A Fundamental Critical Assessment of Efficiencies in Terahertz Time-Domain Spectroscopy Systems

by

Yang Zeng

A thesis submitted to the University of London for partial fulfilment of the requirements of the degree of Doctor of Philosophy

School of Electronic Engineering and Computer Science
Queen Mary, University of London
United Kingdom

January 2017

TO MY FAMILY

I, Yang Zeng, confirm that the research included within this thesis is my own work or that where it has been carried out in collaboration with, or supported by others, that this is duly acknowledged below and my contribution indicated. Previously published material is also acknowledged below.

I attest that I have exercised reasonable care to ensure that the work is original, and does not to the best of my knowledge break any UK law, infringe any third party's copyright or other Intellectual Property Right, or contain any confidential material.

I accept that College has the right to use plagiarism detection software to check the electronic version of the thesis.

I confirm that this thesis has not been previously submitted for a degree by this or any other university.

The copyright of this thesis rests with the author and no quotation from it or information derived from it may be published without the prior written consent of the author.

Signature: Yang Zeng

Date:

Abstract

The electric properties of materials in the THz spectrum are of significant interest for scientific research in the past two decades thanks to the development of THz-TDS systems. However, the measurement capability of the system is still bound by the low efficiency and instability of the system. In this work, a thorough assessment of the THz-TDS system is carried out in order to enhance the measurement capability of the system and provide guidelines for accurate and repeatable measurements.

In Chapter 2, the operation fundamentals of THz-TDS systems including the generation and detection are reviewed. The limitations of THz-TDS systems are evaluated in the aspects of dynamic range, signal-to-noise ratio, and spectral resolution. The influence of systematic parameters are addressed and examined.

In Chapter 3, a systematic characterisation of the performance of PCAs is performed. The performance of THz PCA is evaluated with respect to the intrinsic and extrinsic excitation parameters, as well as the power collection efficiency within the THz-TDS system. Performance evaluation is carried out in combination of experimental measurements and numerical modellings.

Chapter 4 extensively investigates the sensitivity of the THz-TDS system regarding on misalignment of the components. An EM simulation model is built for the evaluation. Point E-field respond in frequency domain and time-domain are examined corresponding directly to the detection signal, and compared with lab measurements. The model is then extended to study the field distribution inside the system. Mode analysis of the field is conducted to discover the pattern of energy coupling related to misalignment.

Chapter 5 aims to further enhance the efficiency and radiation characteristics of THz PCAs by adapting the concept of antenna array. The influence of array configuration

is assessed by array factor analysis. Coupling conditions of array parameters are established. Performance dependences of THz PCAs on the array geometrics are extensively studied in theory, and tested against experiment.

Chapter 6 assess the implementation of plasmonoic structures for the improvement of efficiency and power at the THz generation process. Fundamentals are discussed and structures are designed accordingly. Optimisation principles in consideration of the carrier properties are proposed and practised. Photoconductive antennas with plasmonic structures are fabricated and tested in a THz-TDS system, and the results are compared with simulation.

Acknowledgments

Undertaking my PhD study in the Antennas Group, Queen Mary University of London has been an unforgettable experience. It would not be possible to accomplish without the help from so many people.

First I would like to express my sincerest gratitude to my primary supervisor, Dr. Robert Donnan for his insightful guidance and lasting support throughout my study. I am always encouraged and motivated from our discussions. I would also like to thank my secondary supervisor Prof. Xiaodong Chen and my independent assessor Dr. Akram Alomainy for their helpful advices.

I would like to specially acknowledge Dr. Theo Kreouzis from for supporting me in using the facilities in School of Physics and Astronomy, Queen Mary University of London during my study, and for sharing his enriched experiences in experiments and measurements. My sincere acknowledgement also goes to the clean room lab manager Geoff Gannaway for his guidance and help in photo-lithography, and the antenna lab manager Max Torrico for his support in my experiment.

I would like to appreciate Dr. Bin Yang from University of Chester for sharing his experience in THz-TDS and quasi-optic systems, and Dr. Jue Wang from University of Glasgow for his effort in the fabrication of plasmonic electrodes with electron beam lithography.

Many thanks to Ahmed Aziz and Dr. Oleksandr Sushko for their assistance and discussion in the alignment and operation of the THz-TDS bench.

I am more than grateful to all my friend and colleagues, including Dr. Guangwei Jiang, Dr. Xiang Li, Dr. Junyi Qiu, Dr. Fengfeng Zhang, Dr. Ke Yang, Jing Tian, Andre

Sarker, Thomas Luftus, Xingjian Zhang, Wenjun Sun, Yuan Ma, Biyi Wu, for their support, advices and discussions.

My greatest gratitude goes to my family and my girlfriend Dr. Chuying Yu for their unconditional love, caring and encouragement during all these years.

The financial support from China Scholarship Council is gratefully acknowledged and highly appreciated.

Table of Contents

Abstract **ii**

Acknowledgments **iv**

Table of Contents **vi**

List of Figures **x**

List of Tables **xvii**

List of Abbreviations **xviii**

List of Symbols **xx**

1 Introduction **1**

1.1 Introduction to THz Science and Technology 1

1.2 Introduction to THz-TDS and its Applications 5

1.3 Objectives of Study 6

1.4 Organisation of the Thesis 8

References 9

2 Principles of Operation and Limitations of THz-TDS **13**

2.1 Generation of Broadband Frequency Envelopes from ultra-short THz Pulses 14

2.1.1 Review of mechanisms 14
2.1.2 Photoconductive Process 16
2.1.3 THz Photoconductive Antennas 19
2.2 Coherent Detection of radiation induced form a THz pulse 23
2.2.1 Photoconductive Antenna Detection 24
2.2.2 Free Space Electro-Optic Sampling 25
2.2.3 Comparison Between PCA Detection and Free Space EO Sampling 32
2.3 Measurement with THz-TDS 33
2.4 Limitation of Measurement 36
2.4.1 Reference Quality 36
2.4.2 Noise 39
2.4.3 Spectrum Characteristics 43
2.5 Summary 46
References 47

3 Characterisation of THz Photoconductive Antennas 52
3.1 Overview 52
3.2 Intrinsic Excitation Parameters 54
3.2.1 Transient Profile of Excitation Optics 55
3.2.2 Substrate Material Properties 58
3.2.3 Optimisation Between Intrinsic Excitation Parameters 61
3.3 Extrinsic Excitation Parameters 63
3.3.1 Bias Electric Field 64
3.3.2 Optical Excitation Geometrics 69
3.4 Power Collection Efficiency in THz-TDS 78
3.4.1 Evaluation Method 78
3.4.2 Efficiency Evaluation of Parabolic Mirror Collection Scheme . . . 80
3.4.3 Experiment Validation and Discussion 83
3.5 Summary 86

References . . . 88

4 Alignment Sensitivity Analysis of THz-TDS System 91

4.1 Introduction . . . 91

4.2 Methods . . . 92

4.3 Electric Field Response in Frequency and Time Domains . . . 95

4.3.1 Simulation Results . . . 95

4.3.2 Experimental Measurements . . . 99

4.4 Field Distribution . . . 102

4.4.1 Beam Waist Expansion . . . 104

4.4.2 Mode Analysis . . . 106

4.5 Summary . . . 112

References . . . 113

5 Terahertz Photoconductive Antennas Arrays 116

5.1 Introduction . . . 116

5.2 Array Factors for THz PCAs . . . 118

5.3 Continuous THz PCA Arrays . . . 119

5.3.1 Array Factors of Continuous Arrays . . . 120

5.3.2 Radiation Dependence of THz PCAs on Optical Beam Size . . . 122

5.4 Discrete THz PCA Arrays . . . 126

5.4.1 Array Factors of Discrete Arrays . . . 127

5.4.2 Analysis and Optimisation of Interdigitated THz PCAs . . . 129

5.4.3 Fabrication and Measurement of Interdigitated THz PCAs . . . 135

5.5 Summary . . . 143

References . . . 144

6 Plasmonic Electrode Assisted Photoconductive Process 146

6.1 Introduction . . . 146

6.2 Extraordinary Optical Transmission for THz PCAs . . . 147

6.3 Coupling Between Enhanced Absorption and Photo-generated Carriers . 152
6.4 Fabrication and Experimental Measurement 158
6.5 Summary 162
References 164

7 Conclusions and future work **166**
7.1 Summary 166
7.2 Future work 169

Appendix A Author's publications **171**

Appendix B Alignment of THz-TDS Systems **173**

Appendix C Fabrication Procedures for THz PCAs **179**
C.1 Thermal Vacuum Evaporator 179
C.2 Photo-lithography 181
C.2.1 Lithography - Metal-Etching Procedure 182
C.2.2 Lithography - Lift-off Procedure 183
C.2.3 Comparison 186

List of Figures

1.1 Terahertz band in the electromagnetic spectrum [2] 1

1.2 The applications and future of THz technology, from [1] at the year of 2007, listing the state of the art at 2007, and the prospects of 2010 and 2015. 4

2.1 An illustration of band diagrams for metal, semiconductor and insulator [16]. For conductors (metals), there is no band gap as the valence and the conduction bands overlap. The band-gap of insulator is relatively large ($\geq$ 3.5 eV).The band-gap of semiconductors falls into the area of intermediate energies. 17

2.2 Schematic diagram of THz pulse emission from a photoconductive antenna excited by an optical pulse [17]. 20

2.3 Generation of THz radiation from photoconductive antennas from parameter settings τ_n =500 fs, τ_m =30 fs, τ_l = 100 fs, (a) time domain signal of the laser intensity (blue), photocurrent (red), electric field (green) normalised to their individual maxima; (b) the spectrum of the generated THz field. 22

2.4 The refractive index ellipsoid of a uniaxial crystal, where the optical axis is set along the z-axis [20]. 26

2.5 Schematic diagram of free-space EO sampling [21] and the polarisation status of the probe optics with and without the THz field. 28

2.6 Normalised $F(f_{opt}, f_{THz})$ of ZnTe with thickness of $L = 0.1\ mm$, $L = 0.5\ mm$ and $L = 2\ mm$, reproduced from [31] 31
2.7 Schematic of THz-TDS operating in QMUL [36] 34
2.8 Reference signal (empty background) and measurement signal (a DNA sample) from a typical THz-TDS system in time and frequency domain [37]. (a) Time domain traces of reference pulse and sample pulse; (b) comparison in power spectrum between sample and reference. 35
2.9 A block diagram of general LIAs 39
2.10 Dependence of reference signal quality to time constant τ_{LIA}. (a) Amplitude, standard divination of noise signal at $\tau = 100$ ms and RMS noise in time domain; (b) SNR in frequency domain from different τ_{LIA}, red and blue traces are displaced by 20 dB and 40 dB for clarity; (c) Power spectra of reference signals at difference τ_{LIA}, normalised to the same noise 41
2.11 Dependence of signal-to-noise ratio and dynamic range on internal reference frequency in lock-in amplification scheme. (a) Signal-to-noise ratio in frequency domain measured with different f_r; (b) Power spectra for different f_r, normalised to the same noise floor 42
2.12 Detection of reference signal with different scan parameters. Plot (a) shows the power spectrum upto 3.75 THz, the upper measurable frequency for $\Delta d = 20\mu$m. Plot (b) zooms in to the spectrum between 0.5 THz and 1.5 THz 45

3.1 The dependence of spectral contribution on optical pulse duration. (a) power spectral densities displayed for optical pulses with same energy; (b) power spectral density for optical pulses having the same peak power. 56
3.2 Ultra-broadband THz wave generated from a 20 fs laser pulse [3]. The highest frequency components extend beyond 15 THz, with the absorption and resonant peaks observed within the spectrum. 57

3.3 Spectral contribution of carriers dynamics in different photoconductive substrates (silicon, semi-insulate GaAs, low-temperature-grown GaAs). . 59
3.4 Comparison of THz pulse radiated from PCAs based on LT-GaAs and SI-GaAs substrates. (a) Time domain signal; (b) Power spectrum. Data are extracted from measurements in [7] and normalised to the peak of the THz pulse from LT-GaAs based PCA. 61
3.5 Power spectrum dependence on the ratio between optical pulse duration and carrier lifetime. The power carried by optical pulses are normalised to the same value, while the frequency is scaled to the inverse of carrier lifetime $f_{ce} = 1/\tau_c$. 63
3.6 Evolution of peak amplitude with bias voltage ranging from 0 V to 200 V. 65
3.7 Spectrum analysis of THz pulses generated under different bias field. (a) Power spectra of THz pulses at different bias; (b) Spectral power ratio 66
3.8 Excitation location dependence of THz PCAs with different electrode materials 68
3.9 Schematic of the ECM. Optical excitation illuminates on the photo-excited area within the gap, while THz wave is radiated from the radiation impedance R_r 72
3.10 Time domain E-field of THz pulses generated from PCAs with different gap dimensions ranging from 70 μm to 110 μm 76
3.11 The radiation pattern of an electric dipole. (a) 3D radiation pattern; (b) E-plane and H-plane of the radiation pattern 79
3.12 Schematic of parabolic mirror collection scheme and the maximum collection angles. (a) Front view; (b) side view. 81
3.13 Collection efficiency of parabolic mirror collection scheme corresponding to different polarisation of photocurrent. 83
3.14 Schematics of back and front radiation layouts. (a) Back radiation; (b) front radiation 84

3.15 Comparison of detected THz signals from back and front radiation layouts. (a) Power spectra; (b) power ratio 85

4.1 Schematic of the simulated QO system 93

4.2 The relative amplitude of E-field at the detection point with regard to lateral error in (a) the x-axis; (b) the y-axis; (c) the z-axis and (d) polar rotation. Results in only one direction are plotted in (b) and (d) owing to symmetry about the yz plane. Dash line is set at 0.7 in (a)-(c), corresponding to half in power. 96

4.3 Transient respond of at the detection point in the simulated THz-TDS system and the spectrum of the recieved signal, considering the displacement transverse to (Plots (a) and (b)) and along the optic axis (Plots (c) and (d)) of parabola $M1$ 98

4.4 The influence of source misalignment along the z-axis to the detected THz signal. Plot (a) shows the recorded THz field in time domain; Plot (b) shows the ratio of the E-field amplitude to the in-focus scenario. . . 100

4.5 The influence of source misalignment along the y-axis to the detected THz signal. Plot (a) shows the recorded THz field in time domain; Plot (b) shows the ratio of the E-field amplitude to the in-focus scenario . . . 101

4.6 Simulated E-field distributions at 1.0 THz in the detection plane for different source locations. Plot (a) is for an ideally-set source; plots (b), (c) and (d) correspond respectively to off-set errors of $d_z = \lambda_c$, $d_x = \lambda_c$ and $d_y = \lambda_c$. 103

4.7 The evolution of beam-waist size with frequency. Plot (a) portrays the evolution of w_x and w_y for the situation of ideal alignment; plots (b) to (d) show the level of expansion of the beam-waist size corresponding to misalignment of the source in z, x and y directions, respectively. 105

4.8 E-field distribution of HG modes from HG_{00} to HG_{22}, corresponding to $w_x = 0.74$ mm and $w_y = 0.86$ mm at $f = 2.0$ THz. 108

5.1 Optical saturation in THz PCAs. (a) Saturation by the radiated THz field of LT-GaAs and SI-GaAs based PCAs [5], linear realtionship between THz field and optical pump power breakdown at 10 mW; (b) Alteration of carrier lifetime due to trapped-state saturation [4], carrier lifetime increases with optical pump power. 117

5.2 Schematic of a planar antenna array, red dots represents the antenna elements. The polar angle θ and azimuth angle ϕ are as indicated 118

5.3 Schematic a continuous THz PCA array with interdigitated electrodes. The THz PCA is excited by an optical beam of beam waist w_o between the electrodes. 120

5.4 Evolution of AF_p at typical frequencies to source dimensions. (a) f = 300 GHz; (b) f = 1.0 THz; (c) f = 2.0 THz; (d) f = 3.0 THz 123

5.5 Measured power spectra of THz pulses radiated from a PCA excited with optical beam of different waists 124

5.6 Schematic a THz PCA array with interdigitated electrodes. Interdigitation of period p, gap width d_g is created in the optically illuminated area. 127

5.7 Evolution of AF_p for p = 20 μm and d_g = 10 μm interdigitation to optical beam waist at typical frequencies. (a) f = 300 GHz; (b) f = 1.0 THz; (c) f = 2.0 THz; (d) f = 3.0 THz 130

5.8 Evolution of AF_p at typical frequencies to period of interdigitation. (a) f = 300 GHz; (b) f = 1.0 THz; (c) f = 2.0 THz; (d) f = 3.0 THz . . . 132

5.9 Evolution of AF_p to gap dimension at typical frequencies. (a) f = 300 GHz; (b) f = 1.0 THz; (c) f = 2.0 THz; (d) f = 3.0 THz 134

5.10 Schematic side view of the four layer interdigitated THz PCA, from bottom to top is the photoconductive substrate, interdigitated electrodes, buffer layer and shadow mask. Polarity of the bias on the electrodes are as displayed, and the shadow mask is aligned to the gap between the electrodes. 136

5.11 Micrographs of selected fabricated THz PCAs with interdigitated electrodes. (a) Without shadow mask layer; (b) after deposition of the shadow mask layer. 137
5.12 Influence of optical beam dimension for interdigitated PCAs. Plots (a) and (b) illustrates the time-domain and frequency domain response of B2 under the two illumination conditions; (c) shows the spectral power ratio between $w_o = 1000$ μm and $w_o = 200$ μm for B1, B2 and B3. . . . 139
5.13 Measured THz signal from C1, C2 and C3 with $w_o = 200$ μm in (a) time domain; (b) power spectrum 140
5.14 Comparison of measured THz signal from interdigitated PCAs with same p but different d_g. (a) Time domain response; (b) frequency domain response of A1 and B1; (c) spectral power ratio between A1 and B1 (blue), A2 and B2 (red) 142

6.1 Schematics of conventional THz PCAs and THz PCAs with plasmonic electrodes [4]. For THz PCAs with plasmnoic electrodes, optical beam is first coupled to the surface plasmons before arriving on the photoconductive substrate. 148
6.2 Schematic of the plasmonic coupled sub-wavelength structure. A TEM wave incidents on the sub-wavelength metal structure with period of p, spacing of a and thickness of h. TM modes are then excited within the nano-slits. 150
6.3 Simulated optical power absorption by different plasmonic geometrics at optical wavelength of 800 nm. (a) non-plasmonic structure; (b) $a =$ 100 nm, $p = 200$ nm; (c)$a = 100$ nm, $p = 300$ nm, (d)$a = 200$ nm, $p =$ 400 nm. 151
6.4 The enhanced area in the ultrafast photoconductive process. The carriers in the enhanced area can reach the electrode before recombined/scattered.153

6.5 Geometric dependence of the average power absorption density in the effective area for d_{eff} = 20 nm. (a) p = 200 nm; (b) p = 300 nm; (c) p = 400 nm; (d) p = 500 nm. 154
6.6 Geometric dependence of the average power absorption density in the effective area for d_{eff} = 200 nm. (a) p = 200 nm; (b) p = 300 nm; (c) p = 400 nm; (d) p = 500 nm. 155
6.7 Distribution of optical power absorption for (a) d_{eff} = 20 nm; (b) d_{eff} = 200 nm. SPs are excited in (a), while the effect of optical diffraction dominates in (b). 156
6.8 Polarisation dependence of average power absorption density of d_{eff} = 200 nm and d_{eff} = 20 nm. 0° refers to TM wave incident, 90° refers to TE wave. 157
6.9 Scanning electron microscope images of selected THz PCAs with plasmonic electrodes. The images in the right column zoom into the plasmonic grating areas on the anodes. (a) p = 200 nm, a = 100 nm; (b) p = 400 nm, a = 200 nm 159
6.10 Measured THz radiation from conventional THz PCA and plasmonic incorporated THz PCAs with different geometric configurations. (a) Time domain signal normalised to the peak amplitude of conventional PCA; (b) power spectrum normalised to the same noise floor. 160
6.11 Defects at the contact between electrode pad and the plasmonic structure.162

B.1 (a)Full layout of the THz-TDS system in QMUL including all the components with notations; (b) photograph of the system. 174

C.1 Schematic of vacuum evaporator (left) and prototype (right) 180
C.2 Fabricated interdigitated electrodes of Pattern C1 from (a) lithography - metal-etching procedure; (b) lithography - lift-off procedure. 186

List of Tables

2-A Comparison of physical processes induced by ultrafast optics for broadband THz wave generation 15

2-B Comparison between free space EO sampling and PCA detection 33

2-C Specifications of commercialised THz-TDS systems 38

3-A Comparison between THz PCAs and RF/MW antennas 53

3-B Calculated excitation factors k_ρ 77

4-A The weight of dominant modes HG_{00} and HG_{02} for error-free situation at selected frequencies in percentage 109

4-B Power contribution of Gauss-Hermite modes at $f_1 = 0.5$ THz 110

4-C Power contribution by HG_{mn} mode at $f_2 = 1.5$ THz 110

5-A Geometric parameters of fabricated interdigitated PCAs 135

List of Abbreviations

AF	Array Factor
CAD	Computer Aid Design
DNA	Deoxyribonucleic Acid
DR	Dynamic Range
ECM	Equivalent Circuit Model
EM	Electromagnetic
EO	Electro-optic
FFT	Fast Fourier Transform
FWHM	Full-Width at Half-Maximum
GO	Geometric Optics
HG	Hermite-Gaussian
PAD	Power Absorption Density
SNR	Signal to Noise Ratio
SPP	Surface Plasmon Polariton
LIA	Lock-in Amplification
LSPR	Localised Surface Plasmon Resonance
LT-GaAs	Low-temperature-grown gallium arsenide
NIR	Near Infra-red
SI-GaAs	Semi-insulate gallium arsenide

TDS	Time Domain Spectroscopy
TE	Transverse Electric
TEF	Trap-Enhanced Field
TEM	Transverse Electric and Magnetic
THz	Terahertz
TM	Transverse Magnetic
TPX	Polymethylpentene
PCA	Photoconductive Antenna
PO	Physical Optics
PSD	Power Spectral Density
QMUL	Queen Mary University of London
QO	Quasi-Optic
RMS	Root Mean Square
SEM	Scanning Electron Microscope
SPP	Surface Plasmonic Polariton
SP	Surface Plasmon
STD	Standard Deviation

List of Major Variables

A_s	Source area
A_{eff}	Enhanced area
A_E	Spectral ratio of electric field
a	Width of electrodes
α	Absorption coefficient
d	Thickness of sample
d_m	Diameter of parabolic mirror
$d_{x/y/z}$	Misplacement in the $x/y/z$ direction
d_{eff}	Dimension of effective area
d_{o-c}	Distance between centre of optical beam and cathode
$d_{i/u}$	Dimension of illuminated (unilluminated) area
d_g	Gap dimension
Δd	resolution of the delay stage
$\Delta n/p$	Photo-generated carrier density of electrons/holes
E	Intensity of electric field
ϵ	Permittivity
η_q	Quantum efficiency
η	Ratio between optical pulse duration and carrier lifetime
η_r	Radiation factor
η_p	Ratio of radiated power

f	Frequency of THz/optical wave
f_{ce}	Reverse of carrier lifetime
f_c	Critical frequency for direction radiation
f_r	Reference frequency in LIA
f_s	Sampling frequency
f_{cs}	Critical frequency for the appearance of side lobes
H	Frequency domain response of carriers
I_{PC}	Photocurrent
I	Spectrum of the intensity envelope of optics
$I_{opt}(I_{opt}^0)$	(Initial) intensity of optical beam
$I_{x/y}$	Intensity of x/y polarised optical beam
j_{pc}	Photocurrent density
k	Wave number
k_ρ	Excitation factor
L	Thickness of EO crystal
λ	Wavelength
l_f	Focal length
$\mu_{e/p}$	Mobility of electrons/holes
$n(n_{o/e})$	Refractive index (of ordinary/extraordinary light)
N	Number of elements
ω	Angular frequency
P_{rad}	Radiated power
P_a	Power absorption density
$\phi(\Delta\phi)$	(Change in) phase
p	Periodicity
$R(R_{s/p})$	Reflection Coefficient (of s/p polarised wave)
$R_{i/u}$	Resistance of illuminated (unilluminated) area
R_r	Radiation resistance
$\rho_{i/u}$	Average resistivity of illuminated (unilluminated) area

σ_s	Conductivity of semiconductor
t	Time
t_r	Retarded time
τ_c	Lifetime of electrons
τ_p	Full width at half maximum of optical pulses
τ_s	Momentum relaxation time
τ_{LIA}	Time constant in LIA
θ	Polar angle
U_{bias}	Bias voltage
$v_{e/p}$	Drift velocity of electron/holes
$w_{x/y}$	Beam waist in the x/y direction

Chapter 1

Introduction

1.1 Introduction to THz Science and Technology

Alongside the robust advance in optics and microwave technology in the late 20th century, the intermediate band of frequencies has started to attract significant attention. This intermediate band of frequencies, as indicated in Fig. 1.1, is now identified as the terahertz (THz) spectral domain. The definition of the THz band is still ambiguous for the moment, while the frequency range between 0.1×10^{12} Hz (0.1 THz) and 10×10^{12} Hz (10 THz) is considered as a commonly accepted coverage of the concept [1].

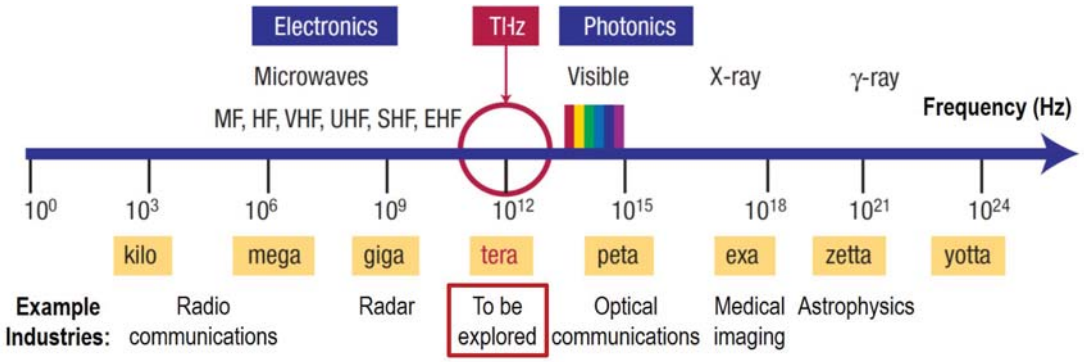

Figure 1.1: Terahertz band in the electromagnetic spectrum [2]

One can take a glimpse into the growing interest by assessing the bibliometrics of the field. The number of related research articles has grown exponentially since 1975 [3]. The on-going research interest arises from the unique characteristics the THz band possesses, and the wide potential of applications unique to it. These characteristics include [4]:

1. **Frequencies above microwave**. The higher frequencies make THz radiation a candidate for the coming high data rate communication. The associated shorter wavelength allows for finer spatial resolution imaging compared with microwave techniques.

2. **Transparency to dielectric materials.** THz radiation is transparent to many dielectric materials that are opaque to visible light. This makes THz detection and imaging techniques very attractive for security and military applications.

3. **Spectral fingerprint.** The frequency domain of THz radiation coincides with the spectral features associated with fundamental physical molecular dynamic processes such as rotational transitions and large-amplitude vibrations of organic compounds, lattice vibrations in solids, intra-band transitions in semiconductors, and energy gaps in super-conductors. The interaction between THz radiation and physical, chemical and biological systems with characteristic lifetimes in the picosecond (ps) range, and energetic transitions in the milli-electronvolt (meV) range, is highly complex and intriguing. Hence, THz radiation is a useful tool for spectroscopic material characterisation as well as studying the physical process in molecule;

4. **Low photon energy.** According to Plank's law, the photon energy of THz radiation is much smaller than that of ultra-violent wave. Hence, compared to ultra-violet radiation, THz radiation will not bleach samples under test. This represents a new epoch in areas of basic science such as structural biology where THz probe light uniquely reveals protein-water mechanics.

On the other hand, the THz band is considered as one of the least studied region of the electromagnetic spectrum, mostly due to the shortage of reliable devices that operate within this sub-spectrum [5]. Over the last few decades, breakthroughs in complementary fields such as photonics, material science, micromachining, etc, have offered practical solutions to this bottleneck.

The primary development lies in the realisation of reliable THz source devices. Approaches are made from different starting points. With specialised design in structures and advanced properties of materials, traditional optics, electronic and microwave sources such as lasers [6], solid-state circuits [7] and vacuum electron devices [8] progress has been made to develop coherent THz sources, though with modest power levels, typically delivering at the level of several μW. Besides these traditional devices, photonic sources that rely on the interaction between optics and materials are being extensively studied [9], and play an important role in THz technology. In addition, the possibility of THz thermal and mechanical sources have also been explored with a promising future [3].

The detection of THz wave is also considered challenging. Optical detection devices, such as photo diodes, are generally not suitable because of the low energy of THz photons. On the other hand, the response of electronic detectors is too slow to follow the rapidly alternating field of THz radiation. Currently, direct detection of THz radiation still relies on thermal detectors and Schottky diodes [2]. However, the requirement of cryogenic cooling has limited their adaptability. Meanwhile, coherent detection methods such as photoconductive antenna (PCA) receivers and electric-optic free-space sampling have been rapidly developed [10]. Recent developments also focus on detectors based on field-effect transistors [11]. This novel device couples THz radiation to induce a resonant plasma, and has been demonstrated for both narrow band and broadband THz detection.

Based on advances in THz devices, current research is also focussed on the realisa-

tion of promising applications. Prototypes of THz high-speed communication systems have been proposed and examined [12]. Active and passive THz imaging systems based different principles of operation are developed and applied to practical field including space and environmental science [13], security and defence [14], biology and medical research [15, 16]. THz spectroscopy techniques are now widely used in material determination and chemical structure analysis [17]. The development of practical applications of THz technology and its future are summarised in Figure 1.2.

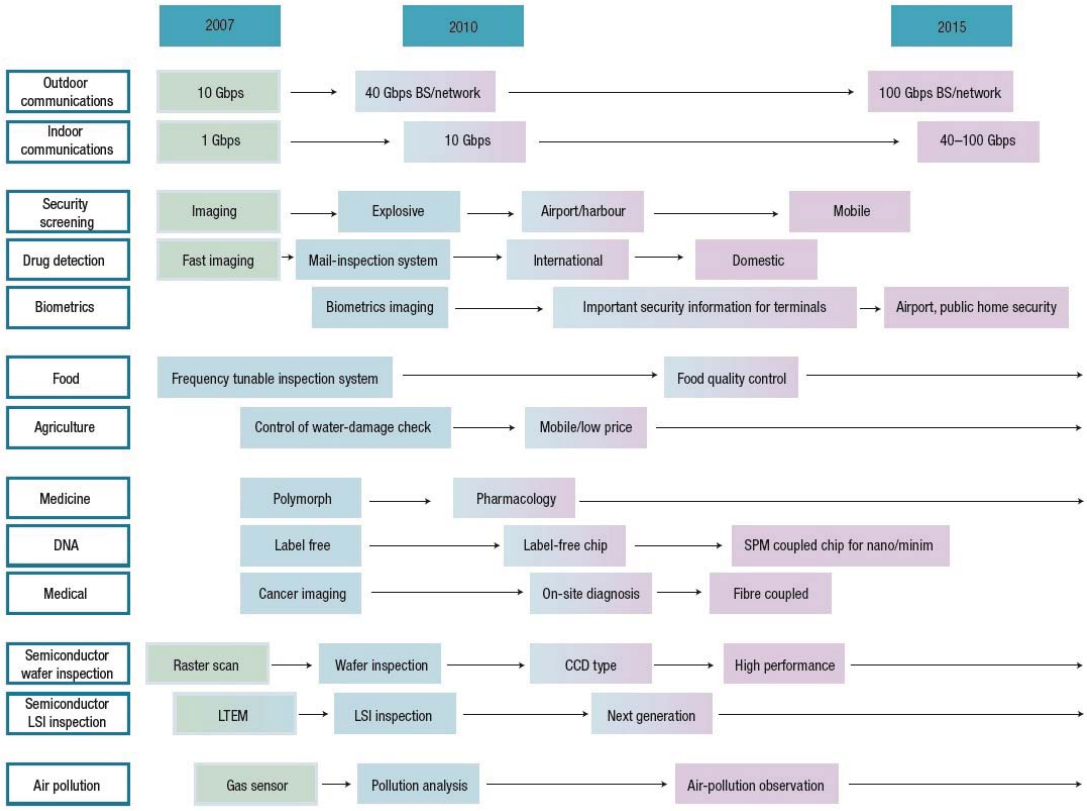

Figure 1.2: The applications and future of THz technology, from [1] at the year of 2007, listing the state of the art at 2007, and the prospects of 2010 and 2015.

1.2 Introduction to THz-TDS and its Applications

Among the variety of THz systems, THz time-domain spectroscopy (THz-TDS) stands out for its unique detection scheme. In the system, the source and detector are coherently synchronised. Compared to thermal detectors, this detection scheme can provide instant amplitude measurement of the THz field, while avoiding strict environmental requirements such as cryogenic cooling. Via the Fourier transform, information in amplitude and phase can also be simultaneously extracted.

THz-TDS systems generally work in the spectral domain between approximately 0.1 THz - 5.0 THz. They operate in a rather different way comparing to traditional spectroscopy methods. In traditional spectroscopy systems, generally, the broadband signal is separated by dispersion devices (e.g. prisms or gratings in monochromators, intermediate frequency mixers in oscilloscopes). The information at a specific frequency is directly measured. In a THz-TDS system, however, measurements are made in the time-domain. The acquired signal from the detector corresponding to a specific time delay τ that contains the information of the entire spectrum. The acquired signal is compared to a reference signal (generally measured without the sample under test in the THz quasi-optical path), to obtain information in the THz region.

The development of THz-TDS systems can be dated back to 1975, when Austin first energised a voltage-biased, silicon-based, photoconductive switch with ultrafast laser pulses and observed photocurrent with a pulse width of less than 20 ps [18]. Coherent detection methods were subsequently introduced to the system in the late 1980s [19]. The broadband THz source and the coherent detection scheme together formed the prototype of current THz-TDS systems. The capability of the system has been significantly extended thanks to the development in the various system components. The highest reported dynamic range of a THz-TDS system exceeds 100 dB [20], while the bandwidth can covering 0.1 THz up to 100 THz [21].

Owning to its unique characteristics, THz-TDS technique plays a role of great significance in the practical application of THz technology. The preliminary application of the technique is to characterise static dielectric properties of materials, including solids, liquid solutions [10] and thin films [22]. These measurements first build up the path to the realisation of THz components with the measured materials by understanding their properties within the spectrum [23]. Moreover, the dielectric properties in the THz spectrum can provide insight into the microscopic properties of a material, such as carrier transport [24], molecular bonding energies [25], *et al.* Based on the principles underpinning dielectric measurements, the synchronised transmission-detection scheme in THz-TDS can be further adapted to study the ultrafast transient processes in the materials that are difficult to monitor with conventional measurement methods [26]. THz-TDS schemes are also being developed for broadband THz imaging. This can be realised by either mechanically scanning the THz beam over an object [27] or illuminating the whole object and analyse the alteration in the spatial distribution of the THz beam [28]. Commercialised THz imaging systems with sophisticated motorised stages can even provide 3D images of the object under test. This can provide buried or occluded information about an object, and has shown great potential in the pharmaceutical and security industries [29, 30]. In conclusion, THz-TDS is a very powerful technique that operates about the centre of the THz spectrum, and is among the most important THz systems.

1.3 Objectives of Study

At present, the major limitation of the THz-TDS technique is its measurement capability, including accuracy, power level and measurement spectrum. The core objective of this study is therefore to explore the possible approaches to extend the measurement capability of the technique. In this study, sub-objectives are drawn to approach the core objective. These sub-objectives are listed as follows:

1. **Sketch out the operational dependence of THz-TDS technique to system components.** The fundamentals of the THz-TDS technique are well established. On the other hand, practical operation of the system is of high complexity. A functioning THz-TDS system consists of not only optical and quasi-optic components, but also mechanical and electronic sub-systems. A comprehensive study of the operation of the dependence of the system on all these components is lacking, but of great importance in order to realise optimum performance.

2. **Provide systematic analysis and optimisation guidelines for THz phtoconductive antennas.** The dominant factor that limits the measurement capability of THz-TDS systems is the low power and efficiency of the THz sources. In this thesis, one of the most commonly used source devices in THz-TDS systems, the THz photoconductive antennas, is made a special object of examination. Systematic assessments of THz PCAs to date are mostly analytical and theoretical, employing simplified models. This thesis aims to provide a combined analyse and evaluation procedure of THz PCAs based on analytical modelling, electromagnetic (EM) simulation and experiment. This will provide a thorough understanding of the generation of THz radiation process, and will map the path for further performance improvement.

3. **Explore the possibility of performance improvement of PCAs with novel concepts.** In this study, two approaches from different technical view are assessed to improve the performance of THz PCAs:

   (a) Photoconductive antenna array: This approach aims at improving the radiation efficiency of PCAs. Most existing work tends to create a dense array layout, with performance being less than expected [31]. Proper guidelines based on array factor analysis is of obvious importance for the development and optimisation of the concept, and is the objective for this part of the study.

(b) Plasmon-assisted photoconductive process: This method tackles the coupling efficiency between optics and the photoconductive material. Promising results are realised [32]. Underpinning physics is also lacking, so this thesis seeks to provide an in-depth analysis of this method, that takes into consideration not only the plasmonic structure but also the carrier dynamics.

4. **Provide assessment methodology for alignment sensitivity in THz-TDS systems.** THz-TDS measurements mostly rely on the interaction between THz radiation and the sample under test in free space. The beam profile of the THz radiation used for sampling can affect the measurement, but is rarely studied. This work aims to provide a methodology to evaluated the beam profile and its sensitivity to system alignment.

1.4 Organisation of the Thesis

The organisation of this thesis is as follows:

Chapter 1 gives a broad background introduction of THz science and technology as well as the THz-TDS technique. Objectives of the study are drawn, and the organisation of the thesis is laid out.

Chapter 2 covers the operational fundamentals of THz-TDS systems. Principles of wave generation and detection are reviewed. Measurement methodology is introduced. Limitations of the system are analysed and discussed.

Chapter 3 provides a thorough characterisation of the performance of THz PCAs in combination of theoretical analysis and experimental measurements. The influences of intrinsic and extrinsic excitation parameters are analysed. The power collection efficiency from different power collection schemes implemented in the THz-TDS systems are evaluated.

Chapter 4 presents a methodology for sensitivity analysis of THz-TDS systems to the alignment of components, especially to the broadband THz source. Simulation results in freuqecy-domain and time-domain are checked against experiment measurements. Field distribution in the system is mapped. The alteration in field distribution is assessed by mode analysis.

Chapter 5 explores the possibility of improving the performance of THz PCAs with array configuration. The influence of the array configuration are evaluated with array factor analysis, and are examined experimentally.

Chapter 6 further examines the prospect of incorporating surface plasmons to enhance the THz radiation from THz PCAs. An evaluation method is proposed to examine the coupling between the enhanced absorption caused by surface plasmons and the photo-generated carriers. In the end, plasmonic incorporated THz PCAs are fabricated and tested in experimental measurements.

Chapter 7 concludes the work in this study, and provides some thoughts for future work.

References

[1] M. Tonouchi, "Cutting-edge terahertz technology," *Nature Photonics*, vol. 1, no. 2, pp. 97–105, 2007.

[2] B. Ferguson and X.-C. Zhang, "Materials for terahertz science and technology," *Nature Materials*, vol. 1, no. 1, pp. 26–33, 2002.

[3] R. A. Lewis, "A review of terahertz sources," *Journal of Physics D: Applied Physics*, vol. 47, no. 37, p. 374001, 2014.

[4] X.-C. Zhang and J. Xu, *Introduction to THz wave photonics*. New York: Springer, 2010.

[5] P. H. Siegel, "Terahertz technology," *IEEE Transactions on Microwave Theory*

and Techniques, vol. 50, no. 3, pp. 910–928, 2002.

[6] S. Kumar, C. W. I. Chan, and Q. Hu, "A 1.8-THz quantum cascade laser operating significantly above the temperature of $\hbar\omega/k_B$," *Nature Physics*, vol. 7, no. 2, pp. 166–171, 2011.

[7] G. Chattopadhyay, "Technology, capabilities, and performance of low power terahertz sources," *IEEE Transactions on Terahertz Science and Technology*, vol. 1, no. 1, pp. 33–53, 2011.

[8] G. L. Carr, M. C. Martin, and W. R. McKinney, "High-power terahertz radiation from relativistic electrons," *Nature*, vol. 420, no. 6912, pp. 153–156, 2002.

[9] H. Hafez, X. Chai, A. Ibrahim, S. Mondal, D. Férachou, X. Ropagnol, and T. Ozaki, "Intense terahertz radiation and their applications," *Journal of Optics*, vol. 18, no. 9, p. 093004, 2016.

[10] P. U. Jepsen, D. G. Cooke, and M. Koch, "Terahertz spectroscopy and imaging - modern techniques and applications," *Laser and Photonics Reviews*, vol. 5, no. 1, pp. 124–166, 2011.

[11] W. Knap, S. Rumyantsev, M. Vitiello, D. Coquillat, S. Blin, N. Dyakonova, M. Shur, F. Teppe, A. Tredicucci, and T. Nagatsuma, "Nanometer size field effect transistors for terahertz detectors," *Nanotechnology*, vol. 24, no. 21, p. 214002, 2013.

[12] S. Koenig, D. Lopez-Diaz, J. Antes, F. Boes, R. Henneberger, A. Leuther, A. Tessmann, R. Schmogrow, D. Hillerkuss, R. Palmer *et al.*, "Wireless sub-THz communication system with high data rate," *Nature Photonics*, vol. 7, no. 12, pp. 977–981, 2013.

[13] P. De Maagt, P. H. Bolivar, and C. Mann, "Terahertz science, engineering and systemsfrom space to earth applications," *Encyclopedia of RF and Microwave Engineering*, 2005.

[14] H.-B. Liu, H. Zhong, N. Karpowicz, Y. Chen, and X.-C. Zhang, "Terahertz spectroscopy and imaging for defense and security applications," *Proceedings of the IEEE*, vol. 95, no. 8, pp. 1514–1527, 2007.

[15] S. Smye, J. Chamberlain, A. Fitzgerald, and E. Berry, "The interaction between

terahertz radiation and biological tissue," *Physics in Medicine and Biology*, vol. 46, no. 9, p. R101, 2001.

[16] C. J. Strachan, P. F. Taday, D. A. Newnham, K. C. Gordon, J. A. Zeitler, M. Pepper, and T. Rades, "Using terahertz pulsed spectroscopy to quantify pharmaceutical polymorphism and crystallinity," *Journal of Pharmaceutical Sciences*, vol. 94, no. 4, pp. 837–846, 2005.

[17] A. I. McIntosh, B. Yang, S. M. Goldup, M. Watkinson, and R. S. Donnan, "Terahertz spectroscopy: a powerful new tool for the chemical sciences?" *Chemical Society Reviews*, vol. 41, no. 6, pp. 2072–2082, 2012.

[18] D. H. Auston, "Picosecond optoelectronic switching and gating in silicon," *Applied Physics Letters*, vol. 26, no. 3, pp. 101–103, 1975.

[19] D. Auston, K. Cheung, and P. Smith, "Picosecond photoconducting hertzian dipoles," *Applied physics letters*, vol. 45, no. 3, pp. 284–286, 1984.

[20] R. Dietz, B. Globisch, H. Roehle, T. Göbel, and M. Schell, "Fiber coupled terahertz time domain spectroscopy system based on InGaAs/InAlAs photoconductors with 100 dB dynamic range," in *2015 40th International Conference on Infrared, Millimeter, and Terahertz waves (IRMMW-THz)*. IEEE, 2015, pp. 1–2.

[21] C. Kübler, R. Huber, and A. Leitenstorfer, "Ultrabroadband terahertz pulses: generation and field-resolved detection," *Semiconductor Science and Technology*, vol. 20, no. 7, p. S128, 2005.

[22] T. Wang, P. Klarskov, and P. U. Jepsen, "Ultrabroadband thz time-domain spectroscopy of a free-flowing water film," *IEEE Transactions on Terahertz Science and Technology*, vol. 4, no. 4, pp. 425–431, 2014.

[23] D. Grischkowsky, S. Keiding, M. Van Exter, and C. Fattinger, "Far-infrared time-domain spectroscopy with terahertz beams of dielectrics and semiconductors," *Journal of the Optical Society of America B*, vol. 7, no. 10, pp. 2006–2015, 1990.

[24] E. Hendry, F. Wang, J. Shan, T. F. Heinz, and M. Bonn, "Electron transport in tio 2 probed by thz time-domain spectroscopy," *Physical Review B*, vol. 69, no. 8, p. 081101, 2004.

[25] C. Ro, L. Thrane, P.-O. Åstrand, A. Wallqvist, K. V. Mikkelsen *et al.*, "Investi-

gation of the temperature dependence of dielectric relaxation in liquid water by thz reflection spectroscopy and molecular dynamics simulation," *The Journal of Chemical Physics*, vol. 107, no. 14, pp. 5319–5331, 1997.

[26] H. Nmec, F. Kadlec, and P. Kuel, "Methodology of an optical pump-terahertz probe experiment: An analytical frequency-domain approach," *The Journal of Chemical Physics*, vol. 117, no. 18, pp. 8454–8466, 2002.

[27] W. L. Chan, J. Deibel, and D. M. Mittleman, "Imaging with terahertz radiation," *Reports on Progress in Physics*, vol. 70, no. 8, p. 1325, 2007.

[28] X. Wang, Y. Cui, W. Sun, J. Ye, and Y. Zhang, "Terahertz real-time imaging with balanced electro-optic detection," *Optics Communications*, vol. 283, no. 23, pp. 4626–4632, 2010.

[29] J. A. Zeitler, P. F. Taday, D. A. Newnham, M. Pepper, K. C. Gordon, and T. Rades, "Terahertz pulsed spectroscopy and imaging in the pharmaceutical setting-a review," *Journal of Pharmacy and Pharmacology*, vol. 59, no. 2, pp. 209–223, 2007.

[30] Y. Shen, T. Lo, P. Taday, B. Cole, W. Tribe, and M. Kemp, "Detection and identification of explosives using terahertz pulsed spectroscopic imaging," *Applied Physics Letters*, vol. 86, no. 24, p. 241116, 2005.

[31] C. W. Berry, M. R. Hashemi, and M. Jarrahi, "Generation of high power pulsed terahertz radiation using a plasmonic photoconductive emitter array with logarithmic spiral antennas," *Applied Physics Letters*, vol. 104, no. 8, p. 081122, 2014.

[32] C. W. Berry, N. Wang, M. R. Hashemi, M. Unlu, and M. Jarrahi, "Significant performance enhancement in photoconductive terahertz optoelectronics by incorporating plasmonic contact electrodes," *Nature Communications*, vol. 4, p. 1622, 2013.

Chapter 2

Principles of Operation and Limitations of THz-TDS

This chapter reviews the principles of operation of THz-TDS systems, and discusses the limitations of measurements. The operation of a THz-TDS system can be summarised into three stages: generation of the broadband THz signal, interaction of THz radiation with the under-testing sample and detection of the modulated THz radiation. Attention is directed first towards the sample-free situation to discuss generation of THz radiation and methods of detection used in THz-TDS. The general methods for sample characterisation with THz-TDS are then introduced. The chapter ends with the discussion of the limitations of THz-TDS operation.

2.1 Generation of Broadband Frequency Envelopes from ultra-short THz Pulses

2.1.1 Review of mechanisms

The Classical electrodynamic theory, as summarised in the Maxwell equations, describes how EM radiation originates from the acceleration of charged particles [1]. To generate EM radiation within the THz spectrum, the period of oscillation of charged particles is required to be in the region of picoseconds (ps) according to the time-bandwidth theorem.

Meeting this requirement with traditional lumped-circuit-based sources is considered extremely challenging, due to energy loss and the effects of parasitic circuit elements. On the other hand, the fast development of ultrafast photonics in the late 20th century opened up the possibility of generating THz radiation by non-oscillatory methods. This principle has been applied to most source devices used in THz-TDS systems. These devices make use of the ultrafast response induced by ultra-short-pulsed lasers that induce fast-varying transient currents, or polarisation in an electro-optic crystal. The ultrafast laser pulse generally has a sub-picosecond pulse length, and plays the equivalent roll of a half-cycle THz feed in a lumped circuit. Subsequently, the transient will radiate in the THz spectrum.

Based on this concept, different physical processes have been explored for the generation of THz radiation. These methods are summarised and compared in Table 2-A with regard to their principle of operation, material requirements and dependence upon external environment conditions.

Table 2-A: Comparison of physical processes induced by ultrafast optics for broadband THz wave generation

Ultrafast Process	Requirement of material	Accelerated particles	Operation principle	Bias field	Radiation direction	Polarisation of optical beam
Photoconductive effect [2]	Photoconductive semiconductors	Free electron hole pairs	Free carriers are accelerated by external E-field to create a fast varying photocurrent	Yes	Normal to interface	Yes [3]
Photo-Dember effect [4]	Photoconductive semiconductors	Free electron hole pairs	Free electrons and holes diffuse in different rate, creating photourrent transient	No	Parallel to interface, can be altered with designed shielding [5]	Yes [6]
Surface field [7]	Photoconductive semiconductors	Free electron hole pairs	Free carriers are accelerated by surface field originating from band-bending at semiconductor-air interface	Not required, H-field can lead to field enhancement [8]	Dependent on direction of excitation optics	No
Shift current [9]	Photoconductive semiconductors	Bounded electrons (polarisation density)	Second order non-linear optics process, spatial shift of the center of free electron charge caused by intense optic excitation	No	Set as normal to interface	Yes
Optical rectification [10]	Electro-optic crystals	Bounded electrons (polarisation density)	Second order non-linear optics process, spatial shift of the center of bound electron charge caused by intense optic excitation	No	Set as normal to interface	Yes
Air plasma [11, 12]	Ionised air	Ionised electrons and ions	Different theories depending on opticial excitation (monochromatic light [11] or second harmonic mixing [12])	Not-required, E-field can lead to field enhancement [13]	Follows direction of excitation optics	No [14]

Among all the mechanisms listed in Table 2-A, photoconductive based emitters (photoconductive antennas, PCAs) are one of the most commonly used source devices in THz-TDS. This is mostly due to:

1. Simplicity of operation. PCAs are solid-state, and can operate at room temperature. It does not require complicated maintenance of equipment, as compared to the air-plasma. Compared to surface field emitters, the radiation direction of PCAs are independent from the excitation optics, which simplifies alignment.

2. Power tuneability. The generation process relies on an external bias field. This is generally stronger than fields internal to the crystal generating THz radiation. As will be shown in Chapter 3, the power of THz radiation can be tuned through the external bias without affecting the photoconductive process. This offers PCAs the potential for generating powerful THz radiation.

In this study, PCAs are the primary device for broadband THz pulse generation. In the remainder of this section, the radiation generation process in THz PCAs will be introduced and reviewed.

2.1.2 Photoconductive Process

Based on their electrical behaviour, solids can be classed into three groups: conductors, insulators and semiconductors [15]. According to quantum physics, the difference between these three categories lies in the possible ranges of energy of their electrons, *i.e.*, electronic band structures [16]. An illustration of the band structures of metals, semiconductors and insulators are shown in Fig. 2.1.

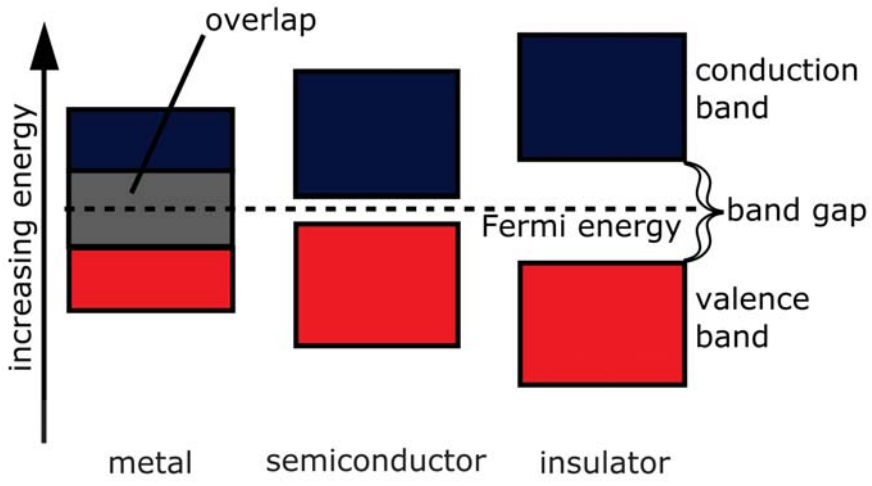

Figure 2.1: An illustration of band diagrams for metal, semiconductor and insulator [16]. For conductors (metals), there is no band gap as the valence and the conduction bands overlap. The band-gap of insulator is relatively large ($\geq$ 3.5 eV).The band-gap of semiconductors falls into the area of intermediate energies.

The existence of a band-gap suggests that pure semiconductor materials (intrinsic semiconductors) are not naturally conductive. On the other hand, the intermediate level of band-gap also indicates that their capability of supporting a current can be easily manipulated compared to conductors and insulators. This manipulation can be achieved in two ways: changing the band structure of semiconductors, or introduce additional energy to the system.

Photoconductive process take the second approach above by altering the conductivity of the semiconductor. External energy is supplied by optical illumination. Free carriers are generated in the electro-optic crystal by absorption of energy from the incident light. The intensity of irradiance into the crystal falls off as a decaying exponential with penetration depth x *i.e.*,

$$I_{opt}(x) = I^0_{opt} \exp(-\alpha x), \tag{2.1}$$

where α the absorption coefficient and I_{opt}^0 is the initial optical intensity at the surface of the crystal.

The most general absorption is the fundamental absorption, when an electron-hole pair is generated by absorbing a photon with energy greater than the band gap. For strongly absorption materials, the optical absorption is considered to be bounded at the surface. The generation rate can be expressed as,

$$G = (\alpha \eta_q I_{opt}^0 / hf)(1 - R) \exp(-\alpha x), \tag{2.2}$$

where η_q is the quantum efficiency, h is the Plank's constant, f is the frequency of the optical wave, and R the reflectivity of the sample.

The induced free charge carriers have two options for paths of propagation. One is to drift under the action of an external electric bias-field; another is to recombine with oppositely-charged free carriers.

Statically, the drift of free charge carriers will form a current. This is evident by a change in conductivity of the semiconductor σ_s. The change in σ_s is expressed as,

$$\Delta\sigma_s = e(\Delta n \mu_e + \Delta p \mu_p), \tag{2.3}$$

where Δn and Δp are the photo-generated carrier densities, μ_e and μ_p are the mobilities of electrons and holes, respectively. The photo-generated current density is,

$$\begin{aligned} \boldsymbol{j}_{pc} &= \Delta\sigma_s \boldsymbol{E} \\ &= e(\Delta n \boldsymbol{v_e} + \Delta p \boldsymbol{v_p}), \end{aligned} \tag{2.4}$$

where $\boldsymbol{v_e}$ and $\boldsymbol{v_p}$ are the drift velocities of electrons and holes, respectively.

The recombination process is described by the carrier lifetime, the average time for carriers to recombine. Taking electrons for example, the continuity equation for

electrons is,

$$\frac{\partial \Delta n}{\partial t} = G - \frac{\Delta n}{\tau_c}, \tag{2.5}$$

where τ_c is the carrier lifetime of electrons. In (2.5), the contribution of diffusion is omitted by assuming that the spatial dependence of the optical excitation intensity is relatively weak.

Equations (2.2), (2.4), (2.5) together portray the photoconductive process in semiconductors. The photoconductive process can be considered as a competition between generation and recombination processes. Free charge carriers are generated by absorbing energy from optical excitation, and then drift according to a bias field, forming a photocurrent. Simultaneously, the charge carrier density is reducing via recombination processes. The transient characteristic of the photocurrent is jointly governed by the nature of optical excitation and the charge carrier dynamics at play in the semiconductor.

2.1.3 THz Photoconductive Antennas

THz photoconductive antennas make use of the non-equilibrium photoconductive process to create fast-varying photocurrents that radiate THz wave. The typical structure of THz photoconductive antennas is shown in Fig. 2.2. A DC bias field is applied to the photoconductive semiconductor substrate through electrodes. Photocurrent is induced when the excitation optical pulse impinges on the electrically-biased region. When the optical pulse ends, the remaining free charge carriers drift until full recombination occurs.

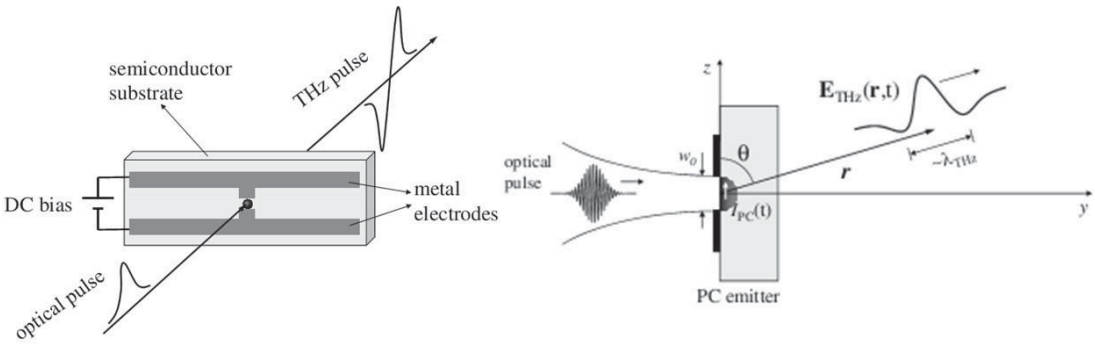

Figure 2.2: Schematic diagram of THz pulse emission from a photoconductive antenna excited by an optical pulse [17].

In the photoconductive process, the total photocurrent is contributed to by both electrons and holes. However, due to the relatively large effective mass of holes (hence their small relative mobility), their contribution to the photocurrent is considerably less than that provided by the electrons. Consequently, the movement of electrons alone is considered. Additionally, in THz PCAs, due to the short duration of optical excitation, the acceleration of electrons should also be taken into consideration. The photocurrent density at time t from (2.4) is,

$$\boldsymbol{j_{pc}}(\boldsymbol{r'}, t) = e\boldsymbol{v_e}(\boldsymbol{r'}, t)n_e(\boldsymbol{r'}, t), \tag{2.6}$$

where $\boldsymbol{r'}$ represents the location of the source in the photoconductive area.

Given that electrons are generated by the incident optical excitation pulse, the transient envelope of the photocurrent density can be considered as the convolution of the optical excitation with the pulse response of the photocurrent [18]. Here, for simplicity, take an infinitesimal source area A_s of excitation for analysis. The influence of the size of the source on radiation characters is therefore ignored, while the spatial distributions of the optical excitation intensity and the bias field are considered uniform.

The photocurrent I_{pc} is then expressed as,

$$\begin{aligned} I_{pc}(t) &= \eta_q \iint I_{opt}(t-t', \boldsymbol{r'})[e\boldsymbol{v_e}(\boldsymbol{r'}, t) n_e(\boldsymbol{r'}, t)] dt' d\boldsymbol{r'} \\ &= \eta_q A_s \int I_{opt}(t-t')[e n_e(t') v_e(t')] dt', \end{aligned} \tag{2.7}$$

where t' refers to the time of carrier generation. The radiated E-field from a varying current is proportional to its first order time derivative. The radiated THz field from the excited photocurrent is,

$$\begin{aligned} \boldsymbol{E}(t) &= \frac{\mu_0}{4\pi} \frac{\sin\theta}{r} \frac{d}{dt_r} I_{pc}(t) \hat{\theta} \\ &= \frac{\eta_q \mu_0 A}{4\pi} \frac{\sin\theta}{r} \hat{\theta} \frac{d}{dt_r} \int I_{opt}(t-t')[e n_e(t') v_e(t')] dt', \end{aligned} \tag{2.8}$$

where $\mu_0 = 4\pi \times 10^{-7}$ H/m is the vacuum permeability, r is the distance between the dipole and the observation point as illustrated in Fig. 2.2, $t_r = t - r/c$ is the retarded time, θ is the angle between vectors $\boldsymbol{p}$ and $\boldsymbol{r}$, and $\hat{\theta}$ is the unit vector normal to $\boldsymbol{r}$.

Equation (2.8) indicates that the THz radiation from PCAs is determined by the transient characteristics of the optical excitation and the photo-generated electrons (change in movement and density). Assuming the excitation optics to be Gaussian pulses, and the dynamics of the elecrons are described by the Drude model, the photocurrent can be expressed analytically as,

$$\begin{aligned} I_{PC}(t) = \eta_q \frac{\sqrt{\pi}}{2} \mu_e E_{bias} A_s I^0_{opt} \\ \Big[\exp\Big(\frac{\tau_p^2}{4\tau_c^2} - \frac{t}{\tau_c}\Big) \cdot \mathrm{erfc}\Big(\frac{\tau_p}{2\tau_c} - \frac{t}{\tau_p}\Big) - \exp\Big(\frac{\tau_p^2}{4\tau_{sc}^2} - \frac{t}{\tau_{sc}}\Big) \cdot \mathrm{erfc}\Big(\frac{\tau_p}{2\tau_{sc}} - \frac{t}{\tau_p}\Big)\Big], \end{aligned} \tag{2.9}$$

where E_{bias} is the local bias field; τ_s is the momentum relaxation time of electrons; τ_p is the full width at half maximum (FWHM) of the optical pulse; and $1/\tau_{sc} = 1/\tau_c + 1/\tau_s$, $\mathrm{erfc}(x) = \frac{2}{\sqrt{\pi}} \int_x^\infty e^{-t^2} dt$. The spectral information of the THz field is obtained by

Fourier transforming the evolution of E-field in the time-domain,

$$E(\omega) = \int_{-\infty}^{\infty} E(t) \exp(-i\omega t) dt, \tag{2.10}$$

where ω is the angular frequency of the THz wave. The power spectral density (PSD) is represented by modulus square of $E(\omega)$, $P(\omega) = |E(\omega)|^2$, while the phase is represented by its imaginary part.

By adapting this analytical model, Fig. 2.3 portrays the normalised transient envelope of the excitation opticial intensity, photocurrent, the amplitude of the radiated THz field, as well as the PSD of the generated field. The parameters are chosen to correspond to the scenario of a low-temperature-grown GaAs (LT-GaAs) based PCA ($\tau_n = 500$ fs, $\tau_m = 30$ fs) excited by a laser pulse with $\tau_l = 100$ fs.

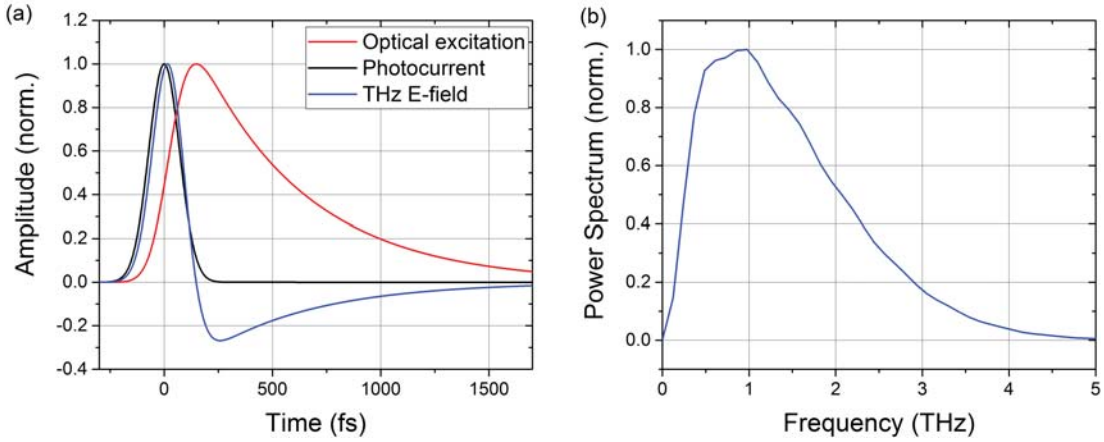

Figure 2.3: Generation of THz radiation from photoconductive antennas from parameter settings τ_n =500 fs, τ_m =30 fs, τ_l = 100 fs, (a) time domain signal of the laser intensity (blue), photocurrent (red), electric field (green) normalised to their individual maxima; (b) the spectrum of the generated THz field.

As depicted in Fig. 2.3, the analytical expression can roughly describe the photoconductive process for THz pulse generation in PCAs. On the other hand, the model

is idealized for the ease of a simplified derivation. A more detailed analysis of the operation of THz PCAs will be presented in following chapters.

2.2 Coherent Detection of radiation induced form a THz pulse

The duration of THz pulses in TDS systems are generally of the order of several picoseconds. Electronic equipment such as oscilloscopes are presently too slow to display this signal. The time-domain coherent detection scheme is reviewed which overcomes this difficulty.

The essence of time-domain coherent detection technique is to divide the THz pulse into small intervals, then coherently measure each interval. The coherency of detection is ensured by the implementation of optically-activated detectors. In the time domain, only the THz signals arriving within the active periods of the detectors can be detected. In THz-TDS schemes, the detectors are activated by the same optical pulse used in the generation of THz radiation. Thus, the detection is synchronised with the excitation of the THz emitter. The division of the THz pulse is realised by introducing a varying time-delay between the arrival of the THz pulse and the activation of the detector. In practice, this time-delay is commonly controlled by altering the optical path length of optical excitation process with motorised translation stages. The duration of each interval is therefore determined by the spatial resolution of stage motion. By scanning through the time-delay, the THz signal in each interval is measured in sequence, and combined to reconstruct a full time-domain envelope.

The time-domain coherent detection scheme is arguably the most vital element in THz-TDS systems. It provides unique and superior capability of offering simultaneous amplitude and phase information. The following will discuss the coherent detection scheme when using the two most common types of detectors, PCAs and electro-optic

crystals.

2.2.1 Photoconductive Antenna Detection

The operation of PCAs as detectors in THz-TDS systems can be considered as the inverse process to the generation of THz radiation. The main difference lies in the photoconductive process. Instead of using the electric field from bias circuits, as during detection, PCAs use the E-field of the incident THz radiation to impel the free charge carriers. The photocurrent generated thus contains information about the incident THz radiation.

Assigning the conductivity of the semiconductor as $\sigma_s(t)$, the current density of the detecting current $J(t)$ can then be calculated as the convolution of the conductivity $\sigma(t)$ and the E-field of the THz radiation E_{THz} is [19],

$$J(t) = \int_{-\infty}^{t} \sigma_s(t - t')E_{THz}(t')dt'. \tag{2.11}$$

By applying the convolution theorem, the responsivity in the frequency domain can be expressed as,

$$\widetilde{J}(f) = \widetilde{\sigma}_s(f) \cdot \widetilde{E}_{THz}(f), \tag{2.12}$$

where $\widetilde{\sigma}_s(f)$ and $\widetilde{E}_{THz}(f)$ are the frequency spectra of $\sigma(t)$ and E_{THz}.

Equations (2.11) and (2.12) provide insight into the accuracy of the detection method. The time domain response of the detector does not directly represent the transient E-field. It is also related to the time-varying conductivity of the semiconductor $\sigma_s(t)$. In practice, this is determined by the duration of the optical pulse τ_l and the carrier lifetime τ_n. Transforming into the frequency domain, the detected spectrum is in fact the spectrum of the THz radiation filtered by the spectrum of $\sigma_s(t)$.

Another factor that needs to be taken into account is the diffraction limit of the

incident THz radiation. The detection mechanism requires interaction of the THz radiation with the photo-excited area of the semiconductor. For ideal detection, the size of the optical excitation and the THz beam should match on the detector. However, this is difficult to achieve owning to the following reasons: firstly, the difference in wavelengths between THz radiation and optical excitation (typically a near infra-red (NIR) pump laser, $\lambda = 800$ nm); and secondly, the broadband nature of the THz pulse. For a specific dimension, diffraction becomes severe as frequency decreases. The responsivity of the detector decreases accordingly. Therefore, the detection of low frequency components of THz radiation is considered to be inaccurate. The lower cut-off frequency is set by the size of the optics on detectors and coating materials.

2.2.2 Free Space Electro-Optic Sampling

Electro-optic (EO) crystals are crystals whose optical properties alter with external E-field illumination. EO sampling technique uses EO crystals as photo-excited detectors in the time-domain coherent detection scheme. The broadband THz pulse is measured through its effect on the EO crystals. Specifically, this effect is characterised by the linear change in the birefringence of the crystals induced by the external E-field, also known as the Pockels effect.

2.2.2.1 Double Refraction

With respect to the directional dependence of their optical properties, crystals can be classed as isotropic and anisotropic. For anisotropic crystals, an incident optical beam will generally create two beams of refraction. This phenomenon is known as double refraction. Double refraction originates from the different refractive indices of crystals to different polarisations of optical field. The polarisations of the two refracted beams are always orthogonal.

The optic axis of a crystal refers to a specific incidence direction, for which double refraction does not occur. For crystals with one optic axis, *i.e.* uniaxial crystals, the two refracted beam are named as ordinary light (o-ray) and extraordinary light (e-ray). The direction of o-ray obeys Snell's law, while the direction of e-light generally does not.

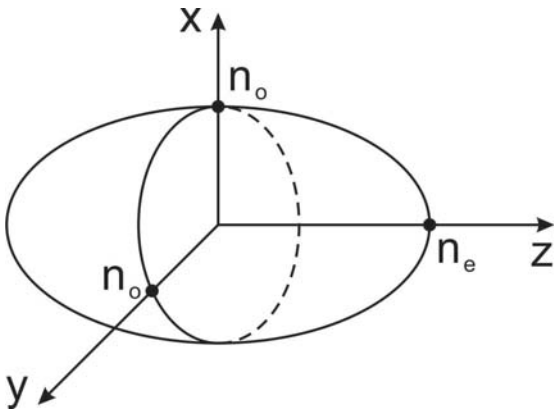

Figure 2.4: The refractive index ellipsoid of a uniaxial crystal, where the optical axis is set along the z-axis [20].

Taking the optic axis as the z-axis, as illusted in Fig. 2.4, the refractive index of a uniaxial crystal to different directions of polarisation can be described with the refractive index ellipsoid [20],

$$\frac{n_x^2}{n_o^2} + \frac{n_y^2}{n_o^2} + \frac{n_z^2}{n_e^2} = 1 \tag{2.13}$$

where n_o is the refractive index for o-ray, and n_e is the refractive index of e-ray.

For light propagating in all directions, its polarisation can be decomposed into two directions: parallel to z-axis and perpendicular to z-axis, *i.e.* within the xy-plane. The refractive index for the projection in the xy-plane is n_o, hence forms the o-ray. The z-polarised component is then the e-ray, and experiences the refractive index of n_e in the crystal. The difference in n_o and n_e characterises the maximum difference of refractive index due to polarisation, and is defined as the birefringence of the crystal.

At the surfaces of uni-axial crystals, o-rays and e-rays generally split as they correspond to different values of refractive index. However, there are two exceptional occasions, when the direction of o- and e-rays coincide,

1. When the light propagates along the optic axis. This is obvious according to the definition of the optic axis. The polarisation of the E-field is purely in the xy-plane. All polarisation components share the same refractive index, as the cut of the index ellipsoid on xy-plane is a circle. Therefore, all lights travel together at the same speed, regardless of the angel of incident on the crystal surface.

2. When the optic axis is parallel to the crystal surface, and the light incidents on the surface perpendicularly. The incident light is decomposed into o- and e-ray as normal. Due to the special arrangement of the crystal surface, the optic axis and incident direction, the o- and e-ray have to travel along the same direction. However, due to the differences in refractive index, their individual propagation speeds and phase changes are different.

2.2.2.2 Detection of THz pulse

The configuration of free space EO detection corresponds to the second scenario mentioned above. Birefringence in the EO crystals is introduced by the arrival of the THz beam. The orientations of the THz field, crystal and polarisation of the optic are specially aligned so that the propagation of the optical pulse will not be disturbed. The influence of the THz beam field is reflected in the phase delay between o- and e-rays.

To effectively detect this phase delay, a balanced detection scheme is commonly applied after the EO crystal. An idealised schematic of the full detection scheme and the polarisation status of the linearly polarised incident optical probe beam is illustrated in Fig. 2.5.

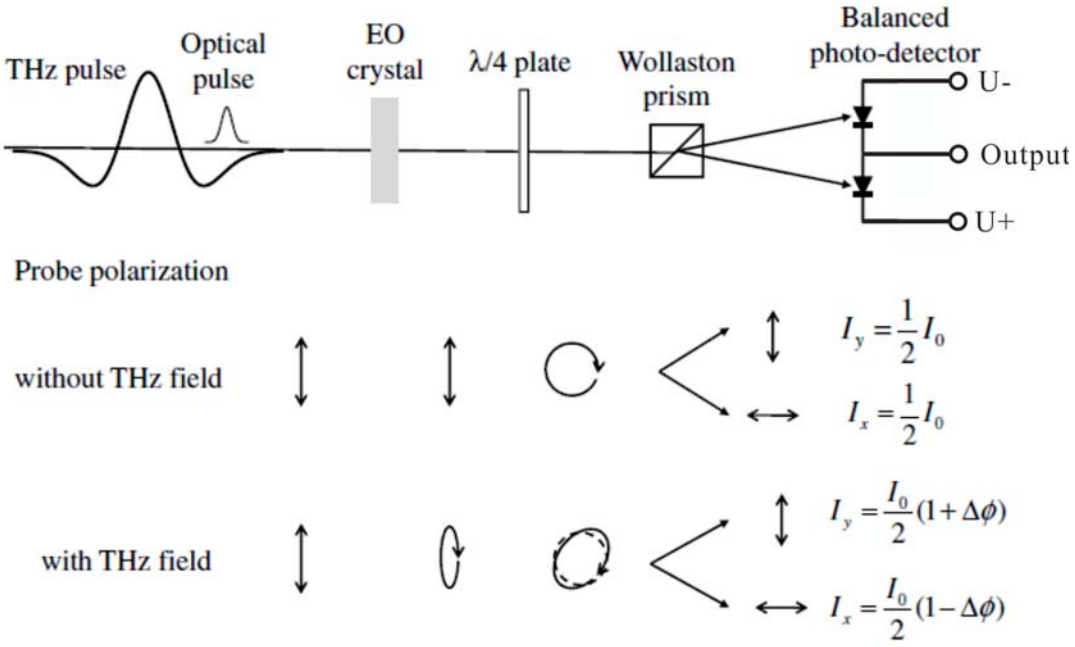

Figure 2.5: Schematic diagram of free-space EO sampling [21] and the polarisation status of the probe optics with and without the THz field.

1. **Without THz field,** the EO crystal is isotropic. The probe light propagates through the EO without any change in polarisation. A quarter wave plate is aligned 45° to the linear polarisation, and converts linear polarisation to circular. A Wollaston prism splits the circularly polarised light into two orthogonal, linearly polarised, beams having no difference in intensity. No signal is detected in the balanced photo-diode detector pair.

2. **With THz field,** double refraction occurs. Due to the phase delay between o- and e-rays, the optical probe pulse becomes slightly elliptically polarised. Subsequently, the circularly polarised light created by the quarter wave-plate is slightly distorted. The intensities of the two beams emerging from the Wollaston prism is different. This divergence is modulated by the THz beam field, and is detected by the balanced pair of photo-diode detectors.

It should be noted that, in practice, most EO crystals are not intrinsically isotropic.

The intrinsic birefringence, however, can be compensated by pre-adjusting the rotation of the quarter wave-plate without the incident of the THz pulse. The measurement, therefore, still reflects the birefringence caused by the bias THz field.

Free space EO sampling of a broadband THz pulse was first realised by X.-C. Zhang using $LiTaO_3$ [22]. Different EO materials were later applied and examined for this detection scheme, and including $LiNbO_3$ [23], ZnTe [24], GaSe [25], GaP [26], CdTe [27] and specialised polymer (MA9:MMA [28]). Here commonly used crystal ZnTe, is discussed as an example. The orientation of ZnTe is set as $< 110 >$. The birefringence caused by the bias THz field is [29],

$$|n_o - n_e| = \frac{n_o^3 \gamma_{41} E_{THz} \sqrt{1 + 3\sin^2 \psi}}{2}, \tag{2.14}$$

where γ_{41} is the EO coefficient of ZnTe crystal, and ψ is the angle between the optic axis of the crystal and the polarisation of the THz beam field. When the THz field is parallel to the optic axis of the crystal, the birefringence is maximum, and the phase delay between o- and e-rays is,

$$\Delta\phi = (n_y - n_x)\frac{\omega L}{c} = \frac{\omega L}{c} n_0^3 \gamma_{41} E_{THz}. \tag{2.15}$$

Accordingly, the intensities of the two beams entering the balanced photo-detector I_x, I_y and the signal measured by the photo-detector I_s is,

$$\begin{aligned} I_s &= I_y - I_x = I_0 \sin\Delta\phi \\ &\approx I_0 \Delta\phi = \frac{I_0 \omega L}{c} n_0^3 \gamma_{41} E_{THz}. \end{aligned} \tag{2.16}$$

As suggested in (2.17), for a selected EO crystal, the responsivity of detection is proportional to its thickness L. However, due to the dispersive nature of the EO crystal, the situation is very different in practice. This will be discussed in the next subsection.

2.2.2.3 Responsivity

Similar to PCA detection, free space EO sampling of THz pulses also relies on optical-THz beam field interaction. As a result, on at the low frequency limit, the cut-off frequency of free space EO sampling is also determined by the diffraction limit of the incident THz beam field. At the high frequency limit, the responsivity of EO detection is affected by the following factors:

1. Finite pulse duration of detection beam. Ideally, the duration of the probe beam should be infinitesimal, so that the detected signal corresponds to the amplitude of the THz beam field of a specific moment. With the duration of the probe beam being finite, the detected signal corresponds to the response of the crystal over the cycle of the pulse.

2. Dispersion of nonlinear susceptibility (the EO coefficient): The EO coefficient of an EO crystal in fact depends on the frequency of the THz beam field. Thus, the constant in (2.17) is actually dispersive.

3. Mismatch between optical group velocity and THz phase velocity: When the optical group velocity and THz phase velocities are different, the probe pulse will be average over several cycles of the THz beam field, and lead to a reduction in the detected signal.

Similar to (2.11), the influence of these factor can be considered as a filter on the detected THz spectrum. The effects of these three factors are considered to be independent. The spectral effect of this filter F is then the product of their individual frequency response [30],

$$F(f_{opt}, f_{THz}) = A_{opt}(f_{THz}) \cdot \chi^{(2)}(f_{opt}; f_{THz}, f_{opt} - f_{THz}) \cdot \Delta\Phi(f_{opt}, f_{THz}) \qquad (2.17)$$

where f_{opt} and f_{THz} are the frequencies of the optical beam and the THz wave, respec-

tively, A_{opt} is the autocorrelation of the optical pulse, $\chi^{(2)}(f_{opt}; f_{THz}, f_{opt} - f_{THz})$ is the second order nonlinear susceptibility corresponding to the influence of EO coefficient in frequency domain, and $\Phi(f_{opt}, f_{THz})$ represents the frequency filtering caused by the velocity mismatch.

For the three filtering factors in (2.17), $A_{opt}(f_{THz})$ and $\chi^{(2)}(f_{opt}; f_{THz}, f_{opt} - f_{THz})$ originate intrinsically from the nature of the system and material, while $\Delta\Phi(\omega, \omega_{THz})$, the influence of phase shift caused by velocity mismatch, is also related to the thickness of the detection crystal. Figure 2.6 illustrates the frequency response of ZnTe with different thicknesses under an 100 fs optical pulse [31].

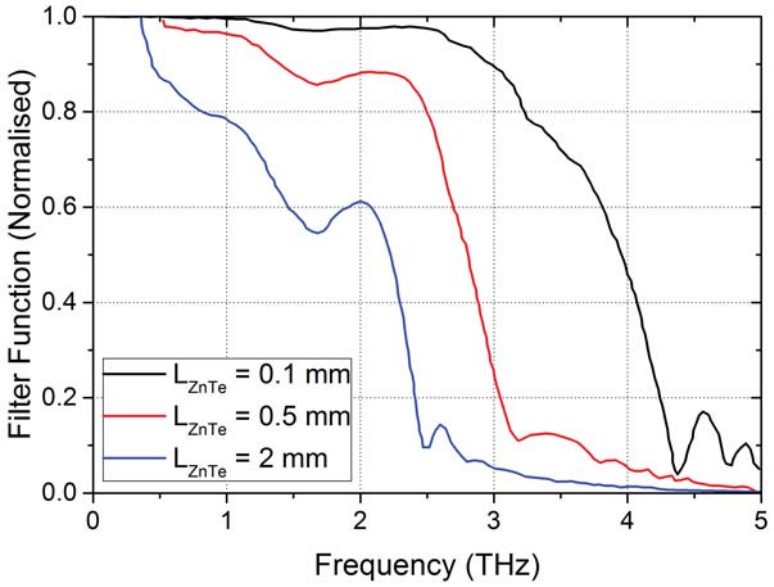

Figure 2.6: Normalised $F(f_{opt}, f_{THz})$ of ZnTe with thickness of $L = 0.1\ mm$, $L = 0.5\ mm$ and $L = 2\ mm$, reproduced from [31]

As illustrated in Fig. 2.6, the bandwidth of responsivity decreases as the thickness of ZnTe increases. This is due to the increase phase shift caused by velocity mismatch between optical and THz beam field in the EO crystal. This effect is amplified for high frequency components in the broadband THz pulse due to the short wavelength. To summarise, in free space EO sampling, the detection bandwidth is compromised by

signal amplitude.

2.2.3 Comparison Between PCA Detection and Free Space EO Sampling

Being the two most widely used coherent detection methods in THz-TDS, THz pulses reconstructed by PCA detection and free space EO sampling are compared in multiple studies.

By taking into account of the spectral filtering factors, the reconstructed signal from the two methods are comparable in the spectrum below 2.0 THz [32, 33]. Compared to PCA detection, free space EO sampling can provide a broader detection bandwidth [34, 35]. The price to pay for this extended spectral detection capability is the relatively complicated configuration to implement free space EO sampling. Free space EO sampling requires extra optical components and a higher level of alignment. For a clearer and detailed comparison, the major aspects of differences in operation and detection capability are compared in Table 2-B.

Table 2-B: Comparison between free space EO sampling and PCA detection

	Free Space EO Sampling	PCA Detection
Bandwidth [35]	Broadband, trade-off between amplitude and bandwidth	Relatively narrower, limit by carrier dynamics
Antenna structure dependence	No	Yes
Alignment requirement	Wave vector matching (strict alignment)	Position matching
Extra optical components	Wave plate, Wollaston-prism	Not required
Support components	Balanced detector, lock-in Amplifier	Lock-in Amplifier, pre-amplifier
Polarisation Dependence	THz field, optic field and crystal orientation	Only THz field
Gate optic power [34]	Low	High
Modulation dependence [33]	High modulation frequency suppresses noise level	Pre-amplifier not compatible with high modulation frequency
Influence of Fabry–Perot effect	Yes	No

2.3 Measurement with THz-TDS

THz-TDS systems are formed by combining the broadband THz pulse generators with the time-domain coherent detection schemes. In addition, quasi-optic (QO) beam forming components are generally added to the systems to guide the THz beam field whilst manipulating their wave fronts. Figure 2.7 schematically illustrate the configuration

of a classic THz-TDS system that operates in the THz laboratory in Queen Mary University of London (QMUL) (full layout and photo in Appendix B).

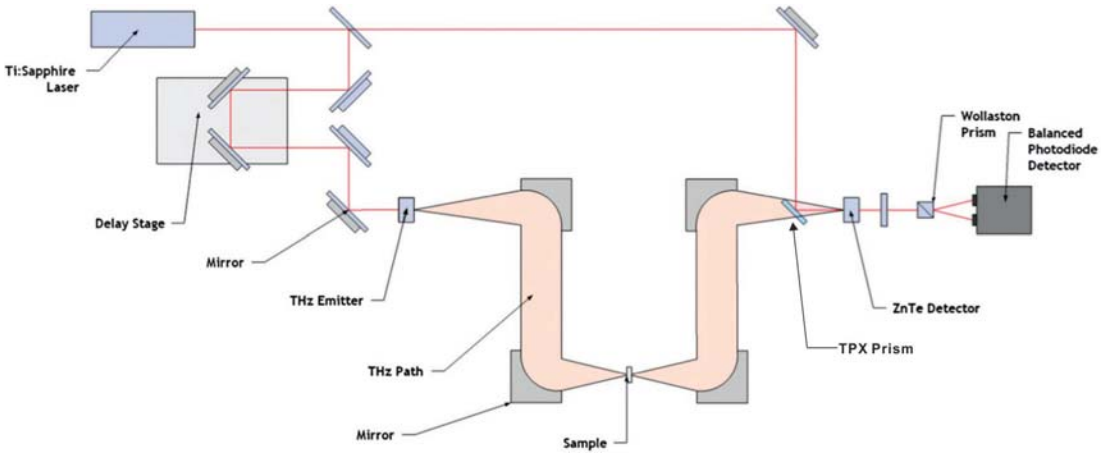

Figure 2.7: Schematic of THz-TDS operating in QMUL [36]

The system is driven by a Ti:sapphire ultrafast laser (Mai Tai, wavelength 750 - 850 nm, repetition rate 80 MHz, pulse length $\leq$ 100 fs, average power $\approx$ 1 W). The THz source used in the system is a GaAs based PCA. A ZnTe crystal is applied as detector in a free space EO sampling set up, while a Polymethylpentene (TPX) prism is used to match the THz wave with the probe optical beam. The delay between the THz wave and optical probe pulse at the detector is controlled by a motorised delay stage with a spatial resolution of 10 μm. In the QO path, four parabolic mirrors are used to guide the THz beam field from the emitter to the detector, providing a focused area and two collimated areas. Sample dielectric measurements can be conducted in any of these areas.

Here, focus lies on to one of the main applications of the THz-TDS technique, to extract dielectric properties of materials with transmission spectroscopy. For this application, at least two scanning signals are required. The signal acquired from a time-domain scan without the under-test sample in the QO path is referred to as the reference signal. All acquired sample pulse signals are compared with this reference for

dielectric parameter extraction. Figure 2.8(a) and (b) present the measured reference and sample signals in the time domain and frequency domain of a DNA sample [37].

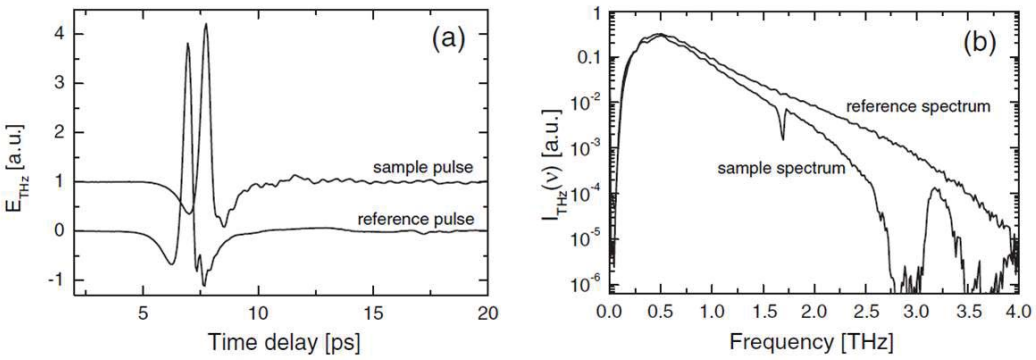

Figure 2.8: Reference signal (empty background) and measurement signal (a DNA sample) from a typical THz-TDS system in time and frequency domain [37]. (a) Time domain traces of reference pulse and sample pulse; (b) comparison in power spectrum between sample and reference.

As illustrated in Fig. 2.8, the influence of the sample-under-test on the reference pulse comes from two aspects. First, the pulse is delayed because of the increased optic path length caused by the refractive index of the sample. In frequency domain, this corresponds to a phase shift over the spectrum. For a sample with a thickness of d, the real part of its refractive index n at frequency f can be calculated directly from the corresponding phase change $\phi(f)$ (in radian),

$$n(f) = 1 + \frac{c}{2\pi f d}\phi(f). \tag{2.18}$$

The second observable influence is the change in the amplitude spectrum caused by the absorption of the sample. Referring to (2.1), and considering the Fresnel coefficient at the air-sample interface with the measured refractive index $n(f)$, the absorption

coefficient $\alpha(f)$ can then be determined by,

$$\alpha(f) = -\frac{2}{d} \ln \left\{ A_E(f) \frac{[n(f)+1]^2}{4n(f)} \right\}, \tag{2.19}$$

where $A_E(f)$ is the spectral ratio of the electric field between the reference signal and sample signal.

This simple and immediate method can provide an approximated value of the refractive index and absorption coefficient of a sample. However, the accuracy of this method is limited by the precision in measurement of the sample thickness. For analytical study, advanced signal processing methods with higher accuracy are required. A common approach is to extend the scan window, and make use of the multiple reflection of the THz pulse inside the sample [38, 39]. The transmitted pulse envelopes from higher order reflections are extracted and compared. Deviations caused by uncertainty in the thickness of a sample can then be minimised with the use of iteration algorithms. In reverse, the use of these algorithms can also help provide a more accurate measurement of the sample thickness [40].

2.4 Limitation of Measurement

So far, the operating principle of THz-TDS has been established. Here the limitation of measurement with THz-TDS is discussed. The constrains of measurement capability, as will be shown, come not only from the wave generation/detection devices, but also from the peripheral operation parameters.

2.4.1 Reference Quality

For dielectric property measurements in THz-TDS, all sample signals are compared with the reference. Therefore, the quality of the reference directly determines the per-

formance of the system. Here, the quality of the reference signal is evaluated from the signal-to-noise ratio (SNR) and dynamic range (DR). The SNR of the system is defined as the ratio between the average amplitude of the signal and its standard deviation [41]. It reflects the stability of the system, and describes the minimum measurable difference. In contrast, the DR of the system refers to the ratio between the signal and the noise floor of the system. They together indicates the minimum and maximum measurable signals of the system. During measurement, the change in magnitude is mainly caused by absorption in the sample. Therefore, the SNR and DR describes the capability of THz-TDS systems by determining the lower and upper boundaries of the measurable absorption coefficient.

As from (2.18) and (2.19), for a sample under test with thickness d, the maximum measurable absorption coefficient at frequency f can be expressed as [42],

$$\alpha_{max}(f)d = 2\ln\left[\mathrm{DR}(f)\frac{4n(f)}{[n(f)+1]^2}\right], \tag{2.20}$$

while the minimum measurable difference in α is,

$$\Delta\alpha(f) = -\frac{2}{d}\cdot\frac{[n(f)+1]^2}{4n(f)}\exp(\alpha d/2)\frac{1}{\mathrm{SNR}(f)}. \tag{2.21}$$

Specifically, the minimum measurable α is,

$$\alpha_{min}(f) = -\frac{2}{d}\cdot\frac{[n(f)+1]^2}{4n(f)}\frac{1}{\mathrm{SNR}(f)}. \tag{2.22}$$

As indicated in (2.20), the measurement capability of a THz-TDS system is limited by two factors: the frequency dependent DR at frequency f, and the thickness of the sample d. The thickness of the sample depends on the measurement process, while the DR is determined by the THz-TDS system. The specifications of major commercialised THz-TDS systems are listed in Table 2-C [43].

Table 2-C: Specifications of commercialised THz-TDS systems

Company	Model	Frequency range (THz)	DR @ approx. 1.0 THz (dB)
Teraview	TeraPulse 3000	0.04 - 3.0	70
	TeraPulse 4000	0.04 - 4.5	70
Advantest	TAS7500SL	0.1 - 2.0	50
	TAS7500SP	0.1 - 4.0	60
	TAS7500SU	0.5 - 7.0	55
Menlo	TeraSmart	0.1 - 4.0	70
	TeraAsops	0.1 - 3.0	60
Picometric	T-Ray 4000	0.02 - 3.5	70
	T-Ray 5000	0.05 - 4.5	70

As shown in Table 2-C, currently, general commercialised THz-TDS systems can cover the spectrum between 0.1 and 4.0 THz, while providing a DR of 60 $\sim$ 70 dB at approximately 1.0 THz. These specifications are comparable to the THz-TDS system operates in QMUL (operates between 0.05 and 4.0 THz with 60 dB DR at 1.0 THz). On the other hand, in the majority of THz-TDS systems, the DR decreases with increasing frequency. Subsequently, the measurement capability weakens at high frequencies. For instance, consider a 20 dB dynamic range at 3.5 THz (a typical value for common THz-TDS systems, as in TeraView TeraPulse 4000), for a 250 μm thick sample, α_{max} is approximately 100 cm^{-1}. For practical applications, this limit is rather low, since for most materials, the absorption coefficient at their absorption peak is generally larger than 1×10^4 cm^{-1}.

2.4.2 Noise

Two approaches can be taken to improve the measurement capability of a THz-TDS system. One is to improve the signal power (this will be assessed in Chapters 3, 5 and 6); another is to suppress noise in the system. Owning to the low power nature of the THz pulses, lock-in amplification (LIA) schemes are commonly implemented in THz-TDS systems in order to effectively retrieve the THz signal buried in the the noisy background. A schematic of general LIAs is illustrated in Fig. 2.9.

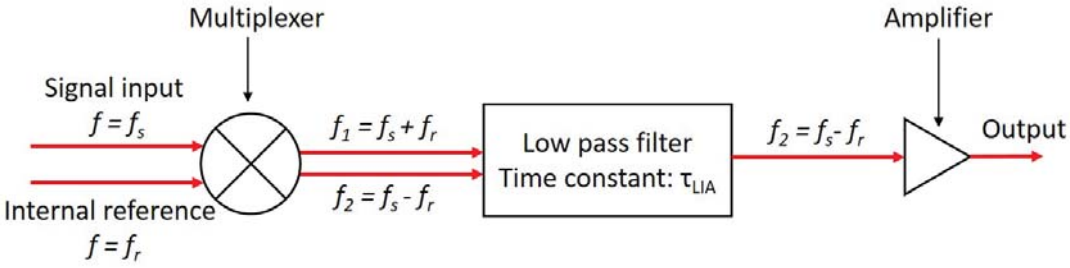

Figure 2.9: A block diagram of general LIAs

As illustrated in Fig. 2.9, in LIA schemes, the input signal is first multiplexed with the internal reference of frequency $f = f_r$. The multiplexed signal is then filtered with a low-pass filter with the time constant of τ_{LIA} before entering the amplifier. As a result, only the signals of frequency $f_s \approx f_r$ can be detected. Therefore, the operation settings of the LIAs can have an affect on the noise level in measurements, and subsequently the quality of the reference signal.

Here, the influences of two LIA settings were demonstrated: the time constant of the low-pass filter τ_{LIA} and the lock-in reference frequency f_r. Their influences were evaluated from the point of view of both SNR and DR. For each operational setting, 10 reference signals were recorded. The measurements were undertaken in atmospheric environment without humidity control. This will lead to reduction in the DR and bandwidth of the system [44]. Spectrally, this is most significant around the absorption

lines of water vapour, but does not seriously affect the comparison of signals over the entire spectrum. In addition, the change in humidity can also introduce extra noise to the system [45]. Nevertheless, the rate of change in humidity is generally slow comparing to the measurement time of THz-TDS systems, hence its influence is limit.

The influence of low-pass filter time constant τ_{LIA} is first assessed . Figure 2.10 illustrates the evaluations of SNR and DR from different τ_{LIA} in both time and frequency domains. The reference frequency f_r was kept at 10 kHz in all measurements.

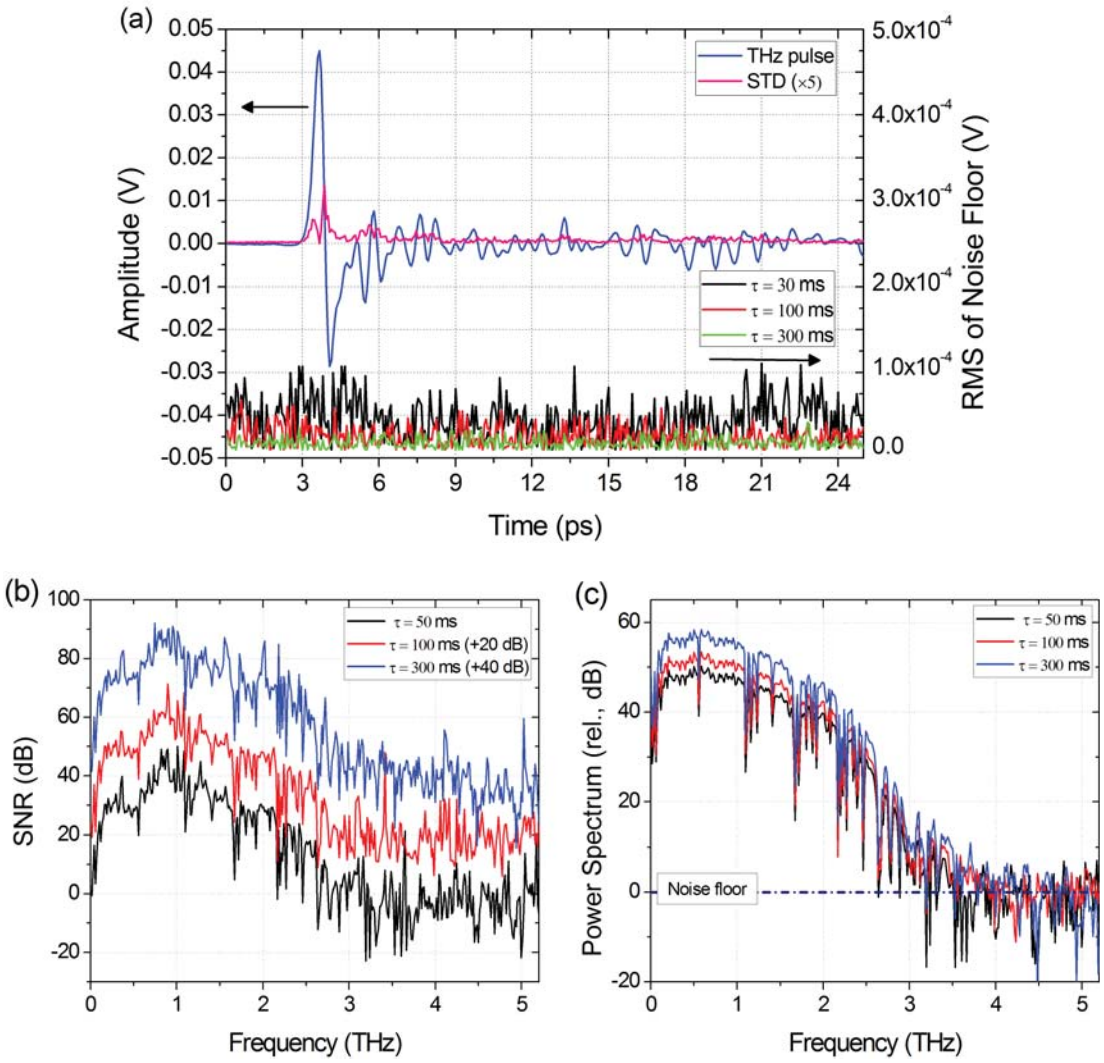

Figure 2.10: Dependence of reference signal quality to time constant τ_{LIA}. (a) Amplitude, standard divination of noise signal at $\tau = 100$ ms and RMS noise in time domain; (b) SNR in frequency domain from different τ_{LIA}, red and blue traces are displaced by 20 dB and 40 dB for clarity; (c) Power spectra of reference signals at difference τ_{LIA}, normalised to the same noise

The results show different effects of τ_{LIA} on the SNR and DR. As illustrated in Fig. 2.10(b), in the frequency domain, the changes in SNR related to τ_{LIA} are negligible (red and blue lines are displaced by 20 dB and 40 dB for clarity). By contrast, increasing

τ_{LIA}, the noise floor is suppressed to a lower level, as shown in Fig. 2.10(a). With no significant change in signal amplitude, an increment in DR of up to 10 dB was observed in the power spectra between $\tau_{LIA} = 30$ ms and $\tau_{LIA} = 300$ ms, as shown in Fig. 2.10(c). The different dependencies of SNR and DR to τ_{LIA} suggest different origins of the fluctuation in the signal and the noise floor. The fluctuation in signal mainly comes from the detected THz beam field. This can be contributed to by fluctuation in the excitation laser power, bias field or disturbance propagation of the THz beam field. This is inheritated by the detected THz wave, hence cannot be suppressed by narrowing the detection bandwidth (increasing τ_{LIA}). However, a reduced detection bandwidth can effectively filter noise within the LIA (Johnson noise, shot noise, etc) and the noise from the detection scheme. This lead to improvement in DR.

The influence of the reference frequency f_r in LIAs is now examined. Fig .2.11 shows the SNR and DR of the reference signal acquired at different f_r. τ_{LIA} is set to 300 ms for all measurements.

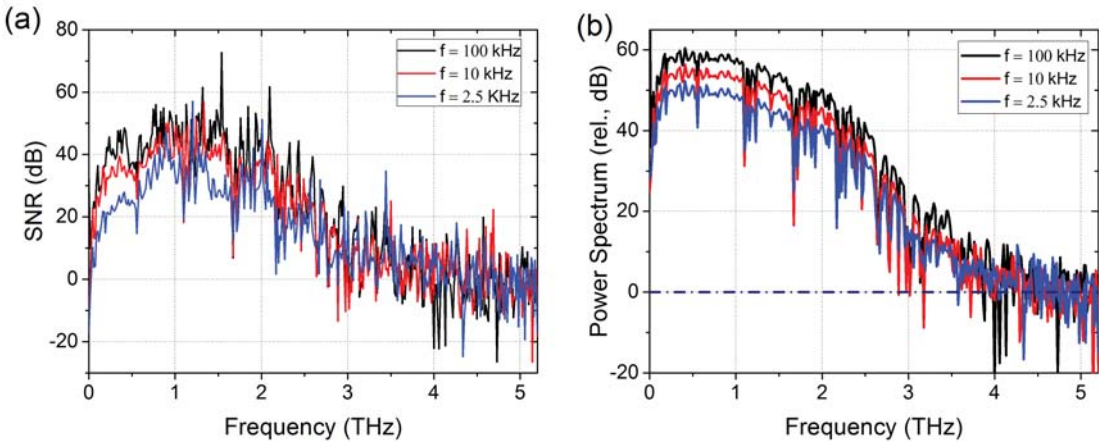

Figure 2.11: Dependence of signal-to-noise ratio and dynamic range on internal reference frequency in lock-in amplification scheme. (a) Signal-to-noise ratio in frequency domain measured with different f_r; (b) Power spectra for different f_r, normalised to the same noise floor

As shown Fig. 2.11, SNR and DR of the system increased simultaneously as f_r increases. In the spectrum below 3.5 THz, an average elevation in SNR of 6 dB is realised by increasing f_r from 2.5 kHz to 10 kHz. By further increasing f_r to 100 kHz, this increment can be further amplified to 11 dB. The DR of the system improves accordingly. This indicates a more effective suppression of the fluctuation in the THz signal. Considering the systematic parameters of the specific system under evaluation (the THz-TDS bench at QMUL), the most likely origin for this improvement in SNR and DR is the reduced jitter in the power of the excitation optics (modulated at 80 MHz).

As discussed above, noise suppression in THz-TDS systems can be improved by optimising the operational parameters of the LIAs. In particular, narrow detection bandwidth is beneficial for the suppression of noise in the detection scheme, while a high reference frequency is preferred to eliminate fluctuations in the THz signal. However, the achievable improvement is very limited. In this evaluation, no significant improvement in DR is realised as τ_{LIA} is further increased above 300 ms. In addition, a larger time constant lead to a slower response in the detection circuit, and subsequently a longer measurement time for the same scan size. The limit in noise suppression corresponding to f_r is not realised in this measurement, as the maximum operation frequency of the LIA in use is 104.8 kHz. The limit is assumed to be in the range of the laser modulation frequency (several MHz). Also, by increasing f_r, the requirements for the signal modulation method (bias modulation or optical chopper) is raised.

2.4.3 Spectrum Characteristics

In THz-TDS measurements, the time-domain signal and spectrum response are connected through discrete Fourier transformation. Therefore, the spectrum characteristics of the measurement is transformed into the characters of time-domain scanning.

The highest measurable frequency is half of the sampling frequency f_s as per the Nyquist theorem. The sampling frequency in THz-TDS is determined by the spatial

resolution of the delay stage Δd through the speed of light in vacuum c as,

$$f_s = 1/\Delta t = c/2\Delta d, \tag{2.23}$$

where Δt is the time-of-flight of light over the spatial resolution of delay ($2\Delta d$).

When choosing the scanning parameters in THz-TDS measurements, the first parameter to be dertermined should be the cut-off frequency ($f_s/2$). It should sufficiently cover the power spectrum of the THz pulse in order to correctly represent the signal. Typical values of Δd are around 10 µm. This yields a maximum measurable frequency of around 7.5 THz. This is generally sufficient to cover most THz-TDS systems with a cut-off frequency at around 5 THz.

For a fixed sampling rate, the spectrum resolution is determined by the number of samples. Fast Fourier Transform (FFT) is the most commonly used method for Fourier transformation of discrete-time signals. For a sample number of 2^N, the spectrum resolution of FFT is,

$$f_r = \frac{f_s}{2^N} = \frac{c}{2^{N+1}\Delta d}. \tag{2.24}$$

After setting the scanning parameters, the spectrum of the detected THz signal is calculated as,

$$E(f) = \sum_{t_n=0}^{t_n=(2^N-1)/f_s} E(t_n)\exp(-i2\pi f t_n), \tag{2.25}$$

where $E(t_n)$ is the measured E-field at time t_n.

As indicated in (2.25), spectral characterisation of the measured THz field is dependent on the scanning parameters. This is demonstrated in experiment by acquiring reference signals in humid air condition with different scanning parameters. The results are illustrated in Fig. 2.12.

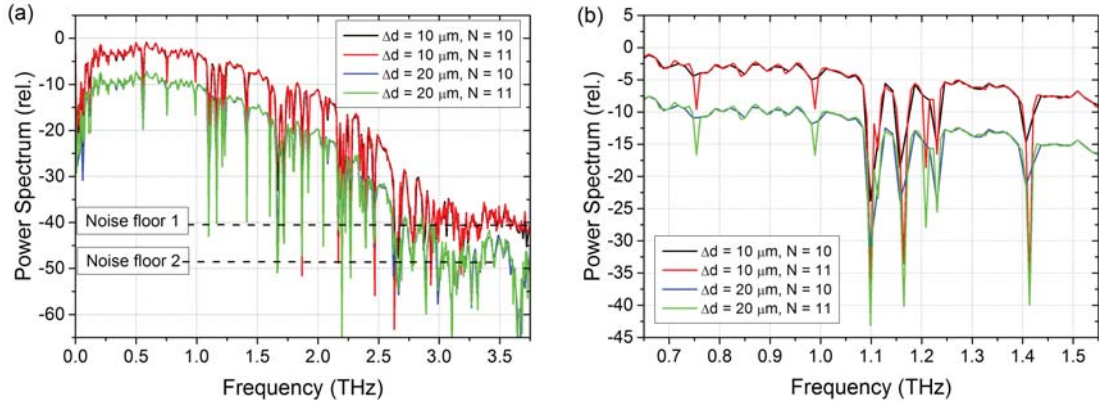

Figure 2.12: Detection of reference signal with different scan parameters. Plot (a) shows the power spectrum upto 3.75 THz, the upper measurable frequency for $\Delta d = 20\mu$m. Plot (b) zooms in to the spectrum between 0.5 THz and 1.5 THz

The cut-off frequency is 7.50 THz for $\Delta d = 10$ μm and 3.75 THz for $\Delta d = 20$ μm. As shown in Fig. 2.12(a), below 3.75 THz there is no significant change in DR between the signals. This suggests that the level of the noise floor is independent of scanning parameters. The power of the THz pulse is mostly spreaded below 3.50 THz. Therefore, a scanning resolution of 20 μm is sufficient to represent the signal. Notable differences are revealed in plot (b) when zooming into the amplitude spectrum between 0.65 - 1.25 THz. The high resolution signals ($\Delta d = 20$ μm, $N = 11$ and $\Delta d = 10$ μm, $N = 11$) are capable of providing more details of the reference environment. For instance, the double absorption lines at 1.208 THz and 1.229 THz [45, 46] cannot be resolved with the low resolution set-ups ($\Delta d = 20$ μm, $N = 10$ and $\Delta d = 10\mu$m, $N = 10$), while the weak absorption lines at 0.750 THz and 1.097 THz are not captured.

The discussion above further provides guidelines for setting spectral resolution in THz-TDS measurements. Equation (2.24) and Fig. 2.12(b) suggest that, after setting the sampling frequency, the spectrum resolution can be improved simply by increasing the number of samples. In addition, (2.24) also provides insight into the dependence

of the spectral accuracy of THz-TDS measurements to the accuracy of the delay stage. The frequency error δf caused by error in delay stage δd can be expressed as,

$$\delta f = \frac{c}{2^{N+1}(\Delta d)^2}|\delta d|. \tag{2.26}$$

As indicated in (2.26), for a fixed sampling frequency, increasing the number of samples is also beneficial in regard to minimising the spectral error. The hard limits are the physical length of the delay stage and the modulation frequency of the excitation laser. However, in practice, the number of samples grows to the power of 2. This dramatically increases the time for measurements. Therefore, the spectrum resolution and accuracy is generally set by the time for measurement.

2.5 Summary

In this chapter, the principles of operation THz-TDS systems were introduced. Different generation mechanisms for broadband THz pulses were reviewed and compared. The THz generation process in photoconductive antennas was specifically focused on and assessed with an analytical model. Fundamentals for the coherent detection scheme were then introduced. The principle of operation of the two most common detection methods, PCA detection and free space EO sampling, were discussed and compared. In summary, the operation of free space EO sampling is more complicated, necessitating better alignment and environmental requirement, but also provides broader detection bandwidth than PCA affords.

After establishing the principles of operation, the methodology of measurement of the dielectric properties of materials with THz-TDS technique was briefly discussed. Based on this methodology, the measurement limitations of THz-TDS systems were thoroughly analysed. The quality of the reference signal in THz-TDS systems was evaluated with respect to DR and SNR, corresponding to the maximum measurable

absorption coeffcient and accuracy of measurement, respectively. It is noted that, without altering the existing generated THz pulse, the signal quality in THz-TDS systems can be improved by optimizing the noise suppression scheme. Specifically, in the commonly used LIAs, the detection time-constant LIA and lock-in reference frequency f_r, play different roles in noise suppression. The detector time-constant mostly contributes to external noise cancellation. By optimising τ_{LIA}, up to 10 dB improvement in DR was achieved in measurements by the QMUL system. By contrast, the reference frequency mostly contributes to suppression of fluctuations in the detected THz beam field. SNR and DR were observed to improve simultaneously as f_r rises. Ultimately, the spectral performance of THz-TDS was evaluated in terms of cut-off frequency, spectral resolution and spectral error. Their correlation with the spatial scanning parameters was established and discussed.

References

[1] J. D. Jackson, *Classical electrodynamics*, 3rd ed. New York: Wiley, 1999.

[2] D. H. Auston, "Picosecond optoelectronic switching and gating in silicon," *Applied Physics Letters*, vol. 26, no. 3, pp. 101–103, 1975.

[3] P. Huggard, C. Shaw, J. Cluff, and S. Andrews, "Polarization-dependent efficiency of photoconducting THz transmitters and receivers," *Applied Physics Letters*, vol. 72, no. 17, pp. 2069–2071, 1998.

[4] K. Liu, J. Xu, T. Yuan, and X.-C. Zhang, "Terahertz radiation from InAs induced by carrier diffusion and drift," *Physical Review B*, vol. 73, no. 15, p. 155330, 2006.

[5] G. Klatt, F. Hilser, W. Qiao, M. Beck, R. Gebs, A. Bartels, K. Huska, U. Lemmer, G. Bastian, M. B. Johnston, *et al.*, "Terahertz emission from lateral photo-dember currents," *Optics express*, vol. 18, no. 5, pp. 4939–4947, 2010.

[6] D. McBryde, M. E. Barnes, S. A. Berry, P. Gow, H. E. Beere, D. A. Ritchie, and V. Apostolopoulos, "Fluence and polarisation dependence of GaAs based Lateral Photo-Dember terahertz emitters," *Optics Express*, vol. 22, no. 3, pp. 3234–3243,

Feb 2014.

[7] X.-C. Zhang and D. Auston, "Optoelectronic measurement of semiconductor surfaces and interfaces with femtosecond optics," *Journal of Applied Physics*, vol. 71, no. 1, pp. 326–338, 1992.

[8] M. B. Johnston, D. Whittaker, A. Corchia, A. Davies, and E. H. Linfield, "Theory of magnetic-field enhancement of surface-field terahertz emission," *Journal of Applied Physics*, vol. 91, no. 4, pp. 2104–2106, 2002.

[9] D. Côté, N. Laman, and H. Van Driel, "Rectification and shift currents in GaAs," *Applied Physics Letters*, vol. 80, no. 6, pp. 905–907, 2002.

[10] A. Nahata, A. S. Weling, and T. F. Heinz, "A wideband coherent terahertz spectroscopy system using optical rectification and electro-optic sampling," *Applied Physics Letters*, vol. 69, no. 16, pp. 2321–2323, 1996.

[11] H. Hamster, A. Sullivan, S. Gordon, W. White, and R. Falcone, "Subpicosecond, electromagnetic pulses from intense laser-plasma interaction," *Physical Review Letters*, vol. 71, no. 17, p. 2725, 1993.

[12] D. Cook and R. Hochstrasser, "Intense terahertz pulses by four-wave rectification in air," *Optics letters*, vol. 25, no. 16, pp. 1210–1212, 2000.

[13] T. Löffler, F. Jacob, and H. Roskos, "Generation of terahertz pulses by photoionization of electrically biased air," *Applied Physics Letters*, vol. 77, no. 3, pp. 453–455, 2000.

[14] C. DAmico, A. Houard, M. Franco, B. Prade, A. Mysyrowicz, A. Couairon, and V. Tikhonchuk, "Conical forward THz emission from femtosecond-laser-beam filamentation in air," *Physical Review Letters*, vol. 98, no. 23, p. 235002, 2007.

[15] C. Kittel, *Introduction to solid state physics*, 7th ed. New York: Wiley, 1996.

[16] K. Seeger, *Semiconductor physics : an introduction*, 8th ed., ser. Advanced texts in physics. Berlin ; New York: Springer, 2002.

[17] X.-C. Zhang and J. Xu, *Introduction to THz wave photonics*. Springer, 2010, vol. 29.

[18] L. Duvillaret, F. Garet, and J. F. Roux, "Analytical modeling and optimization of terahertz time-domain spectroscopy experiments using photoswitches as anten-

nas," *IEEE Journal of Selected Topics in Quantum Electronics*, vol. 7, no. 4, pp. 615–623, 2001.

[19] P. U. Jepsen, R. H. Jacobsen, and S. Keiding, "Generation and detection of terahertz pulses from biased semiconductor antennas," *Journal of the Optical Society of America B*, vol. 13, no. 11, pp. 2424–2436, 1996.

[20] K. Sakoda, *Optical properties of photonic crystals*. Springer Science & Business Media, 2004, vol. 80.

[21] Y.-S. Lee, *Principles of terahertz science and technology*, 1st ed. New York, NY: Springer, 2008.

[22] Q. Wu and X. Zhang, "Freespace electrooptic sampling of terahertz beams," *Applied Physics Letters*, vol. 67, no. 24, pp. 3523–3525, 1995.

[23] C. Winnewisser, P. U. Jepsen, M. Schall, V. Schyja, and H. Helm, "Electro-optic detection of THz radiation in $LiTaO_3$, $LiNbO_3$ and ZnTe," *Applied Physics Letters*, vol. 70, no. 23, pp. 3069–3071, 1997.

[24] Q. Wu and X.-C. Zhang, "Free-space electro-optics sampling of mid-infrared pulses," *Applied Physics Letters*, vol. 71, no. 10, pp. 1285–1286, 1997.

[25] K. Liu, J. Xu, and X.-C. Zhang, "GaSe crystals for broadband terahertz wave detection," in *Nonlinear Optics: Materials, Fundamentals and Applications*. Optical Society of America, 2004, p. MC7.

[26] Q. Wu and X.-C. Zhang, "7 terahertz broadband gap electro-optic sensor," *Applied Physics Letters*, vol. 70, no. 14, pp. 1784–1786, 1997.

[27] X. Xie, J. Xu, and X.-C. Zhang, "Terahertz wave generation and detection from a CdTe crystal characterized by different excitation wavelengths," *Optics letters*, vol. 31, no. 7, pp. 978–980, 2006.

[28] A. Nahata, D. H. Auston, T. F. Heinz, and C. Wu, "Coherent detection of freely propagating terahertz radiation by electrooptic sampling," *Applied Physics Letters*, vol. 68, no. 2, pp. 150–152, 1996.

[29] C. M. Collier, M. H. Bergen, T. J. Stirling, M. A. DeWachter, and J. F. Holzman, "Optimization processes for pulsed terahertz systems," *Applied Optics*, vol. 54, no. 3, pp. 535–545, 2015.

[30] G. Gallot and D. Grischkowsky, "Electro-optic detection of terahertz radiation," *Journal of the Optical Society of America B*, vol. 16, no. 8, pp. 1204–1212, 1999.

[31] G. Gallot, J. Zhang, R. W. McGowan, T.-I. Jeon, and D. Grischkowsky, "Measurements of the THz absorption and dispersion of ZnTe and their relevance to the electro-optic detection of THz radiation," *Applied Physics Letters*, vol. 74, no. 23, pp. 3450–3452, 1999.

[32] S.-G. Park, M. Melloch, and A. Weiner, "Comparison of terahertz waveforms measured by electro-optic and photoconductive sampling," *Applied Physics Letters*, vol. 73, no. 22, pp. 3184–3186, 1998.

[33] Y. Cai, I. Brener, J. Lopata, J. Wynn, L. Pfeiffer, J. Stark, Q. Wu, X. Zhang, and J. Federici, "Coherent terahertz radiation detection: Direct comparison between free-space electro-optic sampling and antenna detection," *Applied Physics Letters*, vol. 73, no. 4, pp. 444–446, 1998.

[34] Q. Wu, F. G. Sun, P. Campbell, and X. Zhang, "Dynamic range of an electrooptic field sensor and its imaging applications," *Applied Physics Letters*, vol. 68, no. 23, pp. 3224–3226, 1996.

[35] S. Kono, M. Tani, and K. Sakai, "Ultrabroadband photoconductive detection: Comparison with free-space electro-optic sampling," *Applied Physics Letters*, vol. 79, no. 7, pp. 898–900, 2001.

[36] A. I. McIntosh, B. Yang, S. M. Goldup, M. Watkinson, and R. S. Donnan, "Terahertz spectroscopy: a powerful new tool for the chemical sciences?" *Chemical Society Reviews*, vol. 41, pp. 2072–2082, 2012.

[37] B. M. Fischer, M. Walther, and P. U. Jepsen, "Far-infrared vibrational modes of DNA components studied by terahertz time-domain spectroscopy," *Physics in Medicine and Biology*, vol. 47, no. 21, p. 3807, 2002.

[38] O. Sushko, K. Shala, R. Dubrovka, and R. Donnan, "Revised metrology for enhanced accuracy in complex optical constant determination by thz-time-domain spectrometry," *Journal of the Optical Society of America A*, vol. 30, no. 5, pp. 979–986, 2013.

[39] I. Pupeza, R. Wilk, and M. Koch, "Highly accurate optical material parameter determination with THz time-domain spectroscopy," *Optics Express*, vol. 15, no. 7, pp. 4335–4350, Apr 2007.

[40] O. Sushko, R. Dubrovka, and R. S. Donnan, "Analysis of optical thickness determination of materials by THz-TDS," *Journal of Physics: Conference Series*, vol. 472, no. 1, p. 012005, 2013.

[41] M. Naftaly and R. Dudley, "Methodologies for determining the dynamic ranges and signal-to-noise ratios of terahertz time-domain spectrometers," *Optics Letters*, vol. 34, no. 8, pp. 1213–1215, Apr 2009.

[42] P. U. Jepsen and B. Fischer, "Dynamic range in terahertz time-domain transmission and reflectionspectroscopy," *Optics Letters*, vol. 30, no. 1, pp. 29–31, 2005.

[43] N. M. Burford and M. O. El-Shenawee, "Review of terahertz photoconductive antenna technology," *Optical Engineering*, vol. 56, no. 1, p. 010901, 2017.

[44] J. Sun, F. Hu, and S. Lucyszyn, "Predicting Atmospheric Attenuation Under Pristine Conditions Between 0.1 and 100 THz," *IEEE Access*, vol. 4, pp. 9377–9399, 2016.

[45] D. M. Slocum, E. J. Slingerland, R. H. Giles, and T. M. Goyette, "Atmospheric absorption of terahertz radiation and water vapor continuum effects," *Journal of Quantitative Spectroscopy and Radiative Transfer*, vol. 127, pp. 49–63, 2013.

[46] M. Van Exter, C. Fattinger, and D. Grischkowsky, "Terahertz time-domain spectroscopy of water vapor," *Optics Letters*, vol. 14, no. 20, pp. 1128–1130, 1989.

Chapter 3

Characterisation of THz Photoconductive Antennas

The key to extend the capability of a THz-TDS system is to improve the quality of the reference signal. The most promising approach is to improve the performance of the THz source. In this chapter, a full characterisation is presented regarding to THz PCAs, one of the most commonly used source devices in THz-TDS systems. This will provide guidelines for the improvement of system performance.

3.1 Overview

The working mechanism of THz PCAs is very different from conventional RF/MW antennas. The major differences between THz PCAs and RF/MW antennas are listed in Table 3-A.

Table 3-A: Comparison between THz PCAs and RF/MW antennas

Parameters	THz PCAs	Conventional RF/MW antennas
Operation frequency	High frequency in THz spectrum, broadband	RF/MW frequency, generally narrow band
Feeding mechanism	Photo excitation	Transmission lines
Nature of current	Drift current formed by photo-generated carriers in photoconductive substrate	Conduction current formed by free carriers in metal
Substrate material	Photoconductive semiconductors	Dielectrics
Bias field	Required	Not required

These differences make the characterisation of THz PCAs challenging. Computer aided design (CAD) methods for conventional antennas are not reliable for THz PCAs due to the multi-physics nature of wave generation and transmission processes. In addition, the shorter wavelengths of THz radiation, with respect to microwaves, increases computational burden. For measurement, the well-established methods and instruments for conventional antenna characterisation are not suitable for THz PCAs. Complete antenna characterisation via time-domain coherent measurement method is experimentally time consuming and problematic.

Currently, characterisation of THz PCAs can be achieved by both numerical calculation and experimental measurement. For numerical simulation, commonly used methods include equivalent circuit approaches [1] and hybrid full-wave calculations [2]. These methods have particular merits in explaining the behaviour of THz PCAs. However, the models used in these methods are generally simplified, and some practical factors ignored. Quantitative predictions of performance with these methods are dif-

ficult to achieve. For experimental characterisation approaches, difficulties lie in the control of the operation conditions of THz PCAs. Generally, only a limited number of parameters can be examined reliably. Comparison between the influence of different parameters is difficult.

Here, a systematic characterisation of the operation of THz PCAs by combining analytical studies with experimental measurements is presented. The study focuses on not only the THz wave generation process in the photoconductive substrate, but also the radiation and collection of the THz wave. For the THz wave generation process, excitation parameters are categorized into intrinsic and extrinsic parameters. Their influences on the THz radiation are examined and discussed. Further, an evaluation method is established and implemented to examine the efficiency of power collection in THz-TDS.

3.2 Intrinsic Excitation Parameters

Intrinsic excitation parameters are set by the system or instruments, and are generally not adjustable. This category includes the pre-set parameters of the pump laser and the carrier characters of the photoconductive semiconductor. These parameters determine the intrinsic factors of the photoconductive process.

As illustrated in (2.9), the temporal envelope of the photocurrent is jointly determined by the time profile of the excitation optics and the transient response of the semiconductor. The generated THz field is proportional to the time derivative of the photocurrent. By applying the convolution theorem, the spectrum of the THz pulse can be expressed as,

$$E(f)_{THz} \propto if \cdot I(f)H(f) = i\sqrt{f}I(f) \cdot \sqrt{f}H(f), \tag{3.1}$$

where $I(f)$ is considered as the spectrum of the intensity envelope of the excitation

optics; and $H(f)$ is the frequency domain response of the semiconductor. Equation (3.1) indicates that, the influences of the optical excitation and the semiconductor are independent in frequency domain. In the following discussions, separate parametric studies are first carried out for these two intrinsic excitation parameters. The significance of their relative values are then subsequently examined.

3.2.1 Transient Profile of Excitation Optics

The temporal profile of the excitation optic pulses are generally considered as to follow Gaussian distribution. The intensity of an optic pulse envelop is described as,

$$I_{opt}(t) = \epsilon_0 c E_0^2 \exp[-\frac{2\ln(2)t^2}{\tau_p^2}], \tag{3.2}$$

where E_0 is the E-field magnitude of the optic pulse; and τ_p is its full-width at half-maximum (FWHM).

In the photoconductive process, the optical excitation creates free carriers in the substrates, leading to an increment in conductivity. As discussed, ultrafast excitation is the key for generation of THz radiation in PCAs. Au ultrafast optical pulse is required to ensure the fast variation of the photocurrent. The duration of the photocurrent is required to be sub-picosecond.

Figure 3.1 illustrates the spectral contribution of optical pulses with varying FWHMs. For clear comparison, the intensity of the optical pulses were set according to two specific scenarios. In Fig. 3.1(a), the energies of the optical pulses were normalised, while in Fig. 3.1(b), the peak power of the optical pulses were set to be the same. Typical values of τ_p between 10 fs and 1 ps were investigated. The absorption coefficient of the photoconductive substrate was assumed to be independent to the pulse duration.

In both Figs. 3.1(a) and (b), a blue shift of the Power spectral distribution (PSD) is observed as the pulse duration shortens. Here this blue shift is described with the

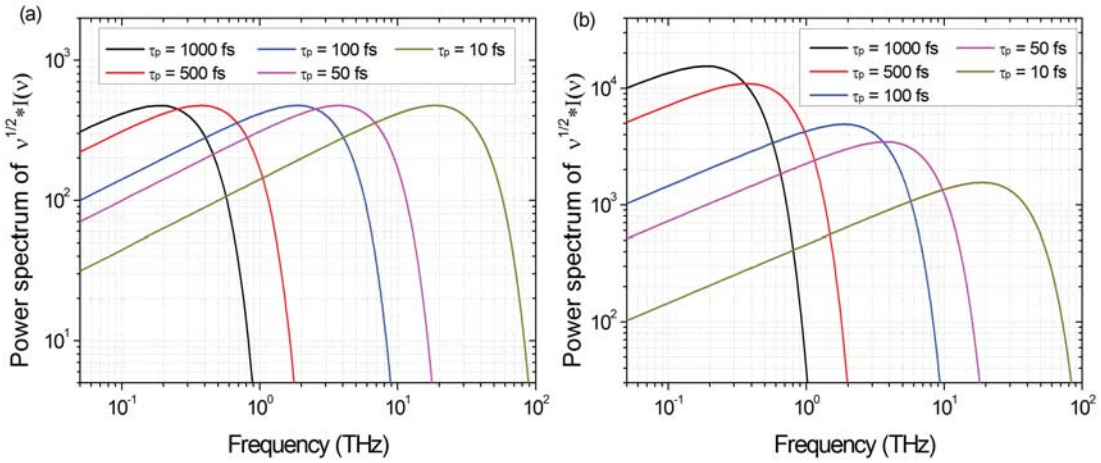

Figure 3.1: The dependence of spectral contribution on optical pulse duration. (a) power spectral densities displayed for optical pulses with same energy; (b) power spectral density for optical pulses having the same peak power.

3-dB upper cut-off frequency f_{3dB}^{+}. For $\tau_p = 1\ ps$, $f_{3dB}^{+} \approx 400$ GHz. In the spectrum above f_{3dB}^{+}, its power distribution drops rapidly. Therefore, excitation optical pulses with $\tau_p \geq 1$ ps hardly contribute to the THz spectrum. This reiterates the necessity for a sub-picosecond optical pulse for THz wave generation. As τ_p decreases to 100 fs, f_{3dB}^{+} will increase to approximate 4 THz. The peak of the spectral distribution is at 2 THz. This pulse duration can be regarded to provide sufficient coverage to the THz spectrum. When τ_p further decreases to 10 fs, f_{3dB}^{+} will reach 35 THz, while the peak of the spectral distribution will shifts to around 10 THz. Variations were also observed in the amplitude of the PSDs. For the optical pulses carrying the same amount of energy, the peak amplitudes of their PSDs are the same as illustrated in Fig. 3.1(a). The blue shifts of the PSDs are accompanied with a reduced power in the low frequency domain. For instance, at 1 THz, the power spectrum of a 10 fs pulse is less than 1/4 of that for a 100 fs pulse. For pulses with the same peak power, this drop in amplitude is more significant, as shown in Fig. 3.1(b). This is due to the reduction in energy carried as the pulse duration decreases. The power spectrum ratio at 1 THz between a 10 fs pulse and 100 fs has dropped to less than 1/10.

Ultrafast optical pulses with $\tau_p < 50$ fs are demonstrated to generate ultrabroadband THz radiation. In the work of Shen [3] *et. al.*, ultra-broadband THz radiation is generated by illuminating a GaAs based PCA with a 20 fs laser pulse. The highest frequency components extend beyond 15 THz in their experiment as shown in Fig. 3.2. By further narrowing the optical pulse width to 12 fs, the bandwidth is extended to above 20 THz, while the signal at 30 THz can still be detected [4]. These results are in good agreement with the analysis above.

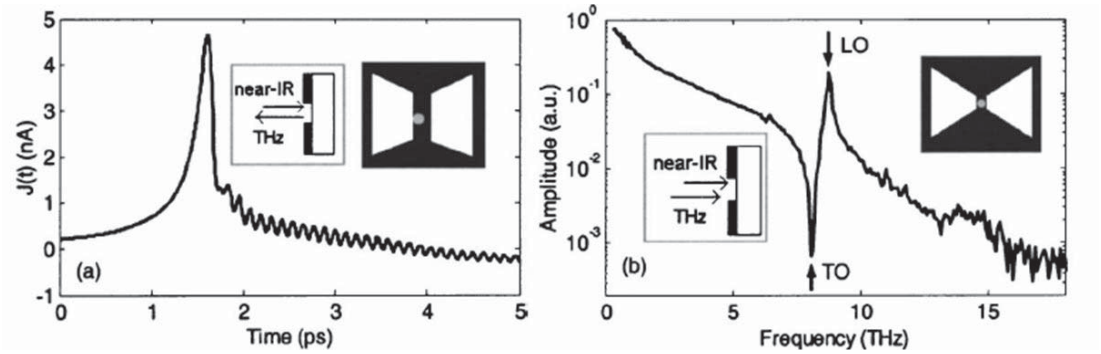

Figure 3.2: Ultra-broadband THz wave generated from a 20 fs laser pulse [3]. The highest frequency components extend beyond 15 THz, with the absorption and resonant peaks observed within the spectrum.

Though the spectrum width of THz-TDS systems can be extended significantly by using shorter excitation pulses, practical applications are still problematic. First is the consideration of the dynamic range. As indicated in Fig. 3.1, dynamic range of the system is compromised by the extended measurement bandwidth. Optical pulses carrying more energy are required to maintain the same dynamic range. In practice this is difficult and costly to realise. The second factor to consider is the properties of materials. The resonant peaks of materials in the THz spectrum generally complicate the generation and detection process. As illustrated in Fig. 3.2, the absorption and resonant peaks of the GaAs substrate at 8.02 THz and 8.76 THz interfere with the broadband signal. The third factor is the higher sampling frequency for the detection system. As the upper cut-off frequency increases, the sampling frequency in the coherent detection scheme has to increase accordingly in order to fully capture the signal. Delay mechanisms with higher accuracy and resolution are required. Meanwhile, as

the operation wavelength shortens, measurements are more sensitive to misalignment. This will be discussed in detail in Chapter 4.

3.2.2 Substrate Material Properties

Now we investigate the performance dependence of THz PCAs on the carrier properties of the substrate material. The transient respond of free carriers in semiconductors can be further separated into two processes: the response of carrier velocity and the response in carrier concentration.

1. **Response in carrier velocity (drift of carriers).**

   Under an external bias field E_{bias}, the variation of carrier velocity is mainly affected by scattering processes. For electrons, the velocity can be described as,

   $$v_e(t) = \mu_e E_{bias}[1 - \exp(-t \cdot \frac{e}{\mu_e m_e^*})], \tag{3.3}$$

   where μ_e is the electron mobility; and m_e^* is the effective electron mass. The time constant $\tau_s = \mu_e m_e^*/e$ is known as the momentum relaxation time of the electron.

2. **Response in carrier concentration (recombination).**

   With no carrier generation process (optical excitation), the change in carrier density is mainly caused by recombination processes. For an initial electron density of n_0, the time-evolution of carrier density $n_e(t)$ is described by,

   $$n_e(t) = n_0 \exp(-t/\tau_c), \tag{3.4}$$

   where τ_c is the carrier lifetime of electrons.

The transient respond of electrons is described by the combination of Equation 3.3 and 3.4. Hence, the major properties of influence on the semiconductor substrate is the

electron mobility μ_e, effective mass m^* and lifetime t_c. Figure 3.3 shows the calculated spectral response of carrier dynamics in several commonly used substrates for THz PCAs.

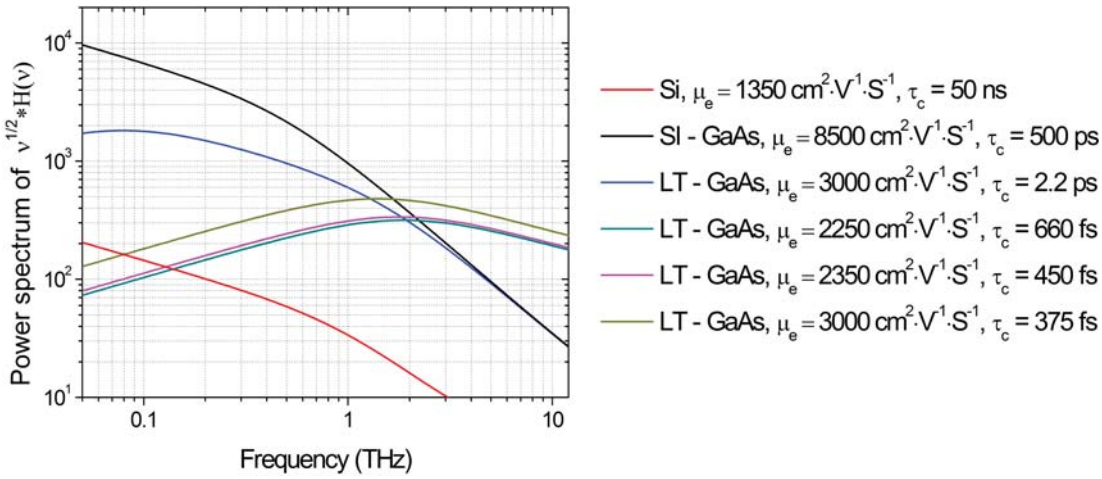

Figure 3.3: Spectral contribution of carriers dynamics in different photoconductive substrates (silicon, semi-insulate GaAs, low-temperature-grown GaAs).

Figure 3.3 firstly demonstrates the superior performance of GaAs-based materials over silicon. Above 200 GHz, all the GaAs-based substrates analysed have a higher magnitude power spectrum than silicon substrates. The power spectrum, related to carrier properties in silicon, drops rapidly as frequency increases. Its contribution above 1 THz is at least an order of magnitude lower than for GaAs-based substrates.

The superior performance of GaAs mainly originates from two aspects: its direct bandgap structure, and its high carrier mobility [5]. The direct bandgap structure offers the material a faster and more efficient photonic response. This leads to a shorter carrier lifetime, and subsequently a more intense variation of the photocurrent. The high electron mobility, on the other hand, amplifies the change in photoconductivity, leading to a larger photocurrent amplitude. These two factors together result in a more intense THz radiation from GaAs based PCAs. This comparison indicates the two key requirements of photoconductive materials: high mobility and short carrier lifetime.

Figure 3.3 also compares the spectral contribution between different types of GaAs substrates. The two most commonly used GaAs are semi-insulating GaAs (SI-GaAs) and low-temperature-grown GaAs (LT-GaAs). For SI-GaAs, undoped substrates are preferred to suppressing dark current and reduction of heating. The carrier properties are considered to be the same as for intrinsic GaAs. LT-GaAs refers to thin GaAs layers grown in a controlled environment. Trapped states are created in order to accelerate the recombination process and reduce the carrier lifetime. The mobility is generally reduced and carrier properties depend on the specific growing process. In the analysis, relevant data are extracted from the work of Gregory *et al* [6].

SI-GaAs and LT-GaAs display different dispersive character. For SI-GaAs, the power spectral density, decreases monotonically with increasing frequency. In contrast, the PSD for LT-GaAs substrates first increases with frequency, then declines after reaching a peak. The spectral location of the peak increases as the carrier lifetime shortens. The results in Fig. 3.3 suggest that the amplitude of the PSD below 2 THz is still predominantly governed by the mobility. Meanwhile, a threshold of approximately 1 ps on carrier lifetime is realised. LT-GaAs substrates with carrier lifetime below this threshold are capable of producing larger spectral power than SI-GaAs above 2 THz.

Figure 3.4 provides a direct experimental comparison of THz PCAs fabricated on LT-GaAs and SI-GaAs substrates [7]. Under the same excitation conditions, SI-GaAs-based PCA generates a higher THz pulse amplitude (approximately 2.3 times in peak), as shown in Fig. 3.4(a). Small but noticeable differences also occur in the pulse shape. The width of the THz pulse generated from SI-GaAs-based PCA is larger, and has a relatively longer tail. More details of the differences are observed in the power spectrum in Fig. 3.4(b). Overall, the trend of the two curves is alike, while the power spectrum of SI-GaAs-based PCA is higher at low frequency, and decreases faster as frequency increases. The intersection of the two curves occurs at 1.90 THz, and the ratio of the power spectrum at 1.0 THz is 2.34. These values are in good agreement with the calculation shown in Fig. 3.3.

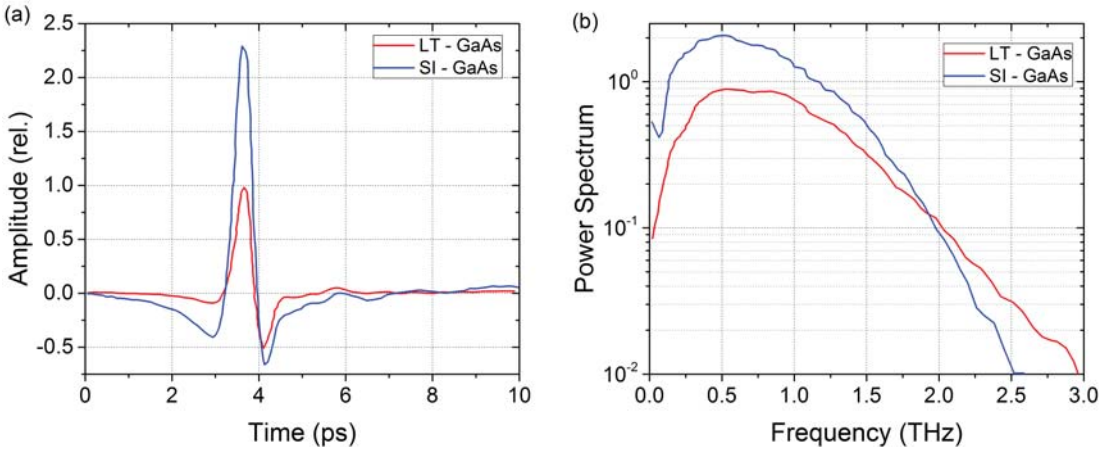

Figure 3.4: Comparison of THz pulse radiated from PCAs based on LT-GaAs and SI-GaAs substrates. (a) Time domain signal; (b) Power spectrum. Data are extracted from measurements in [7] and normalised to the peak of the THz pulse from LT-GaAs based PCA.

The bandgap of GaAs is 1.42 eV, referring to optical absorption edge of around 780 nm. Other than GaAs substrates, ongoing research is exploring the possibility of excitation at different optical wavelengths. The most attractive wavelength is 1550 nm. At this wavelength, matured fibre based optical components can be integrated into THz-TDS systems. This offers the prospect of compact system configurations. Promising candidate materials includes InGaAs/InAlAs [8] Er:GaAs [9].

3.2.3 Optimisation Between Intrinsic Excitation Parameters

Above, the influences of the two primary intrinsic excitation parameters, the temporal behaviour of excitation optical pulse and the transient respond of semiconductor substrate, are discussed independently. In this subsection, further analysis is carried out regarding the relationship between these two factors. This will provide operation and optimisation guidelines for the selection of the intrinsic excitation parameters.

The necessity of sub-picosecond optical pulses for THz generation in PCAs was

demonstrated in the previous discussion. Considering the time scale, semiconductors are classified into two categories with respect to their carrier lifetimes: semiconductors with long carrier lifetime ($\tau_c \gg 1\ ps$) and with short carrier lifetime (comparable to the optical pulse-length).

First consider the long lifetime case. Referring to the results in Fig. 3.3, in the THz region, the spectral power contribution from the carrier dynamics decreases as frequency increases. Its correlation with the spectral contribution of the optical pulse is weak. The location of the peak in the power spectrum is then mostly determined by the transient character of the excitation optics.

The situation is different for semiconductors with short lifetimes, since the contribution from carrier dynamics is no longer monotonous in the THz region. For this case, the joint contribution of the two factors is analysed regarding on the relationship between their transient character $\eta = \tau_p/\tau_c$. Figure 3.5 illustrates the power spectrum of the THz pulse generated from different carrier lifetime/optical pulse length combinations.

In Fig. 3.5, the power carried by optical pulses are normalised to the same value. Meanwhile, in order to present the alteration in bandwidth caused by the η instead of the varying τ_c, the frequency scale is normalised to the inverse of carrier lifetime $f_{ce} = 1/\tau_c$. As shown in Fig 3.5, for semiconductors with short lifetimes, the PSD of the generated THz pulse varies with η between two limits. The first limit occurs at small ratio $\eta \approx 0.1$. This limit refers to the scenario of maximum bandwidth. The upper cut-off frequency (3 dB) can reach up to $2.5f_c$. Beyond this extremum, the distribution of the PSD starts approaching the second limit as η increases. The bandwidth narrows down rapidly, while the power of the THz radiation is compressed to the frequency domain between $0.1f_c$ and $0.5f_c$. The limit occurs at $\eta \to \infty$, while a reasonably good approximation is already achieved for $\eta \geq 0.6$. The peak amplitude is above 90% of the limit, and the upper cut-off frequency is less than $0.8f_c$. Further incrementation in

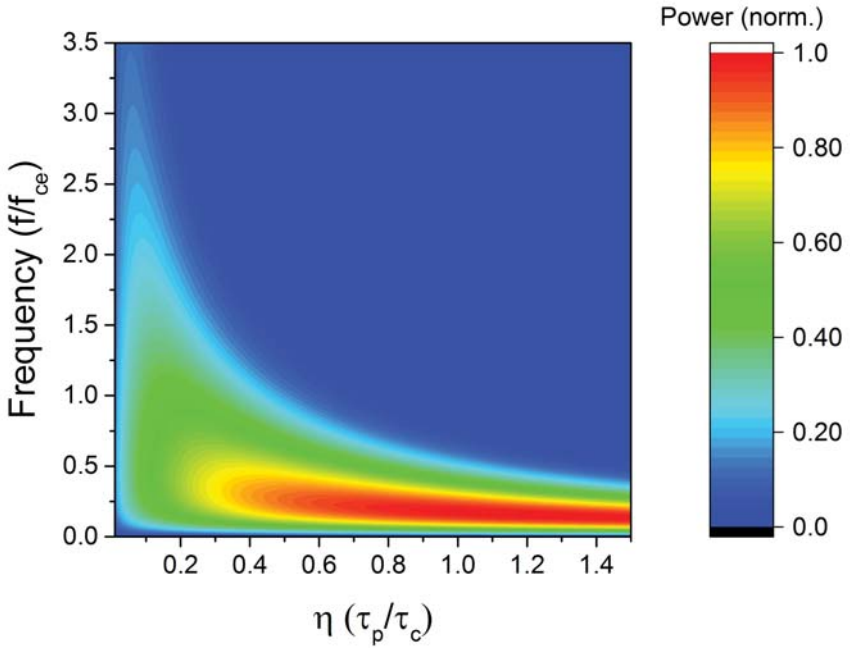

Figure 3.5: Power spectrum dependence on the ratio between optical pulse duration and carrier lifetime. The power carried by optical pulses are normalised to the same value, while the frequency is scaled to the inverse of carrier lifetime $f_{ce} = 1/\tau_c$.

η does not lead to a dramatic change in PSD. Therefore, for the optimum operation with short lifetime semiconductors, two values of η are recommended: $\eta_1 = 0.1$ refers to the scenario of maximum bandwidth; and $\eta_2 = 0.6$ refers to the scenario of intense radiation. For intermediate value $\eta_1 < \eta < \eta_2$, compromise is made between bandwidth and pulse amplitude. By reducing η below η_1, bandwidth and pulse amplitude of the generated THz pulse drop simultaneously. By further increasing η beyond η_2, a small improvement in amplitude can be achieved, while bandwidth of the THz pulse decreases continuously.

3.3 Extrinsic Excitation Parameters

The significance of external excitation parameters on the operation of THz PCAs is now assessed. The external excitation parameters are the conditions provided by the exter-

nal environments. These parameters can be adjusted without significantly influencing the physical nature of the photo-generation process. Their influences are reflected with regards to the extraction of THz radiation from the ultrafast photoconductive process.

Here in this study, the significance of two factors are specifically addressed; first is the bias electric field, and second the geometric layout of the optical excitation.

3.3.1 Bias Electric Field

The discussion in Sec. 3.2 suggests that the temporal shape of the photocurrent is determined by the intrinsic excitation parameters, and subsequently the temporal shape of the generated THz pulse. On the other hand, for the set intrinsic excitation parameters, the bias electric field determines the intensity of the photoconductive process, and thus the strength of the THz field. In this section, the significance of the bias E-field is discussed from two points of view: field intensity and its spatial distribution.

3.3.1.1 Field Intensity

First the influence of the bias intensity during experiments in analysed. The alteration of bias field is realised by controlling the bias voltage applied to the PCA. Reference traces under difference bias voltages are recorded with THz-TDS system in the THz lab at QMUL, while other parameters (excitation and detection) are kept fixed. Figure 3.6 demonstrates the dependence of peak amplitude of the THz pulse on bias field.

Figure 3.6 shows that the peak amplitude of the THz pulse rises as the bias field increases. This suggests that an intense bias E-field is preferred for generating high power THz pulses. The trend of the increment in peak amplitude can be further divided into two regions. A linear relationship fitted the medium/high bias region ($U_{bias} \geq 60$ V). The peak amplitude of the THz pulse increases proportionally with the bias voltage. This is consistent with the analytical model in Sec. 2.1. In contrast,

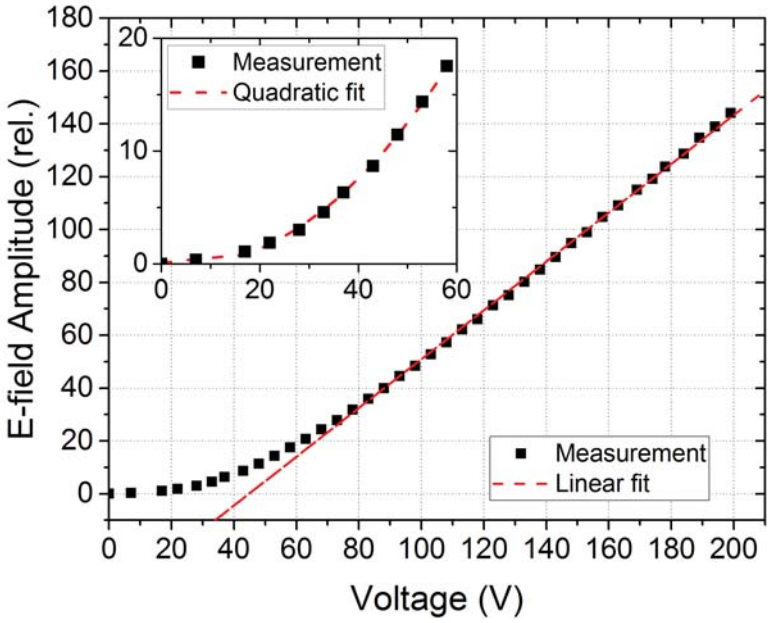

Figure 3.6: Evolution of peak amplitude with bias voltage ranging from 0 V to 200 V.

in the low bias region, the peak amplitude and the bias voltage follows a non-linear relationship, as illustrated in the inset.

Here two possible reasons for the presence of the non-linear region are proposed. One is the Schottky barrier at the electrode-semiconductor interface. The existence of the Schottky barrier introduces a turn-on threshold voltage, which could affect the linearity in low bias region. The other reason is the possible change in carrier dynamics due to the reduced bias field. To identify the origin of the non-linear region, the spectra of the THz pulses generated at different bias voltage are further analysed, as shown in Fig. 3.7.

Three traces of spectra are shown in Fig. 3.7(a). Two are in the aforementioned high bias region (U_1 = 199 V and U_2 = 98 V), and one in the low bias region (U_3 = 27 V). Overall, significant enhancement in dynamic range is realised as the bias field increases. This is consistent with the increased THz pulse peak amplitude. It is also observed that the spectra from lower biases experience stronger fluctuation, though the overall power distribution are similar.

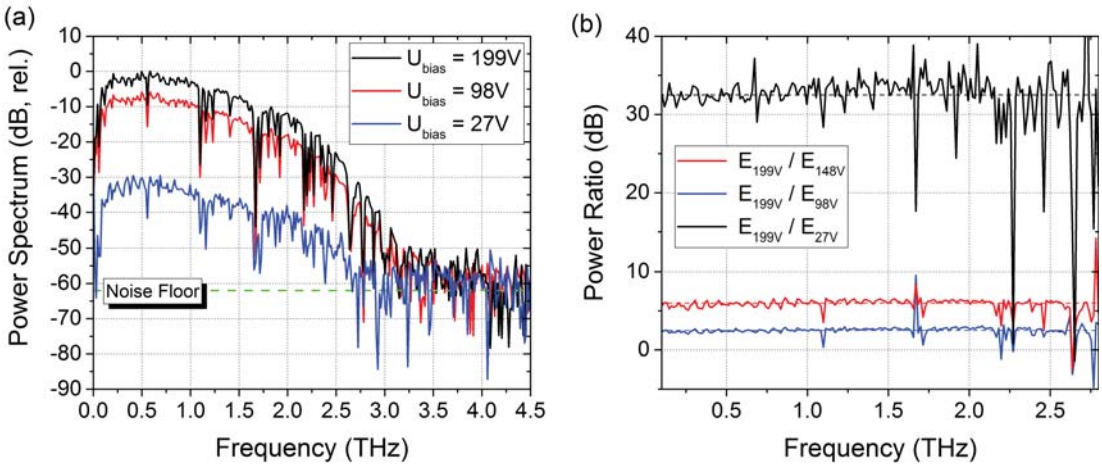

Figure 3.7: Spectrum analysis of THz pulses generated under different bias field. (a) Power spectra of THz pulses at different bias; (b) Spectral power ratio

Figure 3.7(b) demonstrates the spectral power ratio between the power spectrum of U_1 and that of lower bias voltages (U_2, U_3 and U_4 = 148 V). First, we focus on the scatter in the power spectrum. The fluctuation becomes more significant as the bias voltage drops, but frequency independent. This suggests that the fluctuations mainly come from external noise. As the signal amplitude decreases with the dropping bias, the influence of external noise becomes more significant. Next, the power spectrum ratio is considered. For high bias voltages, a stable trend in ratios of power spectra are realised in the frequency domain below 2.8 THz. On the other hand, for the low bias condition of U_3, a steady ratio can also be maintained beyond 2.0 THz. The strong fluctuation above 2.0 THz is due to the dramatically reduced dynamic range at low bias. Steady spectral power ratios in both high and low bias regions indicate that the change in bias field has negligible effect on the carrier dynamics. The non-linear region at low bias is caused by the Schottky barrier.

3.3.1.2 Field Distribution

In the photoconductive process a bias field is applied by an external voltage. The distribution of the external field over the biased area, however, is generally not uniform.

Considering that the amplitude of the THz pulse is dependent on the illuminated area of the bias, matching the illuminated area with the area of intense bias field distribution is beneficial for efficient THz wave generation. Therefore, mapping the bias field distribution is of great significance for the optimum operation of THz PCAs.

Optical excitation in the proximity of the anode is suggested to provide more intense THz radiation. The power ratio of THz radiation can be over 1000 between anode and cathode excitation [10, 11], indicating that most of the bias field is concentrated close to the forward biased semiconductor-electrode interface. This enhanced area is formed by the joint force of the metal-semiconductor contact and carrier dynamics in the semiconductor [12]. Commonly, Schottky contact is formed at the electrode-semiconductor interface. The anode interface is forward-biased. Upon optical excitation, free electrons can easily flow from the semiconductor to the metal electrode owning to the reduced barrier. A space charge area is then formed and adds to the bias field. This enhanced field is known as the trap-enhanced field (TEF). In contrast, the cathode interface is reverse-biased. The increased barrier potential makes it difficult for electrons to flow from the semiconductor to the electrode. Hence, TEF cannot be formed near the cathode interface. The existence of TEF is dependent on the band structure of the electrode material and semiconductor. By altering the electrode material, TEF can be strengthened or weakened [13–15].

Figure 3.8 demonstrates the measured excitation location-dependence of the generated THz radiation. Two PCAs of the same structure but fabricated with different electrode materials (aluminium and gold), are tested. The dimension of the biased region (electrode gap) is 500 μm. The antennas are gated with the same bias voltage and laser. The laser is focused to the dimension of $w \approx 50$ μm, and scans through the gap. The location is displayed by the displacement between the centre of the optical beam and the cathode-semiconductor interface d_{o-c}.

Strong excitation location dependence in the biased region is observed for the two

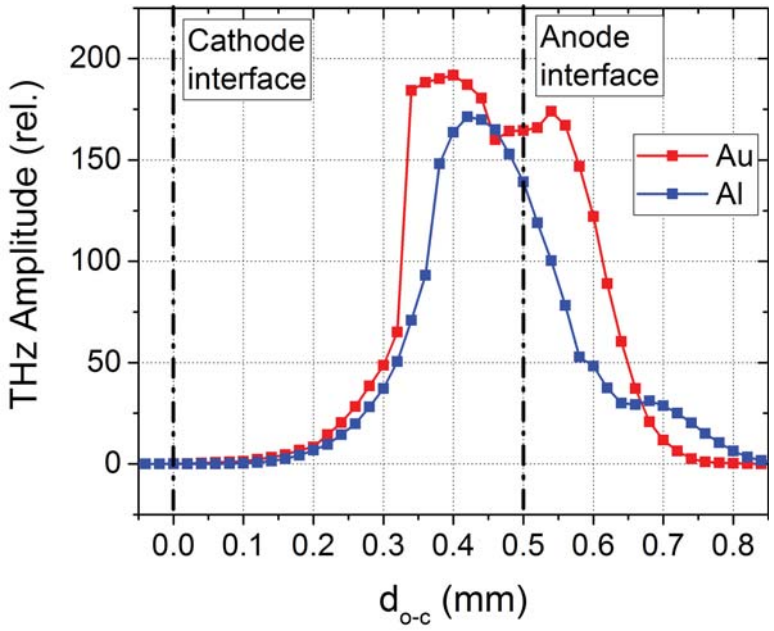

Figure 3.8: Excitation location dependence of THz PCAs with different electrode materials

studied electrode materials. When the excitation beam is focused on the cathode region, no measurable signal is realised; as the optical beam moves towards the anode-semiconductor interface, the signal amplitude increases rapidly. This suggests that Schottky contact is formed for both electrode materials. Power spectra are also recorded at half peak positions in both positive and negative directions. Stable dispersive power ratios to the peak spectra are observed. This indicates that the alteration in amplitude is due to the field distribution and amount of absorbed optical energy. Figure 3.8 also shows different excitation location-dependence for different electrode materials. Gold electrodes creates a larger amplitude of electric field, leading to a more intense THz pulse emission. For both the aluminium and gold electrode PCAs, the boost in field amplitude occurs in the near-anode region between $d_{o-c} = 0.3$ mm and $d_{o-c} = 0.4$ mm, while the increment with gold electrodes comes earlier in location, and is much sharper. For aluminium electrodes, the amplitude of the generated pulse starts to reduce as the optical beam moves out of the gap area. In contrast, with gold electrodes, the intense THz pulse can still be maintained in a small region even when $d_{o-c} > 500$ µm.

These superior characteristics of gold electrodes are assumed to be caused by the larger Schottky barrier at the metal-semiconductor interface. This leads to a larger depletion region, a more uneven field distribution across the gap, and a stronger TEF effect.

It should be noted that, near-electrode excitation can also lead to alteration in the field distribution of the excitation optical beam. As suggested in the work of P. G. Huggard *et al.* [16] and D. McBryde *et al.* [17], this alteration is dependent on the polarisation of the incident optical beam. At the electrode-semiconductor interface, localised enhancement in excitation intensity is realised for an optical beam polarised perpendicularly to the electrode edge. This enhancement is due to the discontinuity caused by the electrode structure, hence is not observed for parallel-polarised optical excitation. At the near-anode region, this enhanced excitation intensity can coincide with the TEF effect, resulting in a more intense THz radiation (more than 4 times in field amplitude as in [16]). In this work, however, the polarisation of the excitation optical beam is set parallel to the electrode edges, in order to solely reflect the alteration in bias field distribution corresponding to the TEF effect.

3.3.2 Optical Excitation Geometrics

In Sec. 3.2.1, the influence of the transient character of the optical pulse on THz radiation generation was discussed. Here, the influence of the spatial character of the excitation optical beam is examined. Compared to the transient characteristics, the spatial distribution of the excitation optics can be altered with simple optical components (*e.g.* lenses), therefore it is considered as an external excitation parameter. In the photoconductive process, a bias electric field is required to form the photocurrent. Hence, effective photo-excitation only takes place in the gap region formed by the electrodes. Focus now is on the profile of the optics within this area. The discussion focus solely focuses on the change in radiation power correlated to the change in excitation dimension. The influence of excitation dimension to the radiation character of THz

PCAs is treated as continuous PCA arrays, and are to be discussed in Chapter 5.

3.3.2.1 Theoretical Analysis

A theoretical analysis via an equivalent circuit model (ECM) is firstly performed. This model simplifies the radiation process into lumped circuit elements for ease of discussion. This approach has already been used for the study of THz PCAs by several researches. The model used in this study differs from others in regard to the following aspects:

1. **Radiation components.** In most analysis of THz PCAs with ECMs, the electrode structures are considered as transmitting antennas [18]. The excited photocurrent is considered as a current feed to the antenna structure. The radiated power is represented by the power coupled to the antenna impedance. This treatment, however, contradicts with the real radiation process. In reality, the THz pulse is mostly radiated by the time-varying photocurrent itself instead of the antenna structures (electrodes). This radiation character originates from the single-pulse nature of operation of THz PCAs and the relatively large electrode dimension comparing to the radiation wavelength. As a result, the resonances on the antenna structure are weak, and contributes little to the overall radiated power. In our model, the electrodes are simply considered as suppliers of bias field, and are assumed not to radiate, while the radiation component is restricted to the excited photoconductor.

2. **Radiation Impedance.** As discussed above, in existing ECM studies, the electrodes are considered as radiation components. The radiation impedance is therefore assumed to be determined by the electrode structure, and independent from the photoconductive process [18]. As our model incorporates the excited photoconductor as a radiating component, the radiation impedance is obviously related to the photoconductive process.

3. **Excitation dimension.** In most existing ECMs, the relative dimension between the optical excitation beams and the gap areas is omitted [1]. The gap areas are generally considered to be uniformly illuminated. In contrast, asymmetric optical excitation is commonly realised in practice. To represent this gap in our model, the effect of the optical beam dimensions are considered. For asymmetric excitation, the influence of the un-excited area is taken into account.

The ECM used in this study is illustrated in Fig. 3.9. The model simply consists of a bias voltage source U, the resistance of the un-excited area R_u, and resistance of the photo-excited area R_i and the radiation resistance R_r. Similar to the existing ECMs, the radiated power is represented by the power consumed by R_r. No reactance parts are included in this model. This simplification is based on the fact that the resonance in the radiation process is weak. The influence of reactance components is therefore insignificant. In addition, the uneven spatial distribution of the bias field caused by the TEF effect is not considered in this model, as it contributes to mostly the generation of the photoconductive current rather than the radiation of the THz wave.

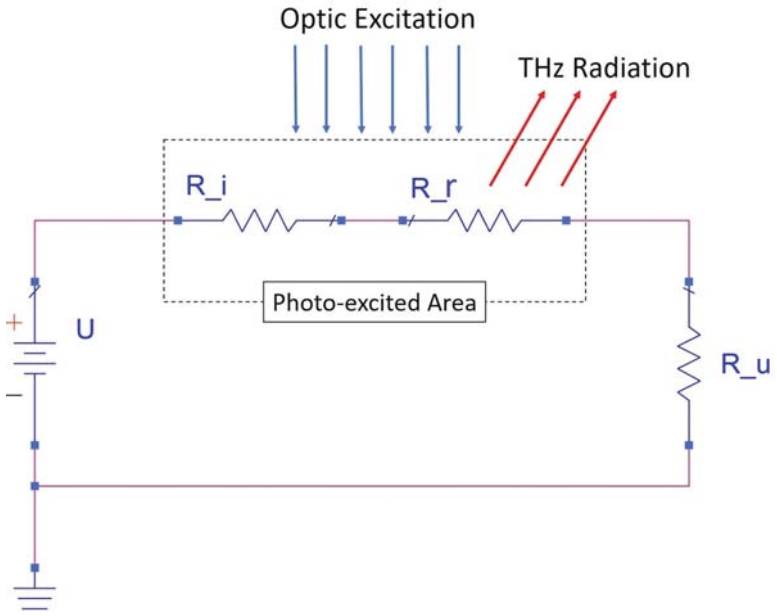

Figure 3.9: Schematic of the ECM. Optical excitation illuminates on the photo-excited area within the gap, while THz wave is radiated from the radiation impedance R_r

In general, the spatial distribution of the optical excitation is given to conform to a Gaussian distribution. In the model this is simplified to an ideal rectangular distribution with the length of d_i. The gap area has length d_g which is then divided into the excited area and the un-excited area with the length of $d_u = d_g - d_i$. As the excited and un-excited areas are isolated and considered as a package, this simplification will not affect the analysis.

The resistivity of the unexcited area is the dark resistivity of the photoconductive substrate ρ_u. The average resistivity of this area is assigned as $\rho_i(t)$. The resistances in Fig. 3.9 are,

$$\begin{aligned} R_i &= \rho_i d_i \\ R_u &= \rho_u d_u. \end{aligned} \tag{3.5}$$

The radiation impedance is correlated to the resistance of the excited area R_i through a radiation factor η_r,

$$R_r = \eta_r \cdot R_i. \tag{3.6}$$

For clarity of comparison, the average electric field E_{avr} across the gap is set to the same level. The bias voltage U then increase proportional to d_g as $U = E_{avr} d_g$. The power radiated from PCA P_{rad} is then,

$$P_{rad} = \left(\frac{U}{R_i + R_u + R_r} \right)^2 \cdot R_r. \tag{3.7}$$

Take Eqs. 3.6 and 3.6 into (3.7), the P_{rad} can be expressed as,

$$P_{rad} = \frac{E_{avr}^2 f d_i \rho_i}{\rho_u^2} \left\{ \frac{1}{1 + \frac{d_i}{d_g} \left[\frac{(1+\eta_r)\rho_i}{\rho_u} - 1 \right]} \right\}^2. \tag{3.8}$$

With regarding to the relative relationship between d_g and d_i, three different situations are considered: whole-gap excitation, infinitesimal spot of excitation, and an intermediate excitation spread. The discussions are reviewed as follows:

1. Whole-gap excitation: In this scenario, the gap is fully illuminated by the excitation optics. There is no unexcited area. $d_i = d_g$ and $d_u = 0$. As per (3.8), the radiated power is simply,

$$P_{rad} = \frac{E_{avr}^2 d_g}{(1 + \eta_r)^2 \rho_i}. \tag{3.9}$$

   Equation (3.9) suggests that, provided the same excitation intensity (same level of ρ_i) applies, the radiation power from PCAs can be amplified by increasing the gap dimension d_g. However, difficulties exist in practice. Firstly, to maintain the average bias field, the bias voltage is required to increase proportionally with d_g. This creates complexity in the bias circuit. More importantly, for whole-gap excitation, d_i varies in accordance to d_g. To maintain the same excitation

intensity, the optical power has to increase as d_g increases. This is rather difficult for an existing optical system.

2. Infinitesimal excitation dimension: This corresponds to the scenario of large-gap PCAs excited with a small-waist optical beam ($d_g \gg d_i$). The dimension of the unexcited area is $d_u \approx d_g$. Omitting the factor of d_i/d_g in the denominator in (3.8), the radiated power can then be expressed as,

$$P_{rad} = \frac{E_{avr}^2 f d_i \rho_i}{\rho_u^2}. \tag{3.10}$$

As indicated in (3.10), for infinitesimal area excitation, the radiated power is independent of d_g. Provided the same excitation intensity, P_{rad} can be amplified by simply expanding the optical beam spot d_i. Compared to whole-gap excitation, this requires only the increment of optical power. No change in d_g is required as long as the premise $d_g \gg d_i$ is satisfied.

3. Intermediate excitation dimension: This is the generalised situation when $d_g \sim d_i$. Here, the properties of the excitation optics (d_i and ρ_i) are fixed, and the influence of the gap dimension d_g on the radiated power is examed. According to (3.8), the trend of alteration is determined by the notation in the factor $k_\rho = \frac{(1+\eta_r)\rho_i}{\rho_u} - 1$:

   (a) When $\rho_i > \rho_u/(1+\eta_r)$, $k_\rho > 0$. P_{rad} increases as d_g increases. A limit is reached when $d_g \gg d_i$, corresponding to an infinitesimal area excitation.

   (b) When $\rho_i < \rho_u/(1+\eta_r)$, $k_\rho < 0$. P_{rad} increases as d_g decrease. Limitation is reached when $d_g = d_i$, corresponding to whole-gap excitation.

The value of ρ_i reflects the intensity of excitation. In practice, ρ_i is always smaller than ρ_u. High excitation intensity leads to large number of free carriers, and subsequently a reduced resistivity. The factor k_ρ can be regarded as evaluation parameters for the level of optical excitation. The discussion above therefore illustrates different

optimum excitation dimensions depending on the excitation level. For a high level of excitation, whole-gap illumination is preferred for maximum radiation power, while for low excitation level, a small optical spot is preferred.

The radiated power from these three situations is further compared assuming the same excitation optical energy (i.e., same value of R_i). The resistivity between the whole-gap excitation ρ_{i1} and the asymmetric excitation ρ_{i2} is connected through,

$$\rho_{i1} d_g = \rho_{i2} d_i. \tag{3.11}$$

For high excitation levels, whole-gap illumination yields stronger THz radiation. The ratio of radiated power between whole-gap and infinitesimal excitation is,

$$\eta_p = \frac{1}{\eta_r (1+\eta_r)^2} \cdot \frac{\rho_u^2}{\rho_{i1}^2}. \tag{3.12}$$

For a low level of excitation, an infinitesimal beam spot provides stronger THz radiation. The ratio of radiated power between the infinitesimal and whole-gap excitation is,

$$\eta_p = \eta_r (1+\eta_r)^2 \cdot \frac{\rho_{i1}^2}{\rho_u^2}. \tag{3.13}$$

3.3.2.2 Experiment Measurement

Here, experimental measurements are carried out to examine the above theorem. Specifically, the influence of gap dimension is examined on the radiated THz power.

THz PCAs with different length of gap dimensions are fabricated by photo-lithography on SI-GaAs wafers. The value of d_g ranges from 70 μm to 110 μm. Electrodes are made of thermally evaporated aluminium with the thickness of 60 nm. PCAs of different gap dimensions are situated on the same SI-GaAs wafer in proximity. This is to minimise the change in optical character upon excitation. The optical beam is focused by a lens

to a beam waist of approximately 50 μm, so that it can fit into the smallest gap used in the measurements. The dimension of the optical beam is kept the same throughout the measurement. This is to eliminate the interference from the spectral effect of optical beam waist. The average bias field is kept at $E_{avr} = 1.0 \times 10^4$ V/cm. The measured time-domain E-field amplitude of the THz pulses are shown in Fig. 3.10.

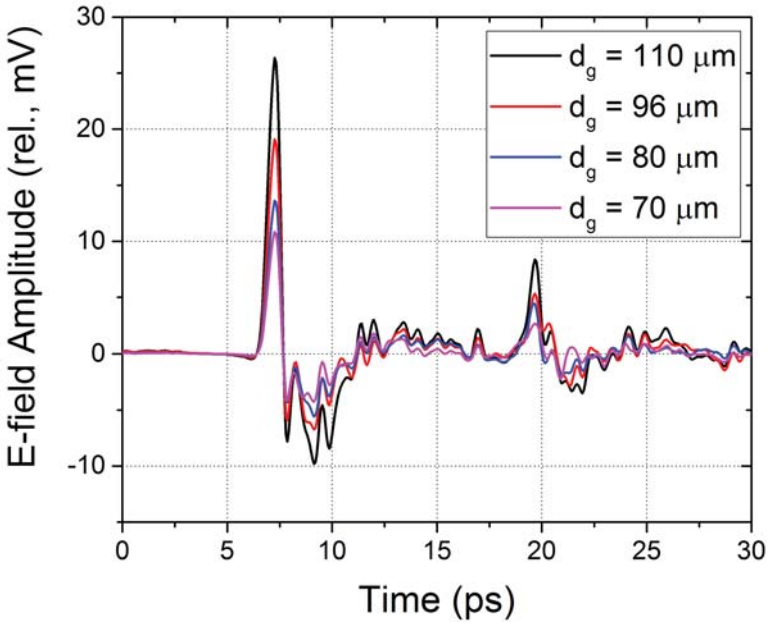

Figure 3.10: Time domain E-field of THz pulses generated from PCAs with different gap dimensions ranging from 70 μm to 110 μm

The measurement results show that the radiated power is enhanced as d_g increases. This corresponds to the low excitation scenario discussed above. From (3.8), the ratio of the radiated E-field η_{re} from PCAs with different dimensions d_{g1} and d_{g2} can be expressed as,

$$\begin{aligned} \eta_{re} &= \frac{E_1}{E_2} = \sqrt{\frac{P_{rad1}}{P_{rad2}}} \\ &= \frac{1 + \frac{d_i}{d_{g2}} k_\rho}{1 + \frac{d_i}{d_{g1}} k_\rho}. \end{aligned} \tag{3.14}$$

The excitation factor k_ρ can then be calculated by,

$$k_\rho = \frac{1}{d_i} \cdot \frac{1 - \eta_{re}}{\frac{1}{d_{g1}}\eta_{re} - \frac{1}{d_{g2}}}. \tag{3.15}$$

In the measurement, power spectra of the THz pulses in Fig. 3.10 are observed to be almost identical. This indicates that k_ρ is dispersionless. Table 3-B lists the values of k_ρ calculated according to (3.15) using all the measured η_{re}.

Table 3-B: Calculated excitation factors k_ρ

d_g (μm)	70	80	96	110
70	-	3.68	3.66	3.66
80	3.68	-	3.64	3.66
96	3.66	3.64	-	3.67
110	3.66	3.66	3.67	-

For different d_g and η_{re} combinations, the values of the calculated k_ρ are relatively stable. This proves the validity of the proposed model and theorem. For specific experiment environment of this thesis, the estimated excitation factor is $k_\rho = 3.66$, with a standard deviation of 0.012.

According to the results from our ECM, the threshold for high and low optical excitation is determined by the radiation factor η_r. It represents the ratio between the radiated power and the power dissipated as heat in the illuminated area. The measurement indicates that this function is dispersionless. According to the theorem, it can be measured by quantitatively controlling the excitation parameters (i.e., intensity or beam width).

3.4 Power Collection Efficiency in THz-TDS

The discussion above analyses the wave generation process of the broadband THz pulse inside the photoconductive substrate. After the generation process, the next step is to couple the THz wave to free space for practical implementations in the THz-TDS systems.

For RF frequencies, antennas are commonly used for this coupling process. RF antennas are generally designed based on the concept of resonance and oscillation. The radiation pattern of antennas can be manipulated by controlling the mutual interaction between the antenna structure and the EM wave. In contrast, resonance in THz PCAs is difficult to achieve due to the non-oscillation THz generation methods and the broad bandwidth of the radiation. The influence of the antenna structure has limited on the radiation pattern. Therefore, efficient coupling of THz radiation mostly relies on the method of power collection used in a given THz-TDS system.

In this section, an evaluation method for the power collection scheme in a THz-TDS system is developed. In practice, the specific power collection scheme operated on the THz-TDS bench in QMUL is evaluated and discussed.

3.4.1 Evaluation Method

The proposed evaluation method was carried out in the following steps:

1. Determine the radiation pattern inside the photoconductive substrate. This corresponds to the initial radiation from the photocurrent transient. In this study, the radiation pattern is approximated by the radiation pattern of an electric dipole, as illustrated in Fig. 3.11.

   This approximation is valid when the dimension of the source is much smaller than that of the THz wavelength ($d_i \ll \lambda_{THz}$). This approximation creates a

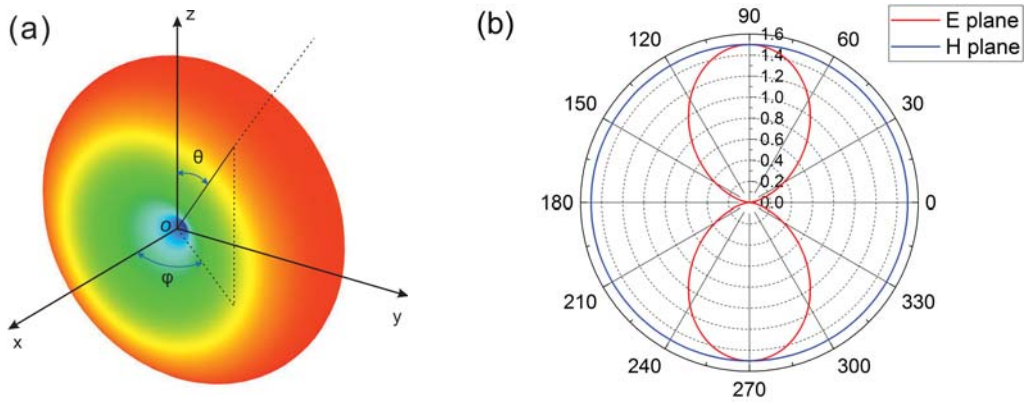

Figure 3.11: The radiation pattern of an electric dipole. (a) 3D radiation pattern; (b) E-plane and H-plane of the radiation pattern

frequency-independent radiation pattern, and simplifies the analysis. For the case of $d_i \sim \lambda_{THz}$, the radiation pattern becomes frequency-dependent, while the evaluation process remains the same.

2. Determine the maximum collection angles of the detection scheme. These angels represent the edge of power collection. They are jointly determined by the geometric layout of the collection scheme and the properties of the substrate material. Snell's law was applied at all interfaces for the calculation.

3. Calculate the transmission coefficient. Reflection and transmission will occur at all coupling interfaces, and ultimately the THz pulse propagated into free-space. In the majority of the spectrum of THz-TDS systems, commonly used components are considered lossless. According to Fresnel equations, the reflection and transmission coefficients of s and p polarised waves at the interface can then

be calculated as [19],

$$\begin{aligned} R_s &= \left| \frac{n\cos\theta_i - \sqrt{1-(n\sin\theta_i)^2}}{n\cos\theta_i + \sqrt{1-(n\sin\theta_i)^2}} \right|^2 \\ T_s &= 1 - R_s \\ R_p &= \left| \frac{n\sqrt{1-(n\sin\theta_i)^2} - \cos\theta_i}{n\sqrt{1-(n\sin\theta_i)^2} + \cos\theta_i} \right|^2 \\ T_p &= 1 - R_p. \end{aligned} \tag{3.16}$$

where θ_i is the incident angle, n is the refractive index of the dielectric at the interaction interface. The incident THz radiation is projected onto the two directions s and p to calculate the overall transmission efficient.

4. Calculate the overall collected power. The overall collected power was calculated by combining the radiation pattern of the THz source, the maximum collection angles and the transmission coefficients. Overall collected power is compared to the power radiated by the photocurrent to evaluate the collection efficiency.

3.4.2 Efficiency Evaluation of Parabolic Mirror Collection Scheme

The following evaluation method is used to assess the collection efficiency of the power collection scheme implemented on the THz-TDS bench at QMUL. The schematic of the layout is demonstrated in Fig. 3.12.

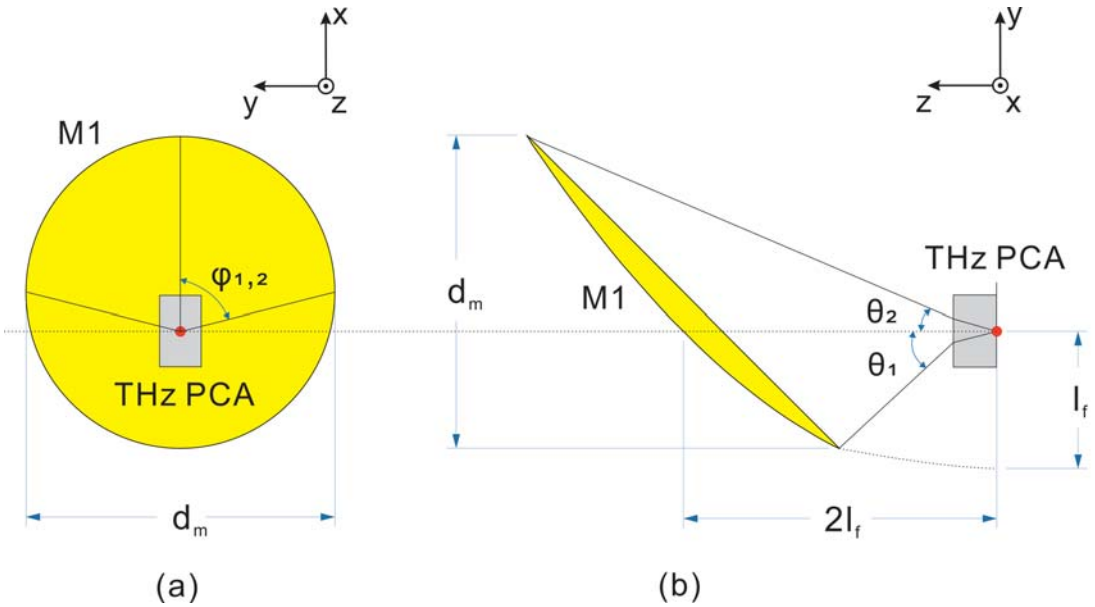

Figure 3.12: Schematic of parabolic mirror collection scheme and the maximum collection angles. (a) Front view; (b) side view.

In this set-up, a 90° off-axis parabolic mirror is used to collect THz radiation from the THz PCA. Ideally, the THz PCA is placed at the focus of the parabolic mirror $M1$. The effective focal length of the parabola is $2l_f$, where l_f is the focus of the parabola. The diameter of the parabolic mirror is d_m. The substrate in use is SI-GaAs with a relative permittivity of $\epsilon_r = 12.9$. The thickness of the substrate is ignored as it is much shorter than l_f and d_m. Taking into account of the refraction at the substrate-air interface, the maximum polar collection angles $\theta_{1,2}$ and azimuthal angles $\phi_{1,2}$ satisfy,

$$\begin{aligned} n_{GaAs}\sin\theta_1 &= \sin\left[\arctan\frac{1-(2-k_m)^2/4}{2-k_m}\right] \\ n_{GaAs}\sin\theta_2 &= \sin\left[\arctan\frac{(2-k_m)^2/4-1}{2+k_m}\right] \\ n_{GaAs}\sin\phi_{1,2} &= \sin\left[\arctan(k_m/2)\right], \end{aligned} \tag{3.17}$$

where $k_m = d_m/2l_f$. The maximum collection angles are then dependent on the ratio between the dimension of the parabolic mirror and its focal length.

Here we mainly study two orthogonal polarisations of the photocurrent: parallel to the x-axis and parallel to the y-axis as illustrated in Fig. 3.12. For photocurrent along the z-axis, the principle radiation direction lies along the y-axis. The power collected by $M1$ is extremely low, and therefore is not analysed here.

For photocurrent along the x-axis, the polar angle of the radiation pattern in Fig. 3.11(a) corresponds to the azimuthal angle in Fig. 3.12. At the GaAs-air interface, the s and p polarised field are,

$$\begin{aligned} E_{s1} &= E_{THz} \sin\phi \\ E_{p1} &= E_{THz} \cos\phi. \end{aligned} \tag{3.18}$$

For photocurrent along the y-axis, the polar and azimuthal angles in Fig. 3.11(a) align with those in Fig. 3.12. At the GaAs-air interface, the s and p polarised field are,

$$\begin{aligned} E_{s2} &= E_{THz} \cos\phi \\ E_{p2} &= E_{THz} \sin\phi. \end{aligned} \tag{3.19}$$

The dependence of the power collection efficiency η_c on the geometric parameter of the parabolic mirror k_m is calculated for these two scenarios. The results are shown in Fig. 3.13.

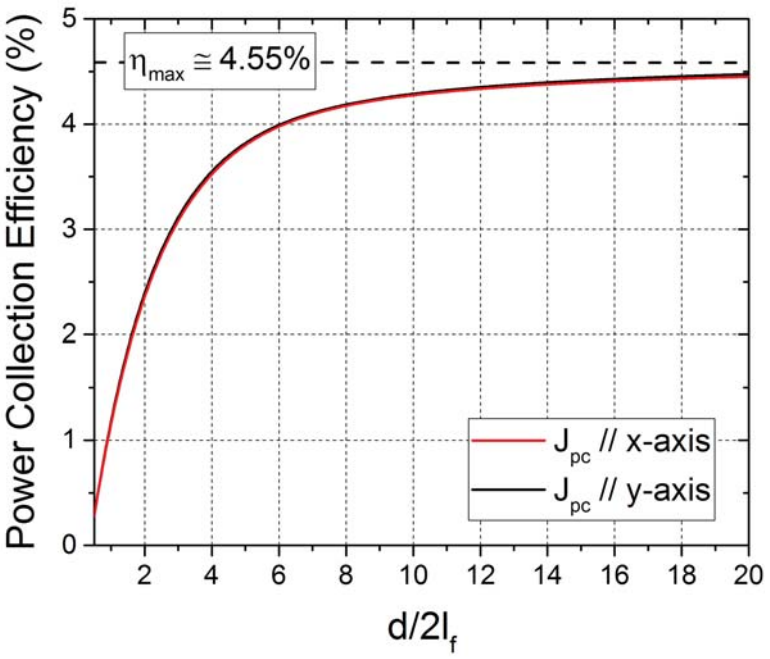

Figure 3.13: Collection efficiency of parabolic mirror collection scheme corresponding to different polarisation of photocurrent.

As illustrated in Fig. 3.13, for both polarisation directions, the collection efficiency increases as k_m increases. Very minor difference ($< 2\%$) in η_c are observed for the two photocurrent polarisations. The growth of η follows an exponential curve. At small k_m values (below 4), the growth rate of η_c is high. As k_m increases, the growth rate decreases. Ultimately, η_c saturates at a maximum of 4.55%.

3.4.3 Experiment Validation and Discussion

The validity of the evaluation method is tested experimentally by comparing the power collection efficiency of parabolic mirrors with different k_m parameters. Two parabolic mirrors $M1$ and $M1'$ were assessed experimentally. The diameters of the two mirrors are identical with $d_m = 5.08\ cm$. The focal lengths of the two mirrors were $l_{f1} =$ 2.54 cm and $l_{f2} =$5.08 cm. The k_m values of the $M1$ and $M1'$ were then $k_{m1} = 1$ and $k_{m2} = 0.5$.

Due to restrictions in experimental environment, $M1$ and $M1'$ were set to collect THz radiation from the opposite directions of the THz PCA. The schematics of back and front collection schemes are shown in Fig. 3.14.

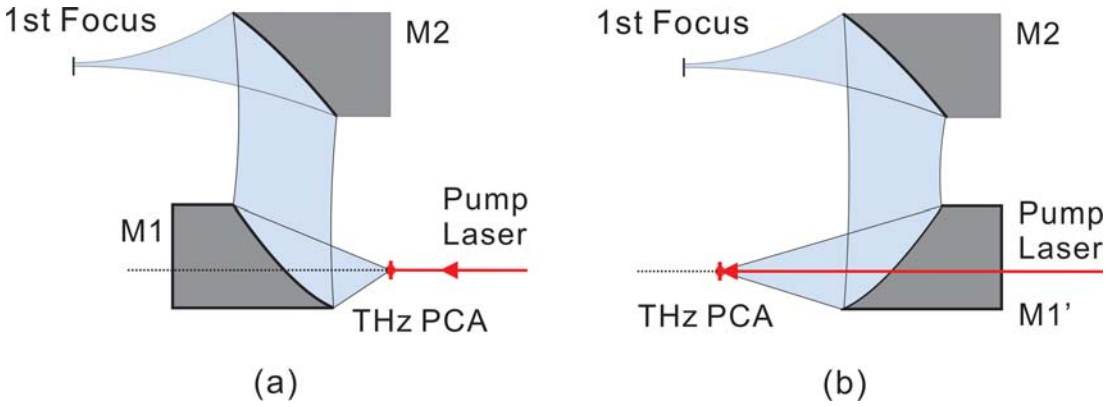

Figure 3.14: Schematics of back and front radiation layouts. (a) Back radiation; (b) front radiation

As the laser-induced photocurrent is generated inside the photoconductive substrate, the radiation processes for front and back radiation are identical. For both radiation directions, the THz wave encounters undergoes refraction at the substrate-air interface. As the measurement is in time domain, the influence of Fabry-Perot effect caused by the difference in distance of the photocurrent to the front/back interfaces is insignificant. As a result, the THz power radiated towards the two directions is considered to be equal (or comparable). The measurement results therefore mainly show the difference caused by the geometries of parabolic mirrors. The measurement results are displayed in Fig. 3.15.

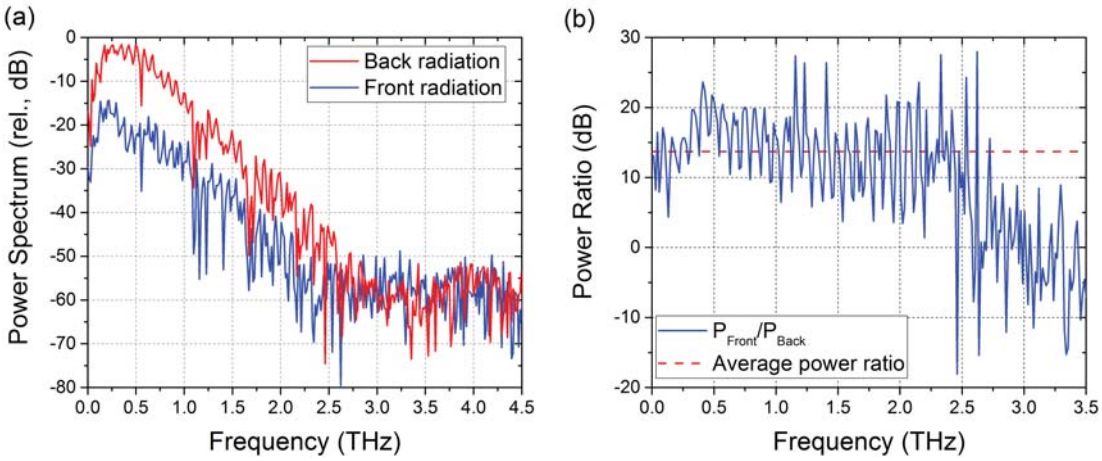

Figure 3.15: Comparison of detected THz signals from back and front radiation layouts. (a) Power spectra; (b) power ratio

Overall, the power spectra of the THz pulses collected by the two parabolic mirrors shown in Fig. 3.15 are similar. The backward radiation configuration provides a higher dynamic range owning to the higher diameter-focus ratio of $M1$. In the frequency range below 2.5 THz, an average power ratio of 13.73 dB is realised between the two power collection schemes. This value is in reasonable proximity to that calculated from the evaluation method, which is 11.59 dB. This confirms the validity of the evaluation method. The power collected by $M1'$ of front radiation is slightly lower than expected. This is most likely to be caused by the misalignment of the THz PCA, since the alignment by the front radiation scheme using a long-focus parabolic mirror is much more difficult in practice. The difference in alignment conditions may also be the reason for the above average power ratio observed around 0.5 THz.

The analysis with the model developed here suggests that parabolic mirrors with large diameters and small focal lengths are preferred for efficient collection of THz radiation. Parabolas with k values larger than 6 are recommended in order to realise an η_{max} of 90%. However, realisation and implementation of these large k_m mirrors are mechanically problematic. Generally, the k_m values for 90° off-axis parabolic mirrors are between 0.25 to 2. This results in a low collection efficiency with parabolic mirror

collection schemes.

It is also noticed that $\eta_{c,max}$ for the collection scheme is still relatively low. This is due to the high permittivity of the photoconductive substrate, resulting in a small critical angle at the substrate-air interface. Most of the radiated power is therefore trapped inside the photoconductive substrate. Substrate lenses can be used to overcome this problem. Such substrate lenses are generally fabricated with silicon to match the permittivity of the photoconductive substrate. The evaluation method here is also applied to calculate the power collection efficiency of this scheme for comparison.

Calculation is made with regard to an extended hemispherical lens with the radius R_{lens} and extended length d_{ext}. For efficient coupling and collimation of the THz wave, R_{lens} and d_{ext} satisfy the relationship [20],

$$\frac{d_{ext}}{R_{lens}} = \tan\theta_{c,Si}, \tag{3.20}$$

where $\theta_{c,Si}$ is the critical angle at the silicon-air interface. The THz PCA is assumed to be placed at the centre of the extended hemispherical lens. The refractions at both the GaAs-Si interface and Si-air interface are taken into account. The calculated power collection efficiency is found to be $\eta_{lens} = 41.1\%$. The result suggests that a Si lens collection scheme is much more efficient than parabolic mirrors. On the other hand, in practice, accurate alignment using Si substrate lenses is rather difficult. The power collection efficiency is generally lower than the ideal value.

3.5 Summary

In this chapter, a coherent performance characterisation of THz PCAs is presented. The characterisation method covers the main aspects of performance dependences of THz PCAs.

The influences of excitation parameters were first analysed and the parameters were categorized into intrinsic and external excitation parameters based on their role in the ultrafast photoconductive process.

The primary intrinsic excitation parameters studied are the transient profile of the excitation optics and the transient response of carriers in the photoconductive substrate. Their influences are firstly analysed individually with analytical parametric studies, and then compared with experiment results from literature. In summary, regarding on the excitation optics, short-pulse duration τ_p is preferred for broadband THz generation, but with dynamic range generally suffering. With regarding to photoconductive substrate material, the bandwidth and amplitude of the THz radiation is balanced through a compromise between carrier lifetime τ_c and mobility μ_e. The relationship between these two intrinsic excitation parameters is further discussed. Two optimum ratios are suggested. The selection of $\eta_1 = 0.1$ provides maximum bandwidth for the generated THz radiation, while $\eta_2 = 0.6$ provides intermediate bandwidth with close to maximum signal amplitude.

The extrinsic excitation parameters analysed are the bias electric field and the optical excitation geometry. For the influence of electric field, linear and non-linear relationships between bias and radiated THz energy is observed experimentally and discussed. The field distribution across the gap area is mapped experimentally, and the influence of electrode materials upon the bias field distribution is discussed. Metals with larger working functions provide lager depletion areas, and subsequently a higher trap-enhanced field. The influence of optical excitation geometry is studied by an equivalent circuit model. The model restituted the radiation components to the photocurrent with a radiation impedance correlated to the photoconductive process. The relative dimension of the optical beam to the electrode gap is also taken into account in the model. The result shows different optimum excitation strategy depending on the optical excitation intensity. For high optical excitation, whole-gap illumination is preferred, while for low optical excitation, an infinitesimal excitation optical beam pro-

vides higher radiated power. The theorem is examined and validated with experiment. The excitation factors of the specific experiment condition is measured.

After establishing the operational dependence of THz PCAs to the excitation parameters, an evaluation methodology is introduced to assess the power collection efficiency of the THz wave collection scheme in THz-TDS systems. Specifically, the parabolic mirror collection scheme is examined with this evaluation method. The calculation suggests that the power collection efficiency increases with the diameter-focus ratio k of the parabolic mirror. The maximum collection efficiency for this scheme is $\eta = 4.55\%$.The validity of this evaluation method is tested experimentally. This estimated power ratios of THz wave collected by different parabolic mirrors is in reasonable proximity with experimentally measured values. This proved the validity of this model.

References

[1] N. Khiabani, Y. Huang, Y.-C. Shen, and S. Boyes, "Theoretical modeling of a photoconductive antenna in a terahertz pulsed system," *IEEE Transactions on Antennas and Propagation*, vol. 61, no. 4, pp. 1538–1546, 2013.

[2] E. Moreno, M. F. Pantoja, S. G. Garcia, A. R. Bretones, and R. G. Martin, "Time-domain numerical modeling of THz photoconductive antennas," *IEEE Transactions on Terahertz Science and Technology*, vol. 4, no. 4, pp. 490–500, 2014.

[3] Y. Shen, P. Upadhya, H. Beere, E. Linfield, A. Davies, I. Gregory, C. Baker, W. Tribe, and M. Evans, "Generation and detection of ultrabroadband terahertz radiation using photoconductive emitters and receivers," *Applied Physics Letters*, vol. 85, no. 2, pp. 164–166, 2004.

[4] Y. Shen, P. Upadhya, E. Linfield, H. Beere, and A. Davies, "Ultrabroadband terahertz radiation from low-temperature-grown GaAs photoconductive emitters," *Applied Physics Letters*, vol. 83, no. 15, pp. 3117–3119, 2003.

[5] Y. S. Yung, "A tutorial on GaAs vs silicon," in *ASIC Conference and Exhibit,*

1992., Proceedings of Fifth Annual IEEE International, Sep 1992, pp. 281–287.

[6] I. S. Gregory, C. Baker, W. Tribe, M. Evans, H. E. Beere, E. H. Linfield, A. Davies, and M. Missous, "High resistivity annealed low-temperature GaAs with 100 fs lifetimes," *Applied Physics Letters*, vol. 83, no. 20, pp. 4199–4201, 2003.

[7] M. Tani, S. Matsuura, K. Sakai, and S.-i. Nakashima, "Emission characteristics of photoconductive antennas based on low-temperature-grown GaAs and semi-insulating GaAs," *Applied Optics*, vol. 36, no. 30, pp. 7853–7859, 1997.

[8] R. J. B. Dietz, M. Gerhard, D. Stanze, M. Koch, B. Sartorius, and M. Schell, "THz generation at 1.55 um excitation: six-fold increase in THz conversion efficiency by separated photoconductive and trapping regions," *Optics Express*, vol. 19, no. 27, pp. 25 911–25 917, Dec 2011.

[9] W.-D. Zhang, J. Middendorf, and E. Brown, "Demonstration of a GaAs-based 1550-nm continuous wave photomixer," *Applied Physics Letters*, vol. 106, no. 2, p. 021119, 2015.

[10] P. C. Upadhya, W. Fan, A. Burnett, J. Cunningham, A. G. Davies, E. H. Linfield, J. Lloyd-Hughes, E. Castro-Camus, M. B. Johnston, and H. Beere, "Excitation-density-dependent generation of broadband terahertz radiation in an asymmetrically excited photoconductive antenna," *Optics Letters*, vol. 32, no. 16, pp. 2297–2299, 2007.

[11] J. H. Kim, *Efficient terahertz photoconductive source*. ProQuest, 2008.

[12] S. E. Ralph and D. Grischkowsky, "Trapenhanced electric fields in semiinsulators: The role of electrical and optical carrier injection," *Applied Physics Letters*, vol. 59, no. 16, pp. 1972–1974, 1991.

[13] N. Vieweg, M. Mikulics, M. Scheller, K. Ezdi, R. Wilk, H.-W. Hübers, and M. Koch, "Impact of the contact metallization on the performance of photoconductive THz antennas," *Optics Express*, vol. 16, no. 24, pp. 19 695–19 705, Nov 2008.

[14] W. Shi, L. Hou, and X. Wang, "High effective terahertz radiation from semi-insulating-GaAs photoconductive antennas with ohmic contact electrodes," *Journal of Applied Physics*, vol. 110, no. 2, 2011.

[15] W. Shi, L. Hou, Z. Liu, and T. Tongue, "Terahertz generation from SI-GaAs

stripline antenna with different structural parameters," *Journal of the Optical Society of America B*, vol. 26, no. 9, pp. A107–A112, Sep 2009.

[16] P. Huggard, C. Shaw, J. Cluff, and S. Andrews, "Polarization-dependent efficiency of photoconducting THz transmitters and receivers," *Applied Physics Letters*, vol. 72, no. 17, pp. 2069–2071, 1998.

[17] D. McBryde, M. E. Barnes, S. A. Berry, P. Gow, H. E. Beere, D. A. Ritchie, and V. Apostolopoulos, "Fluence and polarisation dependence of GaAs based Lateral Photo-Dember terahertz emitters," *Optics Express*, vol. 22, no. 3, pp. 3234–3243, Feb 2014.

[18] C. W. Berry and M. Jarrahi, "Principles of impedance matching in photoconductive antennas," *Journal of Infrared, Millimeter, and Terahertz Waves*, vol. 33, no. 12, pp. 1182–1189, 2012.

[19] J. D. Jackson, *Electrodynamics*. Wiley Online Library, 1975.

[20] D. F. Filipovic, S. S. Gearhart, and G. M. Rebeiz, "Double-slot antennas on extended hemispherical and elliptical silicon dielectric lenses," *IEEE Transactions on Microwave Theory and Techniques*, vol. 41, no. 10, pp. 1738–1749, 1993.

Chapter 4

Alignment Sensitivity Analysis of THz-TDS System

In this chapter, the influence of alignment error to the operation of THz-TDS systems is analysed. Specifically, the work here focuses on the misalignment of the broadband THz source in the quasi-optic subsystem. A numerical simulation model is built in combination with experimental measurements to assess the source alignment sensitivity.

4.1 Introduction

In Sec. 2.4, the systematic errors in THz-TDS systems were discussed regarding to SNR level. In practice, besides systematic errors, the measurement accuracy with THz-TDS technique is also bounded by other factors [1, 2].

One of the major sources of errors is the the alignment of components within the system. Multiple research has addressed the influence of optical misalignment. Misalignment in the pump and probe path were shown to cause attunuation and distortion in the generated and detected THz signals [3, 4], while alignment errors in the delay con-

trol scheme were considered responsible for drift in the frequency domain response [5, 6]. Nevertheless, the influence of optic misalignment can be minumised with routine optical alignment techniques [7], or by implementing fibre-coupled excitation and detection schemes [8]. The real difficulties lie in the alignment of the quasi-optic subsystems within general THz-TDS schemes, since THz spectrum is invisible, yet little efforts have focused on this aspect.

Here, a systematic methodology is proposed to investigate the alignment sensitivity of the QO subsystems. The analysis here is centred on the misalignment of the broadband THz source, while the principle of the shown analysis can be generally adapted for the study of other components in the QO path. The significant of this choice is from two folds. Firstly, the THz source serves as the first component in the QO subsystem. The alignment of other components relies on a correctly-situated source. Secondly, this is increasingly pertinent regarding to the efforts of increasing the radiation aperture of THz source to enhance the radiation power [9]. Illustrating the tolerance of THz-TDS systems to source misalignment will provide guidelines and design limits for such approach.

4.2 Methods

In this study, an EM simulation model was built to visualise the beam-field of the QO path in THz-TDS systems. The layout and geometric parameters were selected with reference to the THz-TDS system operated in QMUL. A schematic of the QO sub-system is shown in Fig. 4.1.

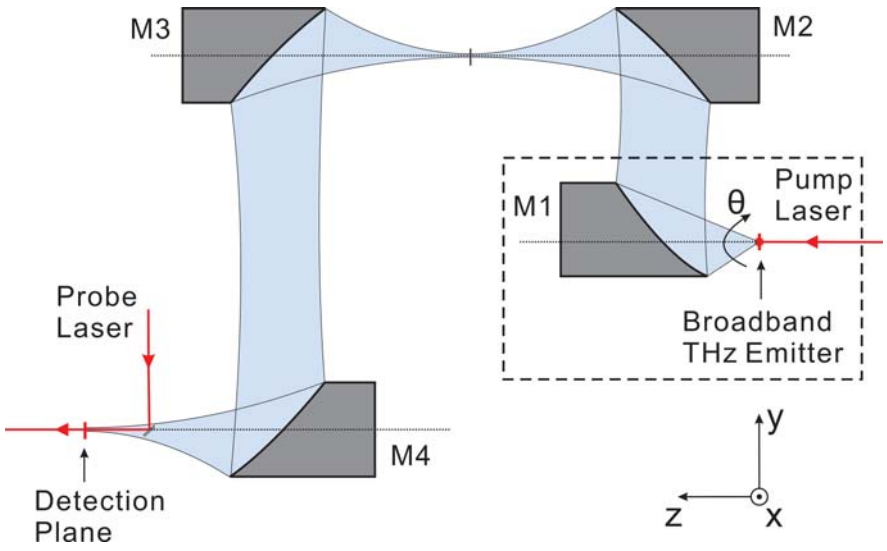

Figure 4.1: Schematic of the simulated QO system

In the QO sub-system, the broadband THz pulse generated by an SI-GaAs-based photoconductive antenna is guided by four parabolic mirrors. A focus is established between mirrors M2 and M3, and a collimated beam between mirrors M3 and M4. M4 provides a focus for the beam-field onto the EO-based detector.

The simulation was built with the electromagnetic CAD package, FEKO. The plane normal to the beam axis and at the focus of mirror M4, is defined as the detection plane over which the electric field is sampled during the measurement. It corresponds to the location where the coherent detection occurs. In the simulations, an electric dipole is used to represent the radiated field from the THz source. The radiation pattern of the dipole is shown in Fig. 3.11. This approximation is valid to a general extend since the radiation pattern of most broadband THz sources is considered to be similar to that of an electric dipole due to the lack of resonance [10]. The spectral domain of study is 100 GHz to 3.0 THz (with a 14 GHz step interval); the typical span of a picosecond pulse. The step-interval matches the common spectrum resolution of a 1024-sample scan having a 10 μm step for the translation stage. The electrically-large dimensions of components in the train of optics, precludes the computationally demanding dense

meshes of full-wave analysis and high-frequency asymptotic overhead for physical optics (PO) analysis. As a result, a geometric optics (GO) optics solver is selected to model the system. The model is solved in the frequency domain, but can be transformed for transient response studies.

The following constrains and post-processes are applied to the simulated model to correctly represent the response in THz-TDS systems:

1. A finite number of wave-surface interactions is set for each mirror in recognition of the coherent nature of detection;

2. The contribution of electric field from insufficient shadowing between mirrors is calculated and subtracted;

3. Only x-axis polarisation is measured. This is consistent with the configuration of the simulated THz-TDS bench.

By idealising the source to an electric dipole, misalignment can be quantitatively described in terms of its location and orientation. As the work here focuses on the influence of source misalignment, all the parabolic mirrors were assumed to be correctly positioned in the EM model. The case of perfect alignment of the source refers to its location at the focus of M1, while the orientation of the dipole is normal to the beam axis. The same coordinate system as in Fig. 3.12 was assigned to the simulation model. The origin is set at the focus of M1, where the dipole source is placed. The following sections assess misalignment of the emitter.

4.3 Electric Field Response in Frequency and Time Domains

4.3.1 Simulation Results

The focus in this study first lies on the response of E-field, sampled at the focus of mirror M4, due to misalignment of the THz source. The misplacement of the source can be categorised in terms of lateral and angular displacement. Their influence will be investigated in turn in this section. Position error was studied in off-set steps of 0.1 mm along each axis, in both positive and negative directions. The maximum off-set is set in correspondence to the wavelength of 1.0 THz ($\lambda_c = 0.3$ mm), which can be considered as the centre of the operation spectrum of the simulated THz-TDS system. The wavelength at 1.0 THz is used to characterise the location off-sets in the remainder of this section. For angular errors, only rotation in the polar angle was considered, as the radiation pattern of an electric dipole is azimuthally symmetric. The amplitudes of the electric fields were normalised with regard to the case for perfect alignment for a clear demonstrate on the effect of misalignment. The results from simulations are shown in Fig. 4.2.

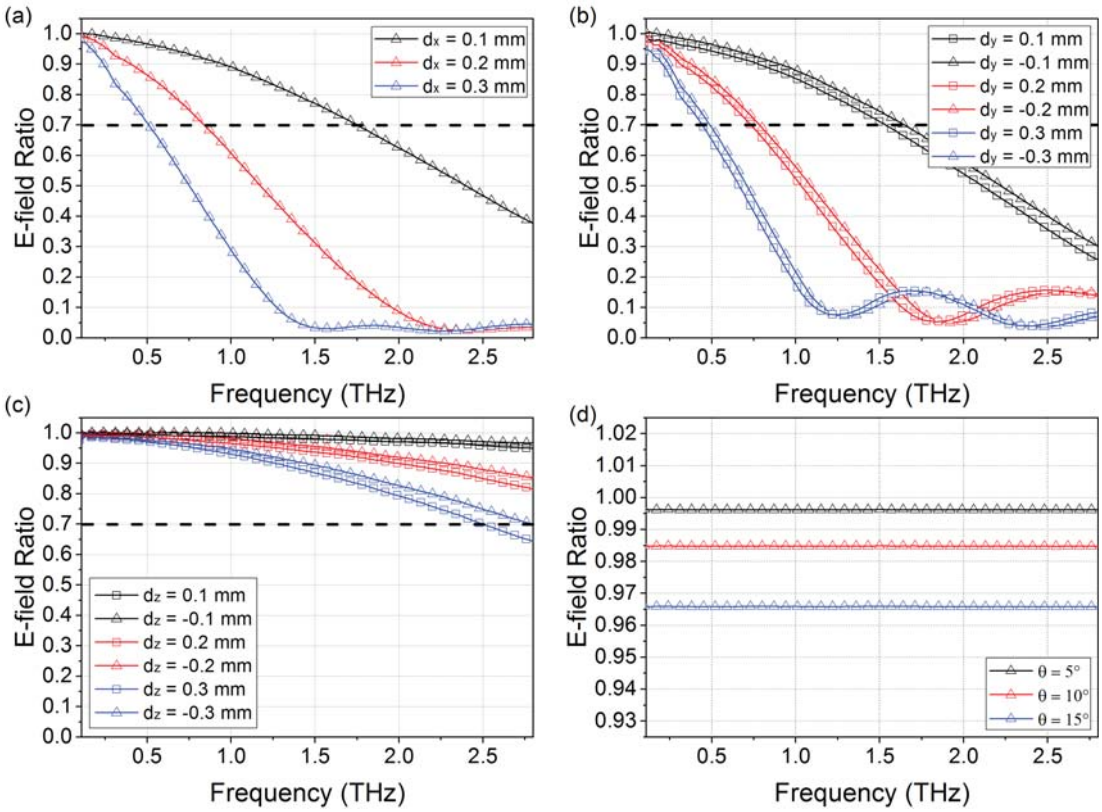

Figure 4.2: The relative amplitude of E-field at the detection point with regard to lateral error in (a) the x-axis; (b) the y-axis; (c) the z-axis and (d) polar rotation. Results in only one direction are plotted in (b) and (d) owing to symmetry about the yz plane. Dash line is set at 0.7 in (a)-(c), corresponding to half in power.

The results in Fig. 4.2 illustrates different dependences of E-field alteration to alignment error in different directions. Overall, the amplitude of E-field at the detection point decreases with the increasing alignment errors, while position and angular errors shows different characteristics. High frequency components were observed to be much more sensitive to position errors. For instance, a displacement of $d_x = 2\lambda_c/3$ results in an 18% fall in E-field amplitude at 0.5 THz, 47% at 1.0 THz, and up to 90% at 2.0 THz. This follows from the shortening wavelength with increasing frequency. The

given displacement means a longer electrical distance for smaller wavelengths, leading to a dramatic change in the electric field distribution and amplitude. Further, comparing plot (a) to plots (b) and (c), a relatively more stable response in E-field for misalignment along the beam axis (z-axis) was observed. Up to 70% E-field amplitude (approximately half in power) held up to 2.5 THz for a displacement of $d_z = \lambda_c/3$. In the transverse directions (xy-plane), however, the same proportional error could only be suffered up to around 0.5 THz. The stable response in E-field along the beam axis is attributable to the relatively short focal length of M1, creating a large angle-of-acceptance for the dipole source. In contrast, as shown in Fig. 4.2(d), the attenuation in E-field caused by angular misalignment is insignificant. Less than 5% of change was observed with a polar rotation error of 15°. Meanwhile, the relative change in amplitude is not dispersive, as the radiation patterns for all studied frequencies were set the same.

With regard to the coherent time-domain characteristic of THz-TDS systems, transient analysis is now examined based on the frequency domain results. A pulse excitation signal was generated in accordance to the analytical model described in Sec. 2.2. The optic pulse length was set as $\tau_l = 100$ fs and the carrier lifetime was $\tau_c = 500$ fs, in correspondent to typical values for many THz-TDS systems. Using these values, a THz pulse signal was generated that provides a sufficient coverage of the simulated frequency domain. The transient response at the detection point for offset errors of the source and the corresponding spectra are shown in Fig. 4.3.

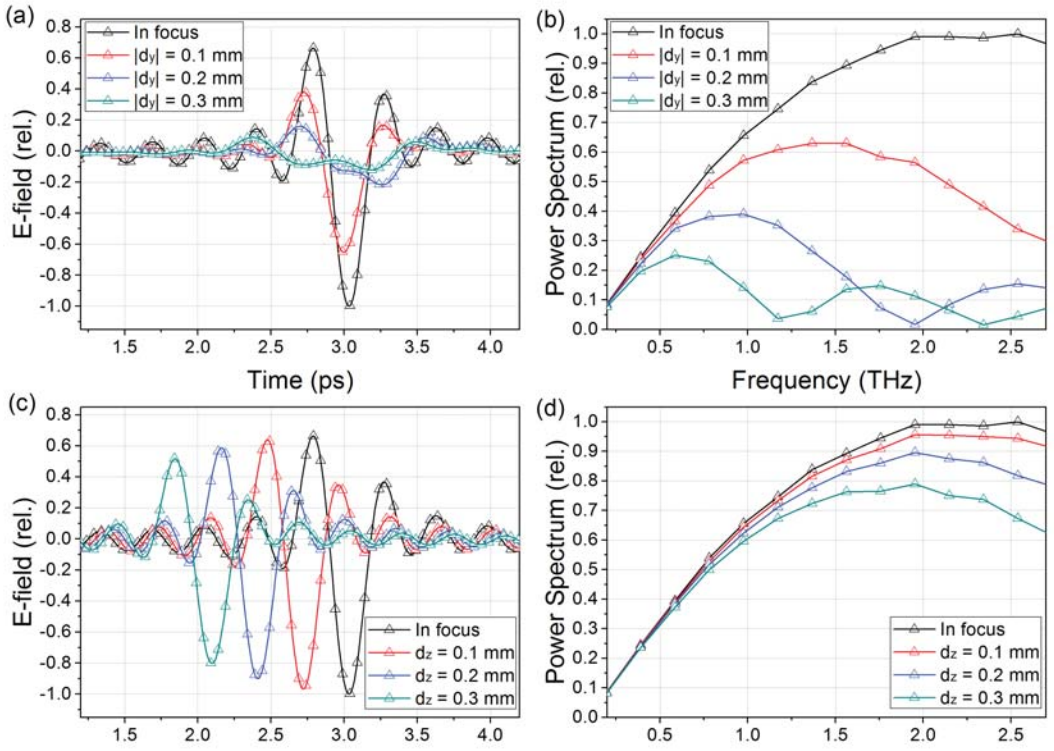

Figure 4.3: Transient respond of at the detection point in the simulated THz-TDS system and the spectrum of the recieved signal, considering the displacement transverse to (Plots (a) and (b)) and along the optic axis (Plots (c) and (d)) of parabola $M1$

In Fig. 4.3 the transient response of the in-focus scenario is denoted by the black traces for a clear comparison. Fig. 4.3(a) shows the distinct sensitivity of offset error in the xy-plane. Shifts of peak position in time-domain were observed, corresponding to change in effective path-length. This shift was relatively small (0.03 ps for $d_y = \lambda_c/3$ and 0.21 ps for $d_y = -2\lambda_c/3$), as the displacement is transverse to the optic axis, and is relatively small compared to the focal length of M1. Besides the shift in peak position, the signal also experienced a strong distortion. The peak amplitude dropped to 75% when $d_y = \lambda_c/3$, and further to 8% when $d_y = -\lambda_c$. The pulses were also seen to broaden corresponding to the loss of high frequency components. A frequency

representation (Fig. 4.3(b)), indicates that above 1.5 THz energy is lost for offset errors greater than $2\lambda_c/3$. This also concurs with the initial frequency-domain analysis. Now consider the case of error along the beam axis. The sensitivity of peak position is more pronounced, as shown in Fig. 4.3(c). Meanwhile, the amount of time-shift is proportional to the displacement, corresponding to the time-of-flight of light. Distortion of the signal was apparent, but less significant. The peak amplitude was only lowered by 10% for a displacement of λ_c. Moreover, no split was observed in the peak. The pulse maintained approximately the same shape throughout. The associated low frequency component below 1.0 THz was immune to off-set error in the source. Significant changes only occur above 1.5 THz. For transient response corresponding to rotation error, the signal merely coincides with the error-free case response. No shifts in peak location were observed, as there was no change in path length of pulse propagation. The distortion and decrease in amplitude of the pulse were also negligible as expected.

In the simulation results from this study, it is shown that the influence of angular errors in THz source was insignificant to the detected signal. This is due to the radiation characters of the THz source used in the simulation model. As shown in Fig. 3.11, the 3-dB beam width of an electric dipole in the polar direction is 90°. This is above the full receiving angle of M1 (53.1°). As a result, the alteration of power in the angular receiving cone of M1 is insensitive to polar small angular rotation of the electric dipole. In practice, the influence of angular errors is related to the radiation scheme used in the specific THz-TDS system. For highly directional radiation scheme (such as substrate lenses [11]), angular misalignment can be catastrophic to the detected THz signal.

4.3.2 Experimental Measurements

The effect of source misalignment to the detected THz signal is demonstrated by experiment. The position errors of THz emitter along the z and y axes were selected for demonstration, corresponding to displacement parallel and transverse to the beam axis.

In the measurements, misalignment along the beam axis was realised by altering the distance between M1 and the THz PCA by a 0.5 mm interval. Unfocused laser beam was used for excitation in order to create a uniform optical illumination condition for all emitter locations. The measurement results are shown in Fig. 4.4.

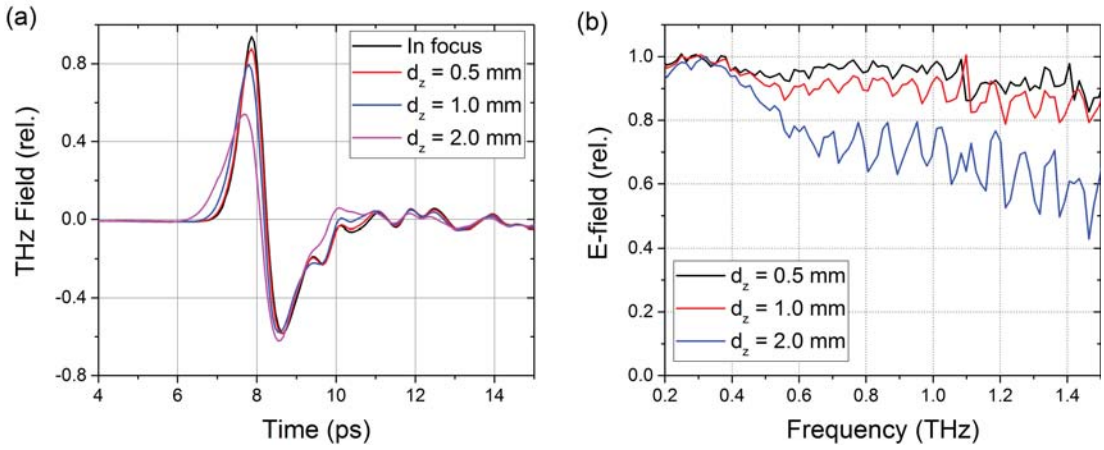

Figure 4.4: The influence of source misalignment along the z-axis to the detected THz signal. Plot (a) shows the recorded THz field in time domain; Plot (b) shows the ratio of the E-field amplitude to the in-focus scenario.

Different from the simulation results, the shift in peak position observed in measurements is insignificant, as shown in Fig. 4.4(a). The reason is that, with the specific experiment set-up, the alteration is the QO path length is mostly compensated by the alteration of the path length of the pump optic beam. Overall, no significant alteration in path length difference is realised between the pump and probe paths. Nevertheless, reduction in signal amplitude and widening of pulse width were both observed. These indicate the power loss of high frequency components. The measured trends of E-field ratio to in-focus situation are similar to that realised by simulation illustrated in Fig. 4.2(a). Due to limitations in the experimental environment, it is difficult to precisely realise intervals of d_z within 0.3 mm. However, the measured E-field ratio

at $d_z = 0.5$ mm is reasonably close to the simulated curve at $d_z = \lambda_c$ (but constantly roughly 3% lower). This can be considered as in good agreement with the simulation results.

Next the influence of location error transverse to the beam axis is examined. Instead of moving the THz emitter, the misalignment along y-axis was realised by moving M1 along y-axis. This approach can avoid the realignment of optical pump beam, whilst maintaining the same optic excitation condition. The location of M1 was altered by a 0.25 mm interval. The measurement results are shown in Fig. 4.5.

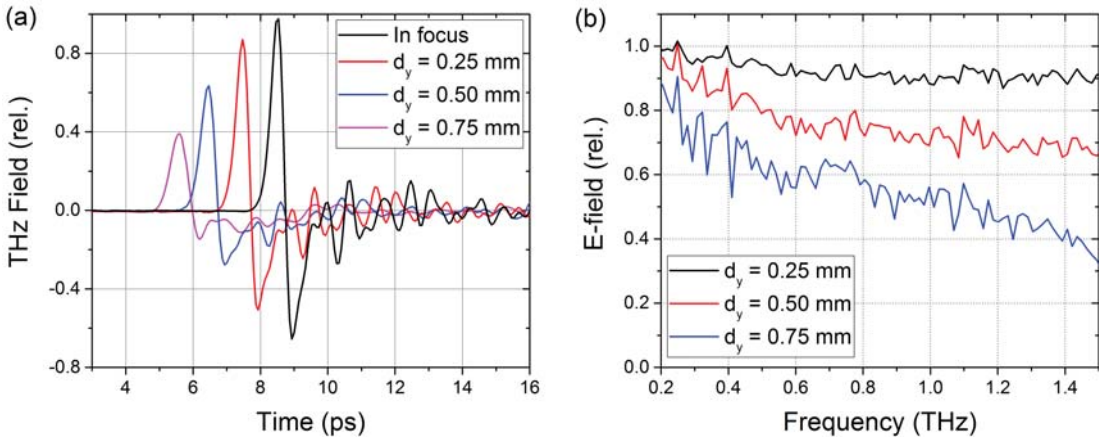

Figure 4.5: The influence of source misalignment along the y-axis to the detected THz signal. Plot (a) shows the recorded THz field in time domain; Plot (b) shows the ratio of the E-field amplitude to the in-focus scenario

In this scenario, shift of THz peaks in the time domain was observed by experiment. On the other hand, the amplitude of the electric field was much higher than the simulated values. Simulation results indicates a drop in E-field amplitude of more than 70% at 1.0 THz for $d_x = 0.3$ mm, while the measured drop in the experiment was only 12%. This vast difference is contributed by the finite dimension of the probe beam in the coherent detection scheme. Comparing to the infinitesimal probe at the focus of

M4 in the simulation, an optical probe beam of finite dimension can interact with and detect the E-field in the proximity of the focus. This results in an increased detected field. Therefore, in practice, a large optic probe beam is beneficial for suppressing the location error of THz source transverse to the optic axes.

The measurement results show a different influence on source location error parallel and transverse to the beam axis. For location error parallel to the beam axis, its influence can be correctly represented by the E-field response at the detection focus. In contrast, for location error transverse to the beam axis, its influence in the detected signal is determined by the E-field distribution in the detection plane.

4.4 Field Distribution

As discussed in the last section, the E-field distribution can play a significant role in the detected THz signal In this section, the dependence of E-field distribution of position error is mapped and analysed.

Figure 4.6 illustrates the E-field distribution in the detection plane for various scenarios of phase-centre error. The simulation results shown are of a 1.0 THz source, whilst similar patterns are also observed over the studied frequency range. The detection plane is normal to the beam axis at the focus of M4.

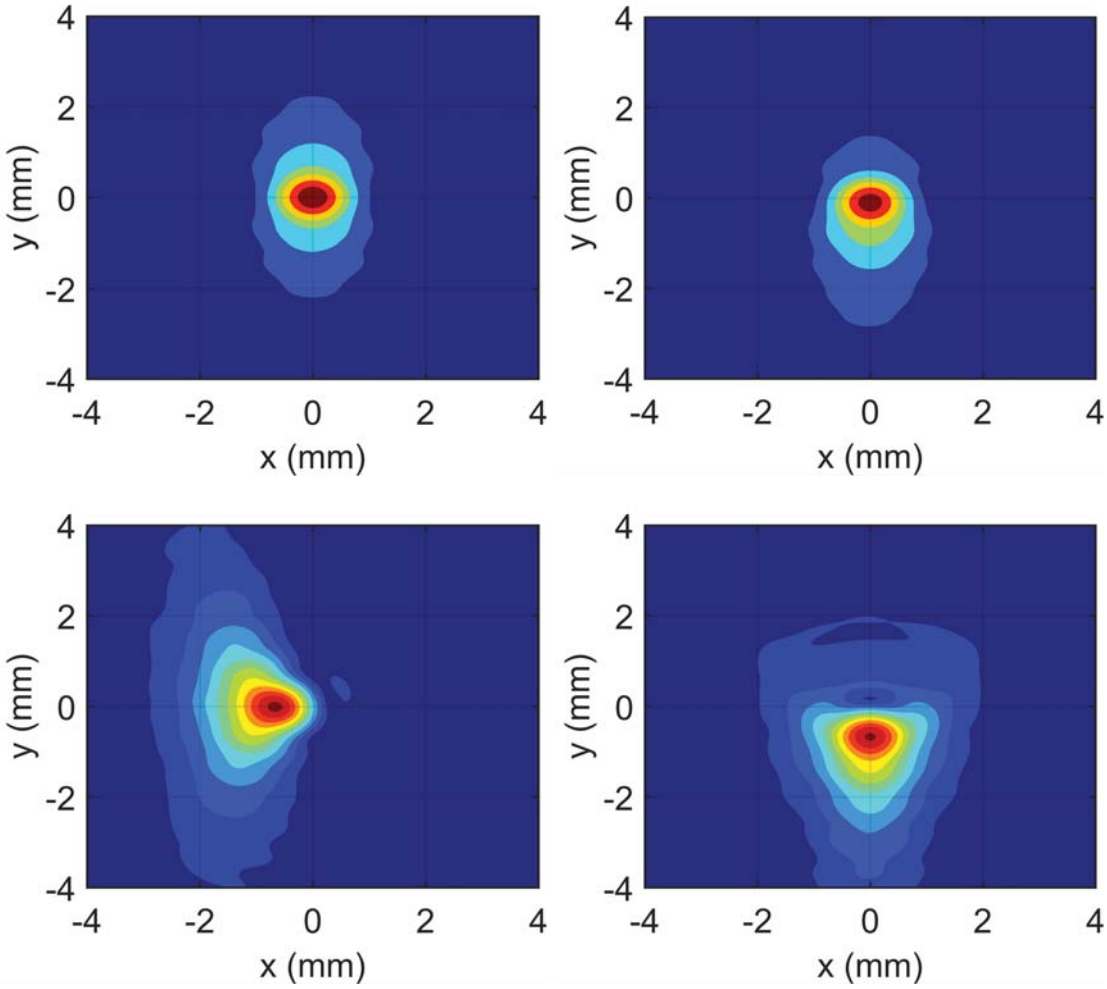

Figure 4.6: Simulated E-field distributions at 1.0 THz in the detection plane for different source locations. Plot (a) is for an ideally-set source; plots (b), (c) and (d) correspond respectively to off-set errors of $d_z = \lambda_c$, $d_x = \lambda_c$ and $d_y = \lambda_c$.

The zero-error case yields an elliptical E-field distribution, in agreement with experiment observations [12]. The asymmetry in x and y are traceable to the geometric surface profile of the parabolic mirrors. For offset error along the beam axis (the z-axis), the field maximum was still close to the focus. No movement of the peak along the x-axis was realised, while a small drift of $d_{drift} = 0.12$ mm along y direction. This drift

is considered to be caused by diffraction originating from uneven illumination of M1 along the y-axis. This can be confirmed by the fact that the drift-distance decreases as frequency increases. In contrast, the movements of the source in the transverse plane results in a much more obvious drift of the peak position. This is in consistent with the conclusion in Sec. 4.3, and helps explain the more significant drop for offset error along the axes normal to the beam axis. This drift displacement of phase centre d_{drift} was found to be non-dispersive, and approximately follows the relationship in (4.1).

$$d_{drift} = -\frac{f_{M4}}{f_{M1}} d_e, \tag{4.1}$$

where d_e is the displacement of the emitter from optimal location, f_{M1} and f_{M4} are the focus lengths of the $M1$ and $M4$, respectively. This is very similar to the lens equation, providing the expected location of maximum field due to positional-error of the source. Equation (4.1) also gives insight into the paradox regarding to the choice of the first parabolic mirror for a THz-TDS system. As concluded in Sec. 3.4, a parabola with short focal length is generally preferred in order to enlarge the receiving angle. However, this will also magnify instability in the system. In addition to the drift in peak position, Fig. 4.6 also shows changes in field distribution caused by offset error in the source. The change in field distribution can be considered in two ways, namely, an expanded beam size, and a change in beam-mode content. These two aspects will be discussed in the following subsections.

4.4.1 Beam Waist Expansion

The expansion of beam size is firstly addressed. The half-waist is calculated in reference to the peak amplitude in the detection plane, and is calculated along both x and y axes. The evolution in the size of the beam waist, corresponding to emitter position, is presented in Fig. 4.7.

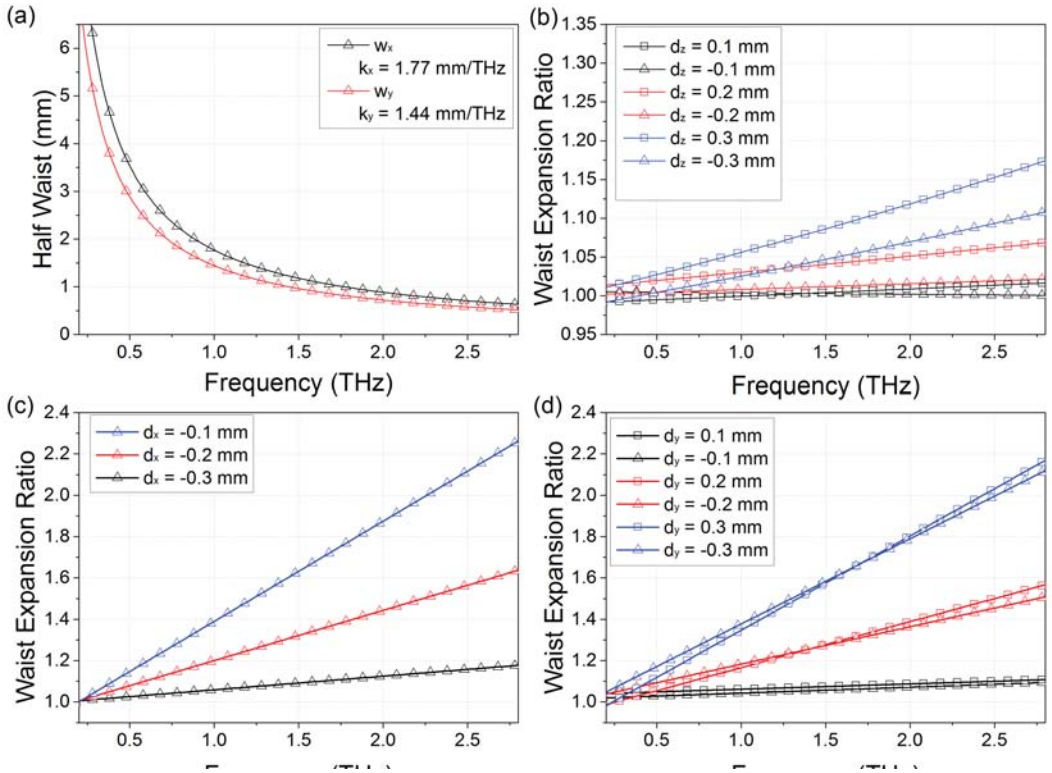

Figure 4.7: The evolution of beam-waist size with frequency. Plot (a) portrays the evolution of w_x and w_y for the situation of ideal alignment; plots (b) to (d) show the level of expansion of the beam-waist size corresponding to misalignment of the source in z, x and y directions, respectively.

Over the domain of frequency studied, the beam-waist tightens as frequency increases, regardless of the position of the source. For an ideally-set source, the trend of waist decrement fit to $1/f$ curves in both x and y directions, as illustrated in Fig. 4.7(a), consistent with the theory of Gaussian beam propagation. The ratio between the coefficients in the two orthogonal directions, $k_x/k_y = 1.23$, matches the theoretical value calculated according to the geometric parameters of M4 [13].

The relative expansion ratio of beam-waist size is then calculated for the scenario of

positional error of the source. The pattern of expansion was realised to be dependent on the direction of off-set error. For off-set errors transverse to the beam axis, beam expansion was predominantly in the direction corresponding to the off-set displacement. For instance, when the off-set is along the y-axis, the increment in w_y was dominant. This dominant expansion ratio with regard to positional off-set errors in the x- and y-directions is illustrated in Fig. 4.7(c) and (d), respectively. In contrast, when the positional error of the THz source is along the beam axis, the enlargement of w_x and w_y are comparable. Here the expansion in x direction (shown in Fig. 4.7(b)) is displayed, since the alteration of field distribution in this direction is less affected by the uneven illumination of M1, and provides more information concerning the nature of beam propagation.

The expansion ratio of spot size increases with frequency, as shown in Fig. 4.7(b), (c) and (d). This re-confirms the sensitivity of high frequency components. The pattern of beam expansion also differs significantly with regard to the direction of positional error of the source. When the off-set error is along the beam axis, the expansion is relatively insignificant. For the largest displacement considered ($d_z = \lambda_c$), notable expansion of more than 10% only occurs above 1.7 THz, ending with a maximum expansion ratio of less than 20% at 3.0 THz. The enlargement of beam-waist size for the $d_z = \lambda_c/3$ is merely negligible. In contrast, for positional error in off-axis directions, severe beam expansion occurs. For the same amount of off-axis displacement, the growth rate in beam size is 8-10 times that along the beam axis. The spot spreads into twice in waist at 2.3 THz for $d_x = \lambda_c$ and at 2.5 THz for $d_y = \lambda_c$. Small alterations of w_x is also observed in this case, but rendered unimportant for the interest of this study.

4.4.2 Mode Analysis

A more detailed investigation of the field distribution is carried out with Hermite-Gaussian (HG) mode analysis. The E-field distribution of the mn order HG mode at

the detection plane is expressed as (4.2) [13],

$$E_{mn}(y,z;x) = (2^{m+n-1}\pi m!n!)^{-1/2}\frac{1}{w_x^{1/2}w_y^{1/2}} \times \left\{H_m(\sqrt{2}\frac{x}{w_x})H_n(\sqrt{2}\frac{y}{w_y})\exp\left[-\left(\frac{x^2}{w_x^2}+\frac{y^2}{w_y^2}\right)\right]\right\}, \quad (4.2)$$

where $H_{m(n)}$ is the m(n) order Hermite polymer, $w_{x(y)}$ is the beam half-waist along $x(y)$ axis. The phase-front radius of curvature term is omitted here since the studied area lies in the focal plane of M4. The contribution of the HG_{mn} mode is represented by the coefficient c_{mn} calculated by integrating the field distribution with E_{mn} over the detection plane,

$$c_{mn} = \iint_{s_{dp}} E_y(x,y;z=f)E_{mn}(x,y)\cdot dxdy. \quad (4.3)$$

while $|c_{mn}|^2$ represents the power contributed by HG_{mn} mode. In this work, 25 HG modes were used in total, from HG_{00} to HG_{44}, to decompose the distribution of field. The power coefficient $|c_{mn}|^2$ is normalised and given as percentages to eliminate the factor of field amplitude at different frequencies. Figure 4.8 shows the E-field distribution of the HG modes from HG_{00} to HG_{22}.

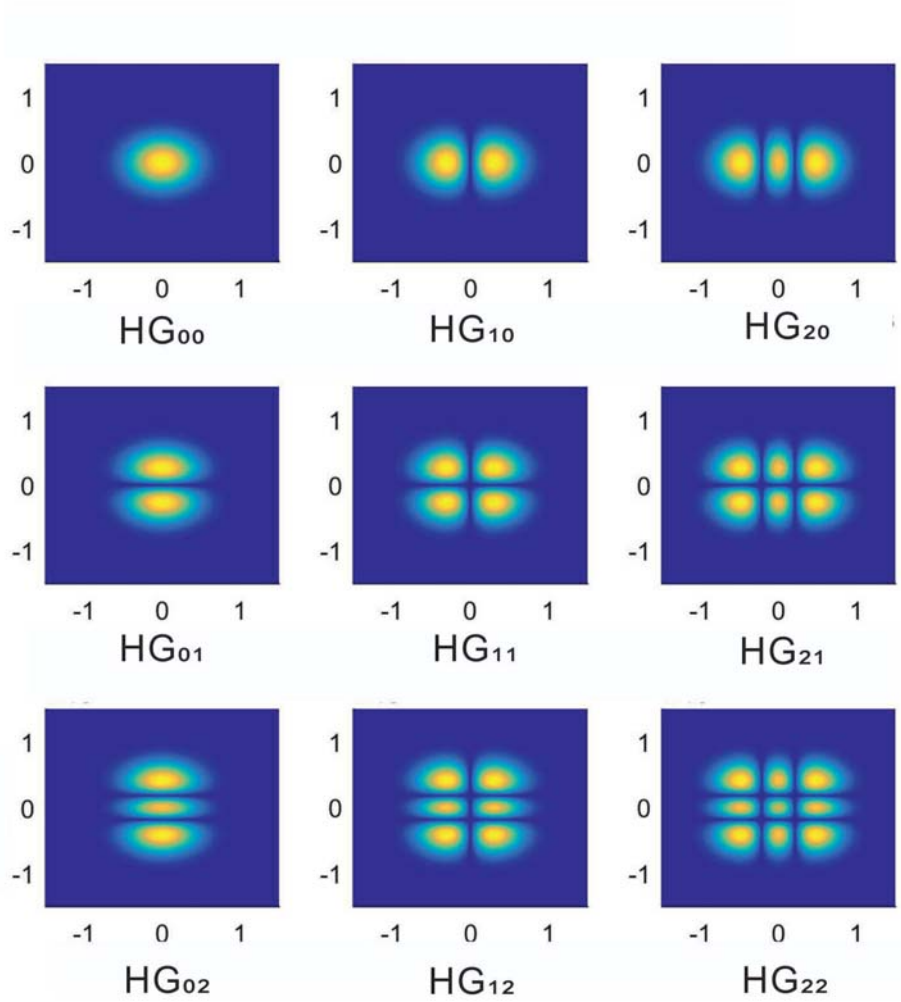

Figure 4.8: E-field distribution of HG modes from HG_{00} to HG_{22}, corresponding to $w_x = 0.74$ mm and $w_y = 0.86$ mm at $f = 2.0$ THz.

The analysis starts form the error-free case. The calculated mode power coefficients at selected frequencies are listed in Table 4-A.

Table 4-A: The weight of dominant modes HG_{00} and HG_{02} for error-free situation at selected frequencies in percentage

Frequency (THz)	0.5	1.0	1.5	2.0
HG_{00}	62.51	71.28	86.64	88.78
HG_{02}	30.72	23.58	10.42	8.02
Sum	93.23	94.86	97.06	96.80

As shown in Table 4-A, when the emitter is ideally positioned, mode content of the beam is dominated by low order HG modes, as expected. Specifically, HG_{00} and HG_{02} together, held more than 90% of beam energy. While in an ideal QO system, HG_{00} should be the dominant mode, the presence of a significant HG_{02} contribution is caused by the edge diffraction of components in the QO path. This can be examined by firstly the HG_{10} dominant field distribution of the cross-polar field E_y that originates purely from diffraction [14, 15], and secondly the reduced coefficients of HG_{02} with increasing frequency due to weakened diffraction,as shown in Table 4-A.

Mode decomposition is now undertaken for situations of off-set error in positioning of the source. The centre of the integration plane in (4.3) is set corresponding to the position offset of the emitter as described in (4.1).

Mode decomposition regarding to field distribution with misalignment at $f_2 =$ 0.5 THz and $f_2 = 1.5$ THz are illustrated in Table 4-B and 4-C, respectively. The off-set distance 0.1 mm, 0.2 mm and 0.3 mm corresponds to $\lambda_1/6$, $\lambda_1/3$, $\lambda_1/2$ for f_1 and $\lambda_2/2$, λ_2, $3\lambda_2/2$ for f_2.

Table 4-B: Power contribution of Gauss-Hermite modes at $f_1 = 0.5$ THz

Location		HG_{0n}	HG_{1n}	HG_{2n}	HG_{3n}	HG_{4n}
In-focus		96.69	Nil	3.82	Nil	0.48
d_x	$\lambda_1/6$	95.08	0.63	3.66	0.08	0.56
	$\lambda_1/3$	93.00	2.42	3.86	0.28	0.45
	$\lambda_1/2$	90.57	4.96	3.38	0.60	0.49
d_y	$\lambda_1/6$	94.94	Nil	4.44	Nil	0.62
	$\lambda_1/3$	94.07	Nil	5.31	Nil	0.62
	$\lambda_1/2$	92.54	0.01	6.66	0.01	0.78

Table 4-C: Power contribution by HG_{mn} mode at $f_2 = 1.5$ THz

Location		HG_{0n}	HG_{1n}	HG_{2n}	HG_{3n}	HG_{4n}
In-focus		97.54	Nil	2.31	Nil	0.15
d_x	$\lambda_2/2$	84.14	12.34	2.75	0.67	0.01
	λ_2	57.23	35.54	3.98	2.29	0.96
	$3\lambda_2/2$	33.60	51.96	6.68	3.79	3.98
d_y	$\lambda_2/2$	90.70	Nil	8.23	Nil	1.06
	λ_2	78.63	Nil	18.49	Nil	2.87
	$3\lambda_2/2$	66.97	Nil	27.77	Nil	5.26

In Tables 4-B and 4-C, the coefficient of the second subscript n is summed up to isolate the effect of edge diffraction (mode HG_{02} for instance). This is also beneficial for a clearer comparison considering the large number of modes used for the decomposition. The results provide a more detailed insight into the influence of the misalignment of the emitter. Overall, as expected, the contribution of fundamental mode reduced as the amount of passion error increased. High frequency components were more sensitive to misalignment of the emitter. For instance, consider the largest error in off-set distance (0.3 mm). At 0.5 THz, the decrement in the contribution of HG_{0n} modes is only 6%

for positional error along the x-axis, and 4% along the y-axis. By comparison, at 1.5 THz, these values respectively increased to 64% and 31%.

While the mode coefficients corresponding to position error are frequency dependent, different patterns of mode coupling between HG modes are further discovered. These coupling patterns are followed at all the studied frequencies. This is realised by first looking into the increment in coefficients of high order modes listed in Table 4-B and 4-C. For off-set error along the y-axis, the power in low order modes was mostly transferred to HG_{2n} and HG_{4n} modes, while the contribution of HG_{1n} and HG_{3n} modes remained merely the same as the error-free situation. This is inherited from the symmetry of the system along the y-axis, which prohibits the existence odd-symmetric modes. For off-set error along the x axis, this symmetry is violated, hence power begins to couple to the odd-symmetric modes. In this case, coupling towards of HG_{2n} and HG_{4n} modes was still observable, but far less significant. The mode that contributes most strongly was identified as HG_{12}, accounting for as much as 4% of field content at 0.5 THz and 48% at 1.5 THz when $d_x = 0.3$ mm. The dominant coupling to HG_{12} mode is not surprised for source off-set along the x axis, as HG_{12} is simultaneously even-symmetric along the x axis, and odd-symmetric along y (as shown in Fig. 4.8). In addition, different patterns regarding to the power coupling to one of the low order modes HG_{02} is also noticed. For off-set error along the y axis, the normalised value of $|c_{02}|^2$ grows monotonically from 31% to 37% for 0.5 THz and from 10% to 49% for 1.5 THz for $d_y = 0.3$ mm. This suggests a more severe edge diffraction in the corresponding direction. In contrast, for the same amount of position error along the x axis, $|c_{02}|^2$ undergoes a decline, by 2 and 7 in percentage for 0.5 THz and 1.5 THz, indicating a weakened diffraction caused by moving away from the major axis of M1s reflecting surface.

In this work, the studies extensively focus on the misalignment in the transverse plane of the beam axis. This is due to the correlation between E-field distribution and the measured THz signal, as demonstrated in the measurements in Sec. 4.3.2. In

principle, mode decomposition regarding to the emitter's position error along the z-axis can also be conducted with similar methods. However, several extra factors will need to be considered. First, as indicated in Fig. 4.3, movement along the optic axis will cause significant time shift of the pulse. Subsequently, the phase term can no longer be omitted for (4.2). An extra phase term of $\exp[ik(x^2/2R_x + y^2/2R_y)]$ should be appended, where k is the angular wave number, R_x and R_y are the phase-front radii of curvature for x and y, respectively. Second, the centre of mode decomposition should be set at the location of maximum field amplitude. As discussed in Sec. 4.4.1, the drift in peak location caused by misalignment in the z-direction is frequency dependent. Therefore, the centre for mode decomposition at different frequencies should be chosen individually.

4.5 Summary

In this chapter, a systematic methodology was presented to investigate the alignment sensitivity of the QO components in THz-TDS systems. Specifically, the influence of misalignment in the broadband THz source was extensively analysed.

An EM simulation model was established to investigate the alteration in E-field due to source misalignment. The influence of source misalignment to the detected THz signal was investigated by combining simulation results with experimental measurements. In general, error position of the THz source leads to attenuation and distortion of the detected THz signal, while the sensitivity increases with the operating frequency. The difference in influences regarding to source position errors along and transverse to the beam axis was observed and discussed. It is realised in this study that, for position off-sets transverse to the beam axis, the alteration in detected signal is determined by not only the field response at the detection focus, but also the field distribution in the near focus area.

Further on, the simulation model was used to map the E-field distribution at the detection plane. The influence of THz source location error was concluded into three aspects: drift of phase centre, expansion in beam waist and change in beam mode. These three aspects were addressed in sequence in this study. The relationship between the drift in phase centre and displacement of the THz source was established. According to the drifted phase centre, the expansion of THz beam width was quantitatively assessed. The expansion of beam waist was observed to severe as frequency increased, confirming the sensitivity of high frequency components. Along the beam axis, the expansion of beam waist was not significant. In contrast, in the transverse plane, for the same amount of displacement, the expansion could be 8 to 10 times larger, while dominant direction of waist expansion was in consistence with the dirction of displacement. In the end, mode analysis was carried out to analyse the detailed alteration in field distribution caused by source location errors. Different patterns of mode coupling regarding to source location error in different directions were discovered and concluded.

References

[1] W. Withayachumnankul and M. Naftaly, "Fundamentals of measurement in terahertz time-domain spectroscopy," *Journal of Infrared, Millimeter, and Terahertz Waves*, vol. 35, no. 8, pp. 610–637, 2014.

[2] W. Withayachumnankul, H. Lin, S. P. Mickan, B. M. Fischer, and D. Abbott, "Analysis of measurement uncertainty in THz-TDS," vol. 6593, Conference Proceedings, pp. 659 326–659 326–18.

[3] G. Paz-Martnez, J. Garduo-Meja, O. V. Kolokoltsev, C. G. Trevio-Palacios, and N. Qureshi, "Focus and alignment tolerance in a photoconductive terahertz source," *Journal of Infrared, Millimeter, and Terahertz Waves*, vol. 36, no. 9, pp. 830–837, 2015.

[4] D. A. Walsh, M. J. Cliffe, R. Pan, E. W. Snedden, D. M. Graham, W. A. Gillespie,

and S. P. Jamison, "Role of misalignment-induced angular chirp in the electro-optic detection of THz waves," *Optics Express*, vol. 22, no. 10, pp. 12 028–12 037, 2014.

[5] M. Kinoshita, H. Iida, and Y. Shimada, "Frequency calibration of terahertz time-domain spectrometer using air-gap etalon," *Terahertz Science and Technology, IEEE Transactions on*, vol. 4, no. 6, pp. 756–759, 2014.

[6] M. Naftaly, R. A. Dudley, J. R. Fletcher, F. Bernard, C. Thomson, and Z. Tian, "Frequency calibration of terahertz time-domain spectrometers," *Journal of the Optical Society of America B*, vol. 26, no. 7, pp. 1357–1362, 2009.

[7] C. M. Collier, M. H. Bergen, T. J. Stirling, M. A. DeWachter, and J. F. Holzman, "Optimization processes for pulsed terahertz systems," *Applied Optics*, vol. 54, no. 3, pp. 535–545, 2015.

[8] R. J. Dietz, N. Vieweg, T. Puppe, A. Zach, B. Globisch, T. Göbel, P. Leisching, and M. Schell, "All fiber-coupled THz-TDS system with kHz measurement rate based on electronically controlled optical sampling," *Optics Letters*, vol. 39, no. 22, pp. 6482–6485, 2014.

[9] N. Krauß, M. Haas, S. Winnerl, M. Helm, and T. Dekorsy, "Terahertz emission based on large-area photoconductive emitters illuminated via beam interference," *Electronics Letters*, vol. 51, no. 17, pp. 1357–1359, 2015.

[10] M. Awad, M. Nagel, H. Kurz, J. Herfort, and K. Ploog, "Characterization of low temperature GaAs antenna array terahertz emitters," *Applied Physics Letters*, vol. 91, no. 18, p. 181124, 2007.

[11] H. Lin, C. Fumeaux, B. M. Fischer, and D. Abbott, "Modelling of sub-wavelength THz sources as Gaussian apertures," *Optics Express*, vol. 18, no. 17, pp. 17 672–17 683, 2010.

[12] A. Bitman, S. Pearl, I. Moshe, and Z. Zalevsky, "Terahertz ultrashort pulse behavior: Near-field and far-field propagation," *Electromagnetics*, vol. 35, no. 3, pp. 167–176, 2015.

[13] D. H. Martin and J. W. Bowen, "Long-wave optics," *IEEE Transactions on Microwave theory and techniques*, vol. 41, no. 10, pp. 1676–1690, 1993.

[14] A. Grtler, C. Winnewisser, H. Helm, and P. Uhd Jepsen, "Terahertz pulse propa-

gation in the near field and the far field," *Journal of the Optical Society of America A*, vol. 17, no. 1, pp. 74–83, 2000.

[15] Y. Wang, Z. Zhao, Z. Chen, L. Zhang, and K. Kang, "Analysis of terahertz pulse propagation through a dielectric edge," vol. 7277, Conference Proceedings, pp. 72 770R–72 770R–8.

Chapter 5

Terahertz Photoconductive Antennas Arrays

In this chapter, the prospect of performance enhancement of THz PCAs with array configurations is examined. The phenomenon of optical saturation is briefly discussed to demonstrate the significance of the array configuration. A systematic study of THz PCA arrays is then carried out by combining array factor analysis with experimental measurements.

5.1 Introduction

In previous chapters, a linear relationship between optical intensity and photoconductive substrates response is assumed. However, in practice, this is valid only for low optical intensity excitation. As the intensity of optical excitation increases above a certain threshold, saturation in photoconductive process occurs. This leads to a reduced optical-electrical conversion efficiency.

Multiple physical processes can contribute to this saturated photocondcutive response.

In ref. [1, 2], the screening of the bias electric field under strong optical excitation is discussed extensively. The screening field is jointly contributed to by the counter effect of THz radiation and the space charge created during the photoconductive process. Their influences are compared in the work of Kim *et al.*, to identify the dominant phenomenon [3]. Meanwhile, for semiconductors with trapped-states, such as LT-GaAs, defect saturation also occurs at high intensity optical excitation [4]. This retards carrier recombination. Fig. 5.1 shows the effect of optical saturation with regard to the radiated THz field intensity and carrier lifetime.

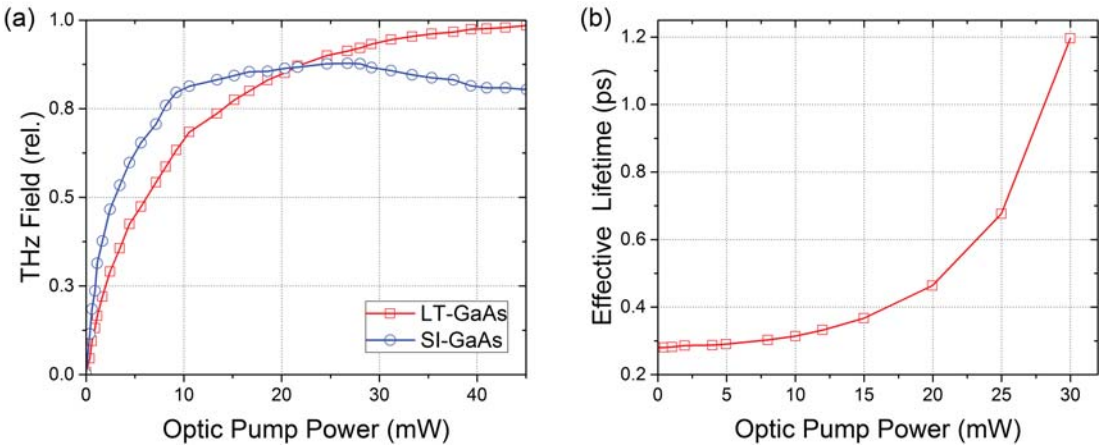

Figure 5.1: Optical saturation in THz PCAs. (a) Saturation by the radiated THz field of LT-GaAs and SI-GaAs based PCAs [5], linear realtionship between THz field and optical pump power breakdown at 10 mW; (b) Alteration of carrier lifetime due to trapped-state saturation [4], carrier lifetime increases with optical pump power.

Typical values of the optical fluence threshold for saturation in GaAs substrates ranges from $15 \sim 200$ $\mu J/cm^2$ [1, 3, 6]. This threshold can be easily exceeded with common ultrafast laser devices. To avoid the saturation area, the optical power needs to be dispersed in space. As each individual illuminated area is capable of radiating THz wave, the overall configuration can be considered as PCA arrays.

5.2 Array Factors for THz PCAs

The concept of antenna array is broadly applied for RF frequency antennas. Antenna arrays are formed by arranging antenna elements according to a certain spatial distribution. The major benefit of an array configuration is to offer adaptability to the radiation character, such as increasing the gain of the radiation pattern and controlling the direction of the main lobe. Generally, for a selected antenna, its radiation characteristics, such as gain and radiation pattern, are fixed. By forming an antenna array, the overall radiation charactersitics can be altered by manipulating the array layout and feeding of elements. Array antennas with high gain and directivity can be realised using this concept [7].

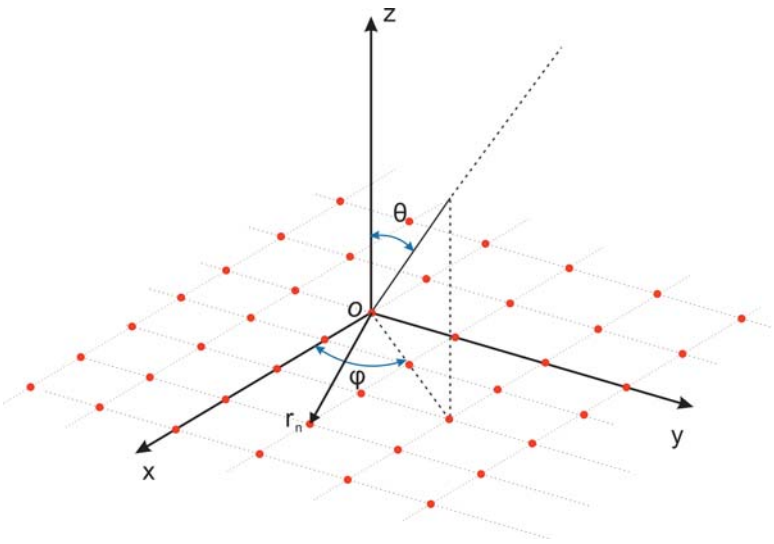

Figure 5.2: Schematic of a planar antenna array, red dots represents the antenna elements. The polar angle θ and azimuth angle ϕ are as indicated

Figure 5.2 illustrates the schematic of a planar antenna array. The influence of the array configuration on the radiation characteristics is represented by the array factors (AF). It connects the radiation pattern an element with that of the antenna array. By

taking the centre of the the array as origin, the AF can be calculated as [8],

$$AF(\theta) = \sum_{n=1}^{N} \dot{I}_n \exp(ikr_n \sin\theta), \tag{5.1}$$

where θ is the polar angle; N is the number of elements; $\dot{I}_n$ is the complex feed signal of the n^{th} element; k is the wave number; and r_n represents the location of the n^{th} element as in Fig. 5.2. The factor of azimuthal angle ϕ is omitted due to rotation symmetry.

Here, the concept of AF is transferred to evaluated the influence of the array configuration on the performance of THz PCAs. For an antenna array, its AF is determined by four factors: number of elements, spatial distribution of elements, amplitudes of element feeds and the relative phase of each feed. Generally, for conventional antennas, these four parameters can be adjusted independently to manipulate the AF. In contrast, for THz PCAs, due to the nature of optical beam feeding, these four array parameters are mutually coupled. The spatial distribution of elements is determined by the power dispersion mechanism of the optical beam upon excitation. PCA arrays are classed accordingly into continuous discrete arrays, and are studied separately in the following sections.

5.3 Continuous THz PCA Arrays

Continuous THz PCA arrays refer to the scenario in which THz PCAs are excited by optical beams of finite beam waists w_o. The distribution of the elements is therefore continuous within the illuminated area. A schematic of a continuous THz PCA array is shown in Fig. 5.3.

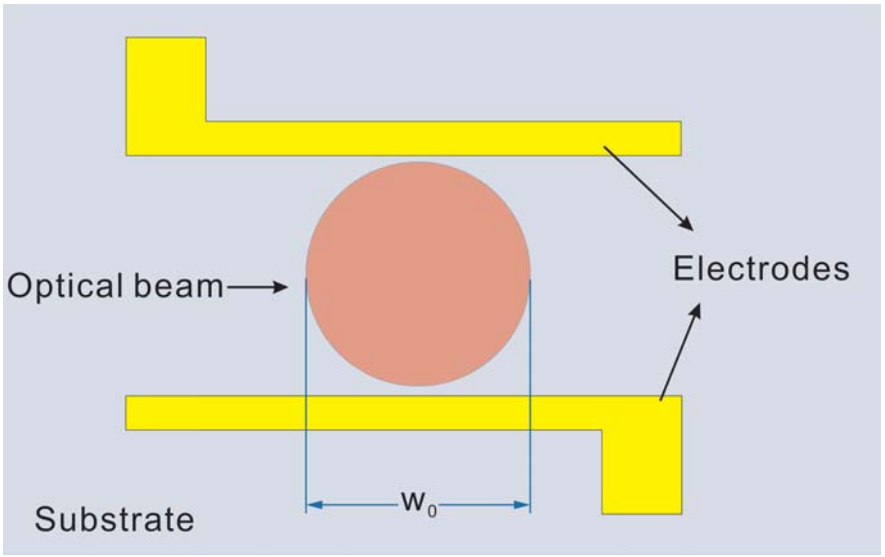

Figure 5.3: Schematic a continuous THz PCA array with interdigitated electrodes. The THz PCA is excited by an optical beam of beam waist w_o between the electrodes.

In this section, the AF for this scenario is established. Based on AF analysis, the performance dependence of THz PCAs to optical beam sized is discussed and examined.

5.3.1 Array Factors of Continuous Arrays

For continuous arrays, the summation over elements in (5.1 becomes integration over the radiating area, while the amplitude of feeding is represented by the concentration of carriers in the radiating area $n(\mathbf{r})$. The normal direction of the PCA substrate aligns with the propagation direction of the laser, so that no phase difference is realised between elements. Assuming that the distribution of carriers is azimuthally symmetric, for frequency f, the AF of the continuous array then becomes,

$$AF(f:\theta,\phi) = \int n(\mathbf{r}) \exp[-i\mathbf{k}(f)\cdot\mathbf{r}]dxdy. \tag{5.2}$$

Further assuming that the optical beam conforms to a fundamental Gaussian distri-

bution in space, and a linear relationship holds between the carrier concentration and the optical beam intensity. The spatial distribution of the carrier is,

$$n(\mathbf{r}) = n_0 \exp[-(r/w_o)^2], \tag{5.3}$$

where w_o is the beam waist of the optical beam on the PCA.

Substituting (5.3) into (5.2), the AF can be expressed as,

$$AF(f:\theta) = n_0 \pi w_o^2 \exp\left\{-\frac{[k(f) w_o \sin\theta]^2}{4}\right\}. \tag{5.4}$$

The first term in (5.4), $n_0 \pi w_o^2$ can be considered as the total number of carriers generated in the photoconductive process. For the same laser device and photoconductive substrate, this factor can be considered as a constant. The angular distribution of the AF for continuous array is therefore determined by the exponential factor in (5.4). Array configuration affects the radiation pattern of the antenna through its square value [9],

$$AF_p(f:\theta) = |AF(f:\theta)|^2. \tag{5.5}$$

As indicated in (5.5), the angular dependence of AF_p is determined by the value of the product of the wave constant and the optical beam size $k(f)w_o$.

1. When $k(f)w_o < \sqrt{2}$, the influence of the variation in angular factor $\sin\theta$ is weak: Maximum variation in AF_p is less than $1/e$. For $k(f)w_o \ll \sqrt{2}$, AF_p becomes quasi-omnidirectional.

2. When $k(f)w_o > \sqrt{2}$, the influence of $\sin\theta$ over AF_p becomes significant: AF_p is therefore strongly angular dependent.

For a specific optical beam size w_o, the threshold frequency f_c for directional and

non-directional radiation corresponds to $k(f)w_o = \sqrt{2}$,

$$f_c = \frac{c}{\sqrt{2}\pi w_o}. \tag{5.6}$$

5.3.2 Radiation Dependence of THz PCAs on Optical Beam Size

Considering the broadband nature of THz radiation from THz PCAs, the influence of a specific optical beam size w_o on AF_p clearly varies over the THz spectrum. Figure 5.4 illustrates the evolution of AF_p corresponding to frequency and optical beam size.

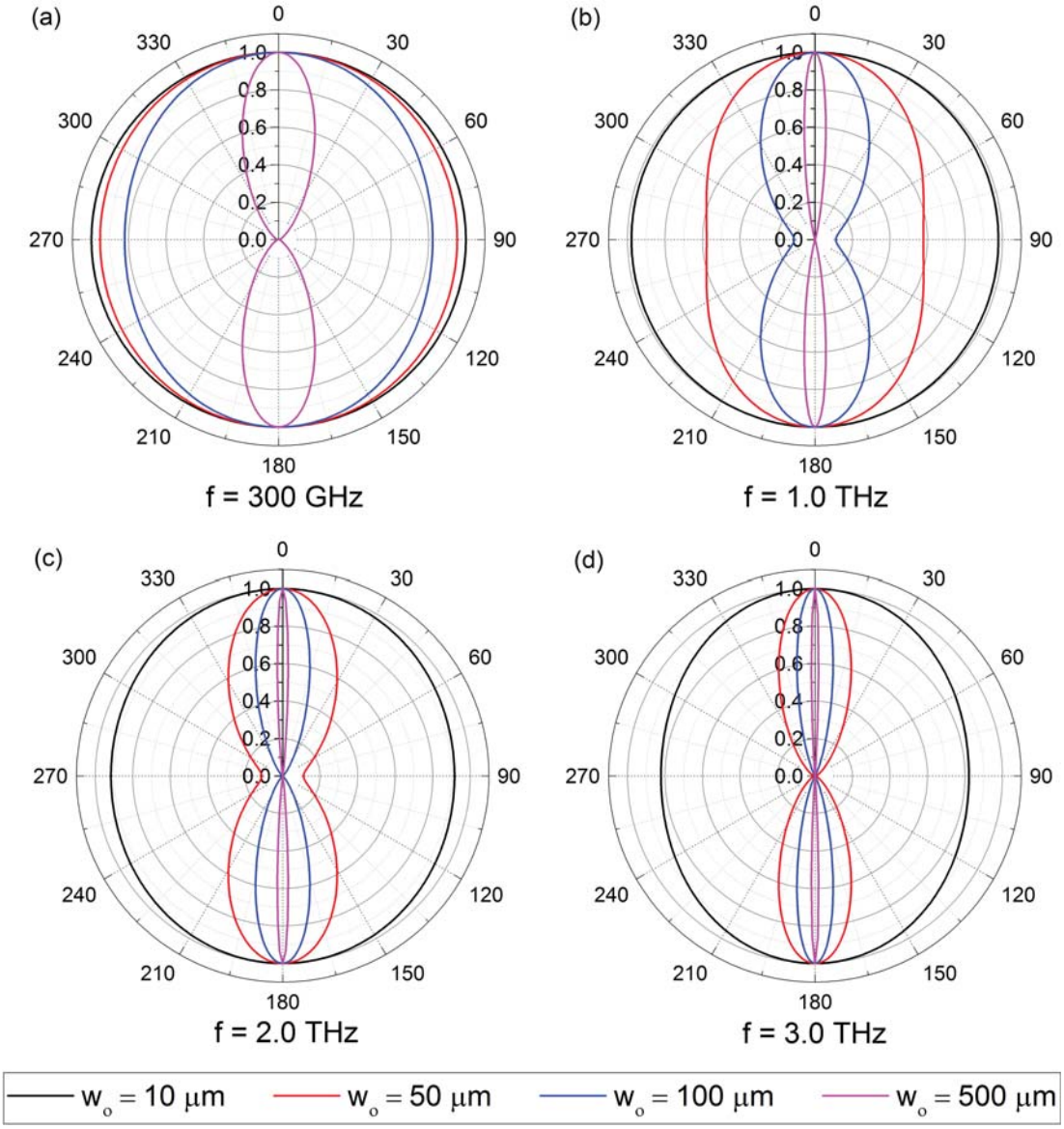

Figure 5.4: Evolution of AF_p at typical frequencies to source dimensions. (a) $f = 300$ GHz; (b) $f = 1.0$ THz; (c) $f = 2.0$ THz; (d) $f = 3.0$ THz

Typical frequencies between 300 GHz and 3.0 THz were selected to cover the majority of the THz spectrum radiated from THz PCAs. As shown in Fig. 5.4, the evolution of AF_p with w_o is highly dispersive. For all frequencies, AF_p become more directional as w_o increases, while the rate of alteration varies dramatically. When gated with an extremely small optical beam ($w_o = 10\mu$m), all frequencies radiates quasi-

omnidirectionally. At the low spectral limit of the THz radiation at 300 GHz, this omnidirectional radiation pattern is maintained to at least $w_o = 100$ μm; while for high frequency components above 2.0 THz, the radiation pattern is already highly directional at $w_o = 50$ μm. Nevertheless, with a large optical beam waist of 500 μm in the end, the radiation patterns of all frequencies become directional.

The influence of optical beam size on the operation of THz PCAs was further examined by experiment. A THz PCA with the gap dimension of $d_g = 500$ μm was used for this measurement. Two scenarios of laser illumination were demonstrated in the measurement. Case-in scenario one, optical excitation of the THz PCA was realised with a focusing lens in the pump-beam path. The diameter of the optical beam on the semiconductor substrate was approximately $w_o = 50$ μm. In scenario two, the lens was removed. The THz PCA was directly excited by the output optical beam from the laser. The measurement results are shown in Fig. 5.5.

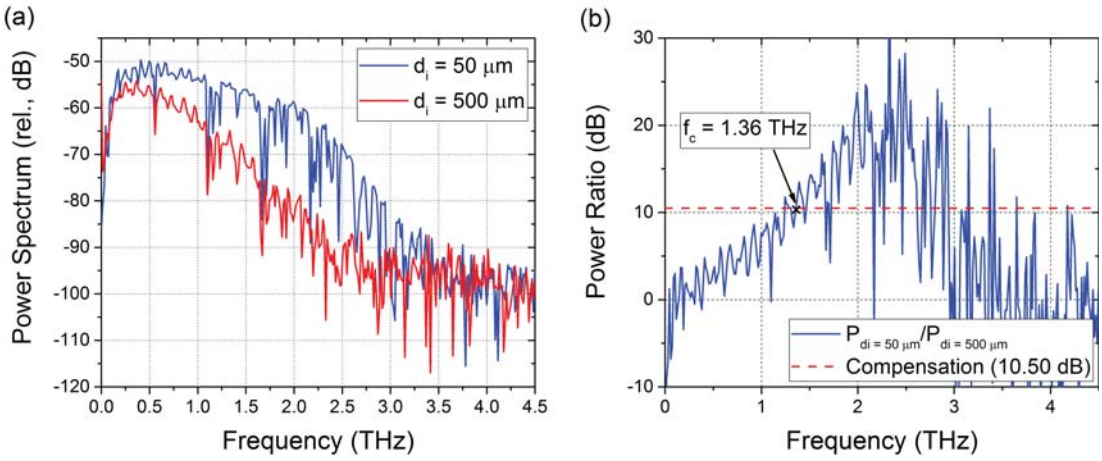

Figure 5.5: Measured power spectra of THz pulses radiated from a PCA excited with optical beam of different waists

A difference in power spectra is observed in Fig. 5.5(a). Overall, the PSD is weighted to the high frequency region for the THz radiation for $w_o = 50$ μm. Referring to Fig. 5.4, this is due to the uneven contribution of this beams size to AF_p. As frequency increases, the directivity of the radiation is enhanced, and more power is collected. The frequency dependent AF_p therefore introduces a high-pass filter action to the radiation.

In contrast, for the excitation dimension of 500 µm, the AF_p is directional over the spectrum of the THz radiation. The frequency filtering effect is therefore insignificant.

For a fair comparison in power ratio, two compensation factors for the large optical excitation dimension of 500 µm are taken into account. The first is the influence of the change in relative dimensions of gap and optical beam size. This is discussed with the equivalent circuit model in Sec. 3.3. By taking the measured excitation parameter of $k_\rho = 3.66$ for $d_i = 50$ µm into the calculation, a power ratio of $\eta_r = 1.16$ is realised between the two excitation scenarios. The second is the alteration in received optical energy upon excitation. The half-waist of the unfocused optical beam of the ultrafast laser is approximately $w_0 = 1.2$ mm (from factory data). Assuming that the gap of the THz PCA lies in the centre of the Gaussian distribution of the optical beam, the absorbed energy is then 32.2% of the total energy of the laser. These two compensation factors together yield an compensated power ratio of 10.50 dB.

The power ratio between the two excitation conditions and the compensation value intersects at approximately $f_c = 1.36$ THz. This frequency marks the turning point of the influence of optical beam dimension on AF_p for the excitation condition of $w_o = 50$ µm. For the frequency domain below f_c, AF_p from the 50 µm excitation is more omnidirectional, while AF_p from 500 µm excitation is directional. Radiation from 500 µm excitation is thereby more efficient. For the frequency domain above f_c, AF_p from 50 µm also become highly directional. Subsequently, the radiation efficiency for the two optical beam waists are comparable. In the measurement, for the 50 µm beam waist, the radiated power above f_c was higher than the compensation level. This is due to the optical saturation effect caused by high optical intensity at small beam waist. The reversed screening bias field leads to a faster change in photocurrent, and a larger power distribution at high frequency [1]. Overall, the measured f_c matches to the calculated value of 1.35 THz from last section. This indicates the validity of the continuous AF analysis.

The theoretical calculation and measurement results demonstrate the superior performance on directivity enhancement with large optical beam excitation. However, challenges exist in the implementation of this concept. According to (5.6), a beam waist of at least 255 μm is required to achieve directional radiation at 300 GHz. Meanwhile, as the beam waist expands, the intensity of optical excitation decreases. Referring to the discussion in Sec. 3.3, asymmetric excitation is more efficient with regard to the coupling out of the generated THz radiation. To satisfy the condition $d_g \gg w_o$, a gap dimension larger than 2.55 mm is required. To maintain an average electric field of approximately 1×10^4 V/cm in the gap area, the bias voltage is required to be in the range of several kV. The requirement of high bias voltage increases the complexity of the bias circuit, and the SNR of the THz-TDS system can be compromised. Another practical issue is the increased location off-set of the edge element w_o expands. This leads to a reduced contribution to the detected THz field, as discussed in Chapter 4.

5.4 Discrete THz PCA Arrays

Discrete THz PCA arrays are introduced to maintain the enhancement in directivity realised by continuous arrays whilst avoiding the requirement for high bias voltages. In practice, this is generally realised by creating interdigitated electrode structures in the optically illuminated area. The layout of the interdigitated electrode structure is demonstrated in Fig. 5.6.

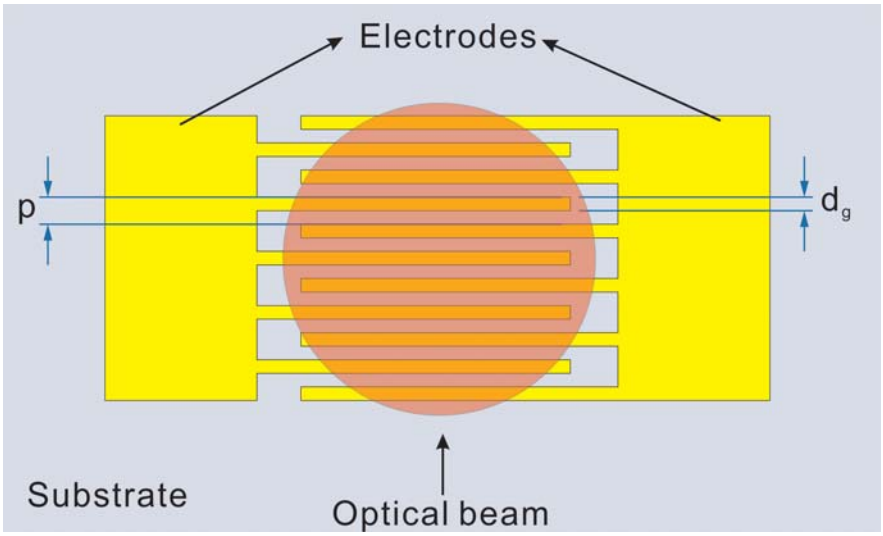

Figure 5.6: Schematic a THz PCA array with interdigitated electrodes. Interdigitation of period p, gap width d_g is created in the optically illuminated area.

It is noticed that the interdigitated electrode structure creates a bias electric field of opposite polarities between the neighbouring gap areas. This is equivalent to a phase difference of π in the local THz radiation, and will lead to cancellation of the E-field in the far-field. In practice, controlled excitation of elements is required to avoid such destructive interference. This can be achieved by using a micro-lens array to guide the optical beam onto the desired elements [10, 11], shielding or etching off the photoconductive substrate in the reverse biased area [12, 13], or introducing an optical phase mask to control the phase of the THz pulses [14].

5.4.1 Array Factors of Discrete Arrays

For discrete THz PCA arrays, the number of elements is related to optical beam size w_o and the period p of the interdigitation via,

$$N = \lfloor (w_o/p) \rfloor, \tag{5.7}$$

where the symbol $\lfloor\ \rfloor$ means flooring to the nearest integral.

To avoid destructive interference from neighbouring elements, every other elements is optically excited. The distance between elements is therefore twice the period $d_e = 2p$, while the number of radiating elements N_r is,

$$N_r = \begin{cases} N/2 & \text{When N is even} \\ (N+1)/2 & \text{When N is odd} \end{cases} \tag{5.8}$$

The feeding amplitude of the n^{th} element corresponds to the optical energy absorbed by its respective gap area. Here in this study, only the optical power distributed directly above the gap area d_g is considered. For a Gaussian distribution of the optical beam, the feeding intensity is,

$$n_n = n_0 \iint_{gap,n} \exp(-\frac{x^2+y^2}{w_o^2})dxdy. \tag{5.9}$$

In practice, depending on the specific selective excitation scheme, the integration area in (5.9) needs to be adjusted according to the feeding. However, the trend of feeding intensity between elements should be similar for the same optical pump beam. Given the purpose of this sub-study is to explore the significance of the array configuration, the difference caused by the selective excitation schemes is not considered here.

The optically excited areas in the gaps can be further regarded as continuous arrays. For excitation with micro-lens arrays, the dimensions of optical beams in the gap areas are generally very small (≤ 10 μm [11]). Referring to the discussion in Sec. 5.3, the AF can be considered omnidirectional. In contrast, for excitation without beam forming devices, the normalised continuous AF of the n^{th} element can be expressed as,

$$AF_n(\theta) = n_0\sqrt{\pi(w_o^2 - n^2p^2)}d_g \exp\left[-\frac{(kd_g \sin\theta)^2}{4}\right]. \tag{5.10}$$

Overall, the AF for discrete PCA arrays are calculated as,

$$\begin{aligned} AF(f:\theta) &= \sum_{n=1}^{N_r} n_n \exp[ink(f)d\sin\theta] \cdot AF_n(\theta) \\ AF_p(f:\theta) &= |AF(f:\theta)|^2 . \end{aligned} \tag{5.11}$$

5.4.2 Analysis and Optimisation of Interdigitated THz PCAs

Based on the discussion above, here the dependence of the discrete AF on the interdigitation structure were examined. Similar to the discussion for continuous case, the influence of optical beam waist for a fixed interdigitation was firstly examined . The evolution of AF_p for an interdigitation structure of $p = 20$ µm and $d_g = 10$ µm is shown in Fig. 5.7. The energy of the optical beam for different w is set uniform, while the angular dependence of AF to d_g is not taken into account here as all gaps possess the same gap dimension.

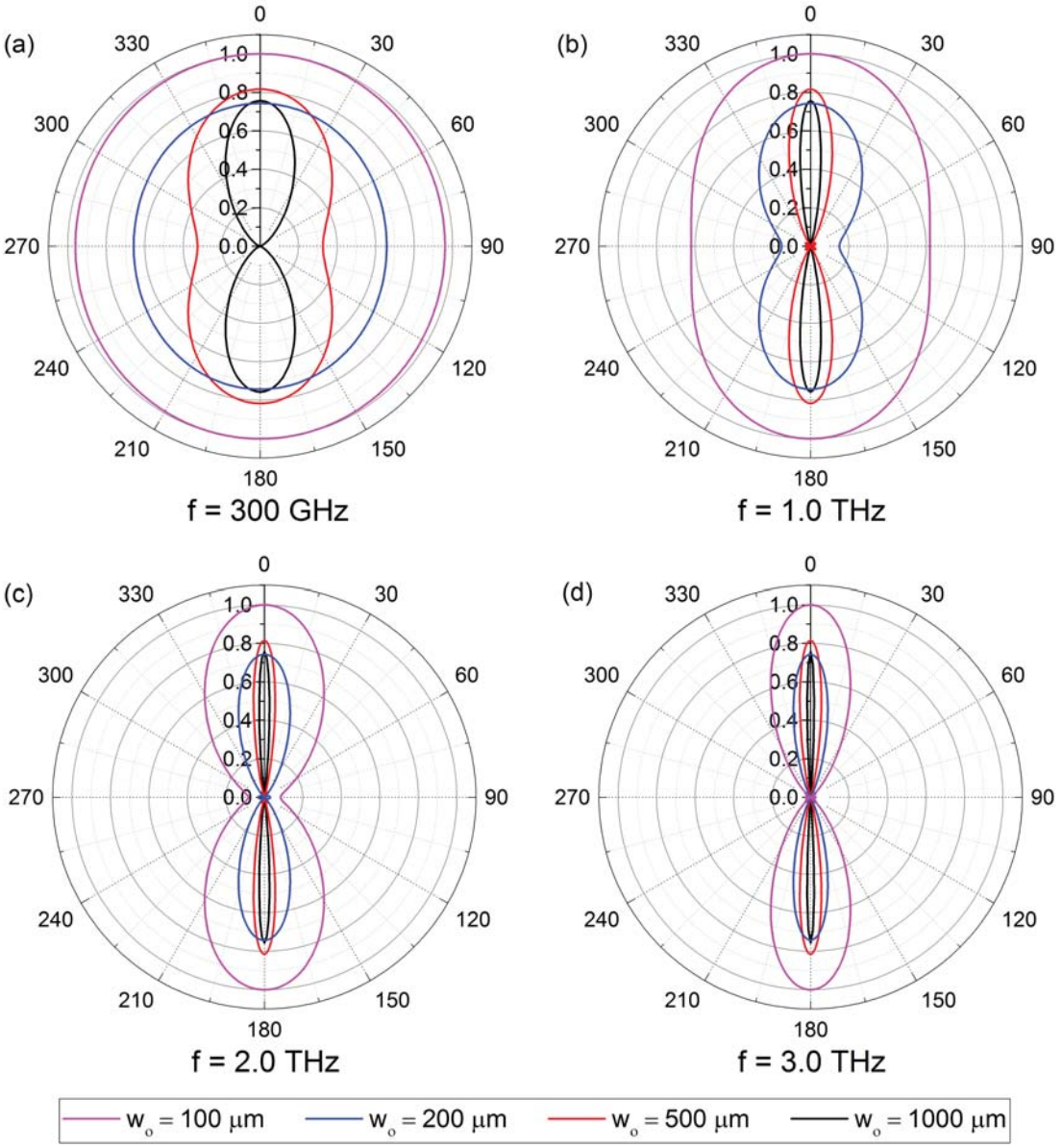

Figure 5.7: Evolution of AF_p for $p = 20$ μm and $d_g = 10$ μm interdigitation to optical beam waist at typical frequencies. (a) $f = 300$ GHz; (b) $f = 1.0$ THz; (c) $f = 2.0$ THz; (d) $f = 3.0$ THz

Similar to the results of the continuous array, the AFs of the discrete array becomes more directional as w_o increases. From the aspect of the discrete array, the enhanced directivity is caused by the increased number of transmitting elements as per (5.7). Meanwhile, in comparison to the continuous array, a larger beam waist (roughly twice)

is required to achieve the same level of directional radiation. In addition to the angular dependence, the change in maximum gain is also observed as the optical beam expands. This is due to the reduced amount of optical energy collected by expanding the optical beam waist. However, the alteration in maximum gain for $w_o \geq 200$ μm is small as the reduction in collected optical power is compensated by the increased number of transmitting elements. From Fig 5.7, $w_o \geq 500$ μm is recommended for directional radiation from interdigitated THz PCAs.

Next, the influence of the period p of the interdigitation was addressed. w_o was set at 500 μm to create a reasonably large transmitting area. To solely represent the dependence of p, the feeding amplitude was normalised, and the angular dependence of AF to d_g was again ignored. The results are shown in Fig. 5.8.

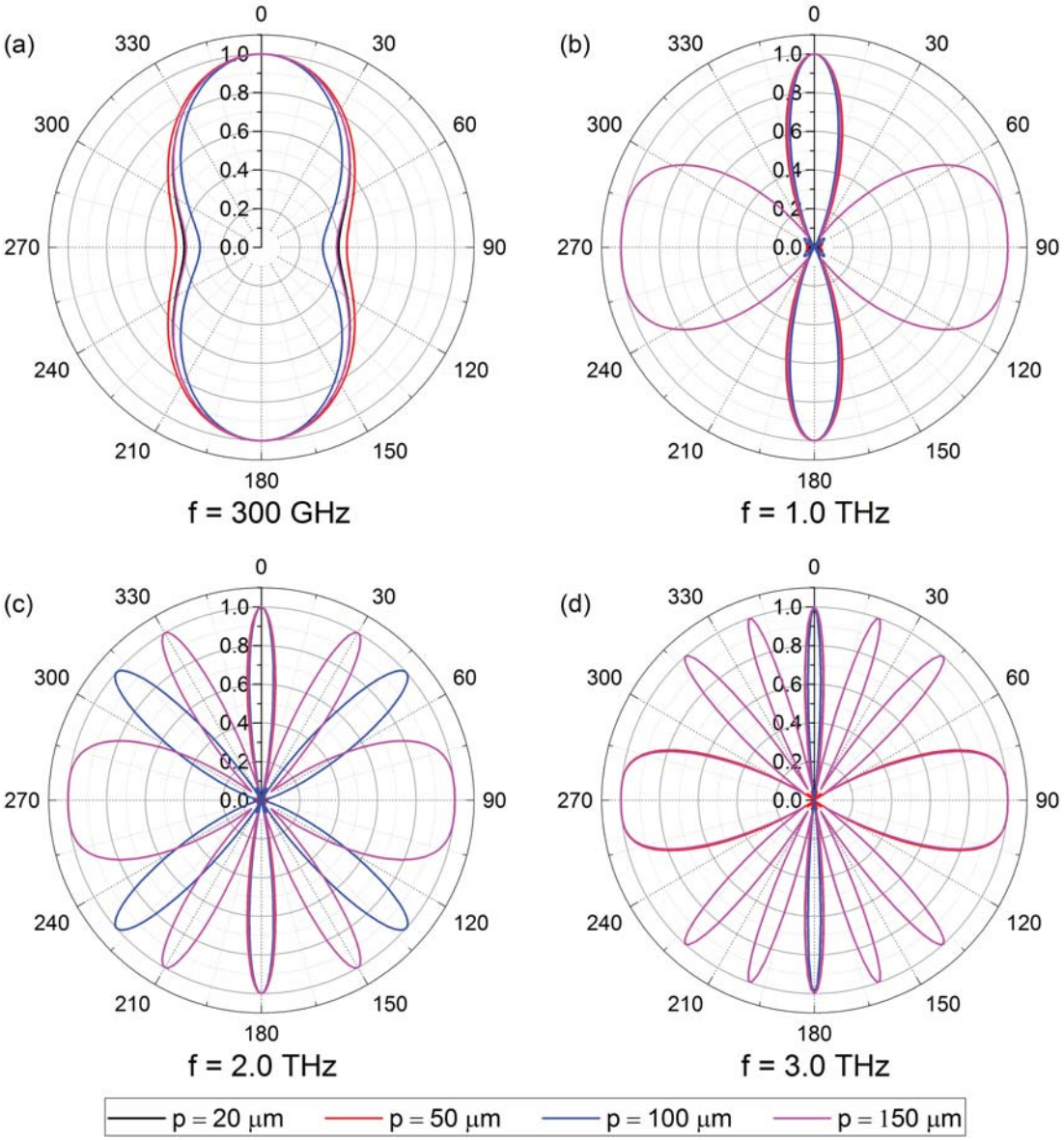

Figure 5.8: Evolution of AF_p at typical frequencies to period of interdigitation. (a) f = 300 GHz; (b) f = 1.0 THz; (c) f = 2.0 THz; (d) f = 3.0 THz

The results demonstrate the difference in nature between continuous and discrete arrays. The distance between elements plays a dominant role in the angular distribution of AF. As frequency increase, the influence of p becomes significant. The enlarged distance between elements creates side lobes in the AF. In array theory, the number

and location of side lobes is determined by the operation frequency, number of elements and distance between elements [7]. In interdigitated THz PCAs, the last two factors are linked through (5.7) and (5.8). For a wavelength of $\lambda(f)$, the threshold period p_c for the appearance of the first side lobe is approximately as,

$$p_c = \frac{w_o \lambda(f)}{2[w_o + \lambda(f)]}, \tag{5.12}$$

and in reverse, the threshold frequency for the appearance of the first side lobe is,

$$f_{cs} = c \cdot \frac{w_o - 2p}{2w_o p}. \tag{5.13}$$

Finally, the effect of gap dimension within the period of interdigitation was analysed. From (5.9), one of the direct benefits from increasing d_g is the increased collection optical energy. Here, this factor was normalised to specifically examine the influence of d_g upon the angular profile of AF. Within the same period of $p = 100$ μm, the alteration of the AF due to d_g is shown in Fig. 5.9.

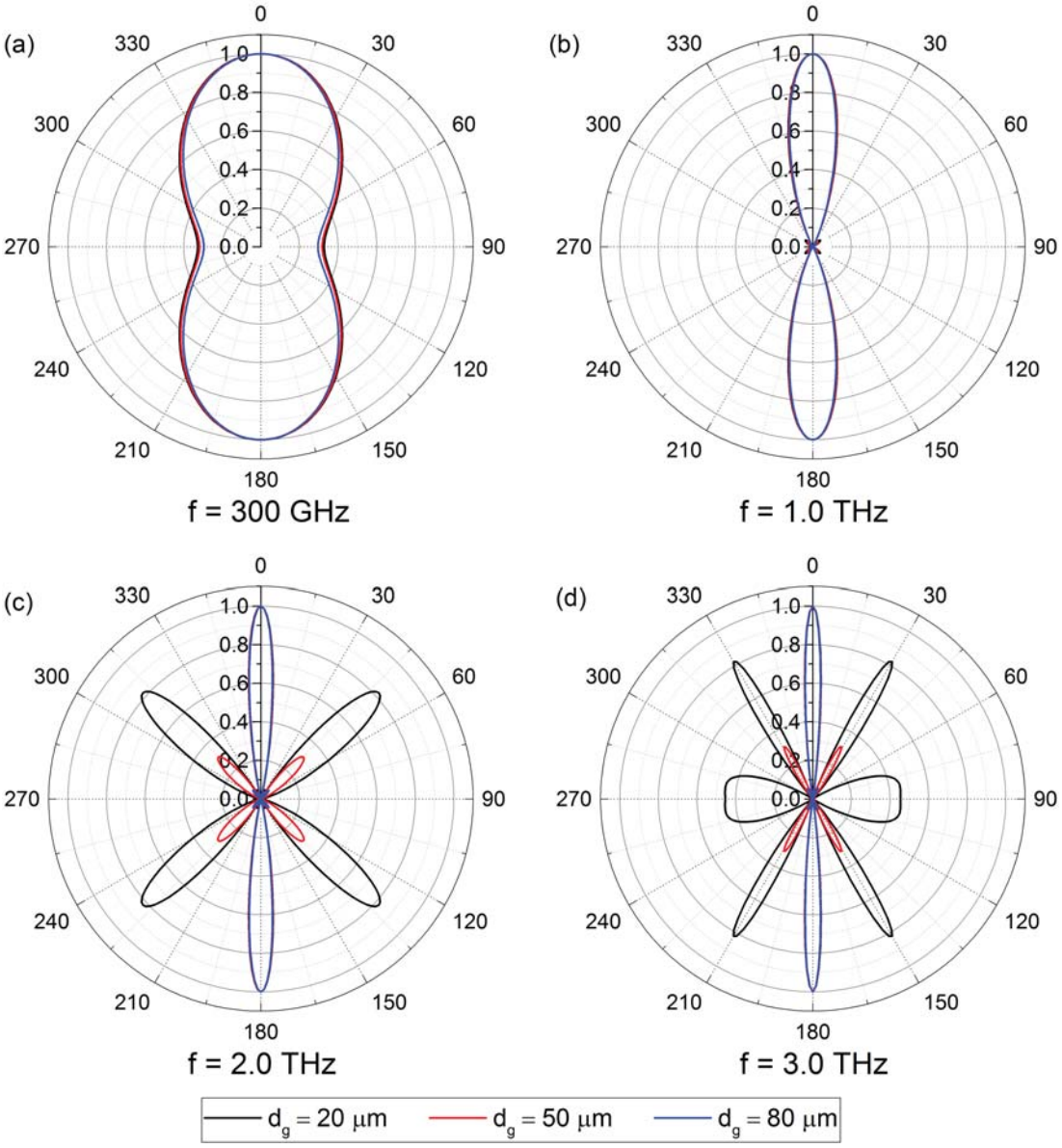

Figure 5.9: Evolution of AF_p to gap dimension at typical frequencies. (a) f = 300 GHz; (b) f = 1.0 THz; (c) f = 2.0 THz; (d) f = 3.0 THz

The influence of d_g is revealed by comparing the blue curves in Fig. 5.8 to Fig. 5.9. For the AF without side lobes at 300 GHz and 1 THz, the effect of d_g is negligible. In contrast, for AF with side lobes, the side lobes can be significantly suppressed by increasing d_g. The side lobes were reduced to less than 30% when d_g = 50 μm at 2.0 THz and 3.0 THz, and was eliminated for d_g = 80 μm. The suppression of side

lobes originates from the directional radiation of the continuous array within the gap area. To conclude, a large gap area within the period is beneficial not only for collecting optical energy but also for side lobe suppression at high frequency.

5.4.3 Fabrication and Measurement of Interdigitated THz PCAs

Here, the performance dependence of interdigitated THz PCAs in connection to their geometric configurations is further demonstrated in experiment. To avoid the complicated alignment process with micro-lenses and to take advantages of the directional radiation from the gap dimension, the measruement here implemented the controlled excitation scheme with shadow masks similar to that in ref. [13]. In total, eight sets of interdigitated THz PCAs with different geometric configurations were designed for fabrication and measurement. Their geometric parameters were listed in Table 5-A.

Table 5-A: Geometric parameters of fabricated interdigitated PCAs

	A1	A2	B1	B2	B3	C1	C2	C3
p (μm)	200	100	200	100	50	85	40	20
d_g (μm)	50	50	25	25	25	10	10	10

5.4.3.1 Fabrication

For this work, a four-layer structure was proposed and fabricated to realise selective illumination of PCA elements. A schematic of the configuration is shown in Fig. 5.10.

The bottom two layers are the photoconductive substrate and the electrode structure. They form the radiating part of the THz PCA. The top layer is the shadow mask corresponding to the specific interdigitation of the electrodes. It is integrated into the PCA avoid the complication of alignment of the shadow mask in measurement. Between the mask layer and electrodes lies a buffer layer. This layer is optically transparent to the pump beam for efficient excitation, while electrically insulated to

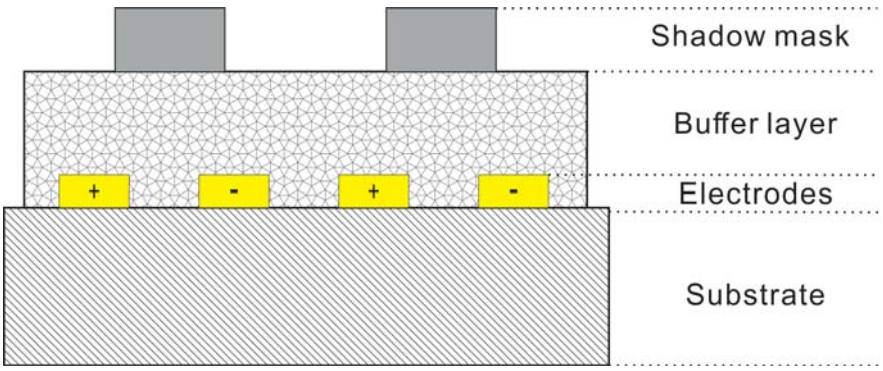

Figure 5.10: Schematic side view of the four layer interdigitated THz PCA, from bottom to top is the photoconductive substrate, interdigitated electrodes, buffer layer and shadow mask. Polarity of the bias on the electrodes are as displayed, and the shadow mask is aligned to the gap between the electrodes.

prevent short circuiting between the electrodes.

The interdigitated PCAs were fabricated using multi-layer aligned photo-lithography on SI-GaAs substrates. The electrode-layer and mask-layer were formed by aluminium with thickness of 70 nm. This provided a good conduction for the electrodes, together with an attenuation of over 99% of the optical power at 800 nm wavelength [15]. A lithography - lift-off process was implemented to achieve high quality formation of the electrode layer, while a simpler lithography - metal-etching process was used to fabricate the mask layer as the quality requirement for the mask layer is comparatively less. The buffer-layer was formed by cured SU8-2005 photoresist with a thickness of approximately 5 μm. This layer is highly transparent to 800 nm light with a transmittance greater than 95% [16]. In the photo-lithography process, the three layers were accurately aligned via alignment marks. Details of the fabrication recipe are provided in Appendix C. Fig. 5.11 provides micrographs images of several selected interdigitated THz PCAs from fabrication with measurements of the geometric parameters.

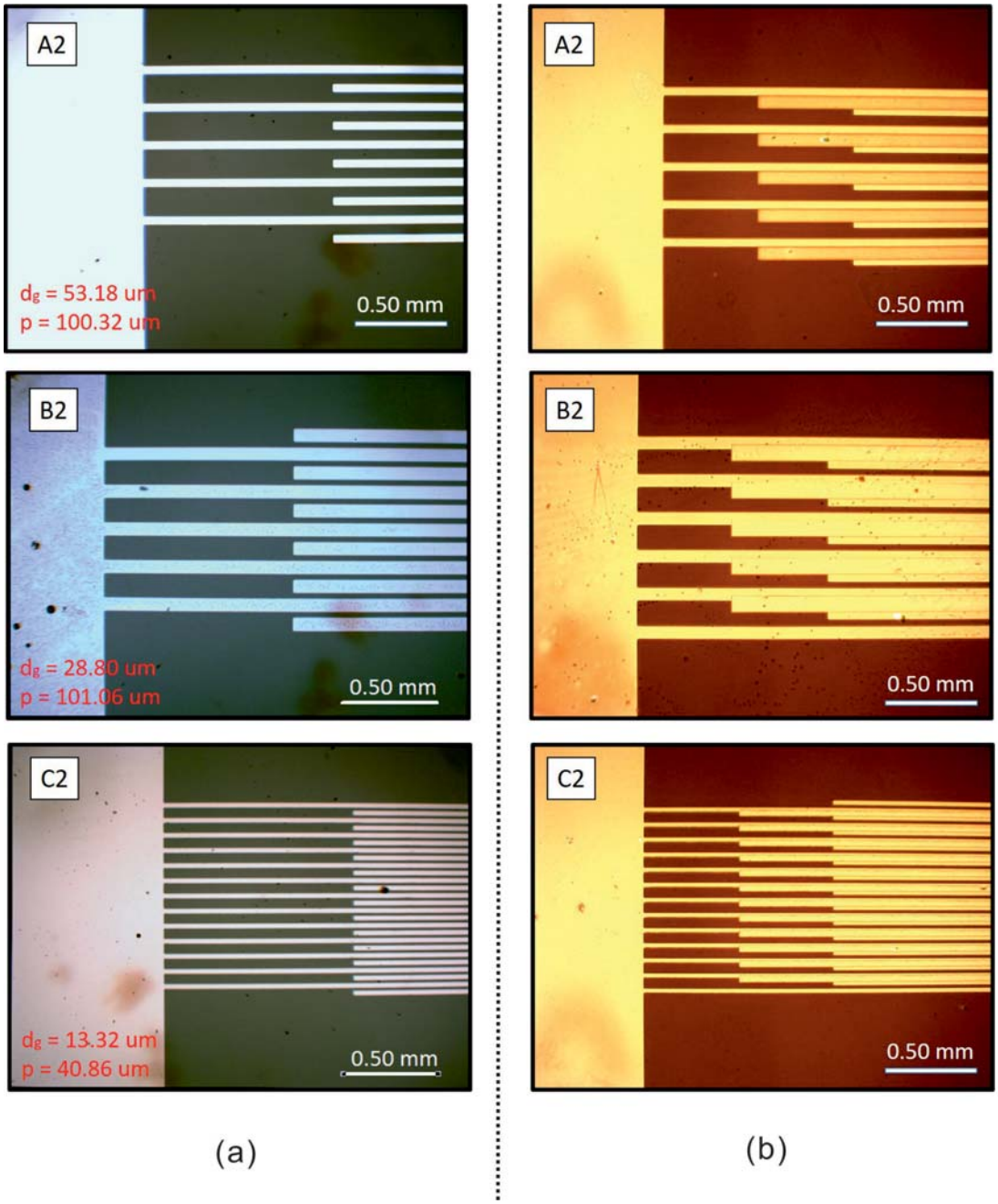

Figure 5.11: Micrographs of selected fabricated THz PCAs with interdigitated electrodes. (a) Without shadow mask layer; (b) after deposition of the shadow mask layer.

In the approach used here, the fabricated gap dimensions were generally $3 \sim 4$ μm

larger than designed, while the period of the interdigitation was accurate to errors within 1 μm. The error in gap dimension is due to the limitation in the thickness of the photo-resist and the parallelism of exposure UV light. Overall, the fabricated structures were near identical to the design.

5.4.3.2 Measurement Results

The performance of the interdigitated THz PCAs was experimentally evaluated using the THz-TDS bench used in previous measurements.

The influence of the excitation optical beam size was firstly demonstrated experimentally. Two laser illumination scenarios were engineered using similar methods to the continuous array measurements of Sec. 5.3. Two optical beam widths of approximately 200 μm and 1000 μm were set by controlling the distance between the lens and PCAs. Figure 5.12 shows the measurement results in the time and frequency domains for patterns B1, B2 and B3.

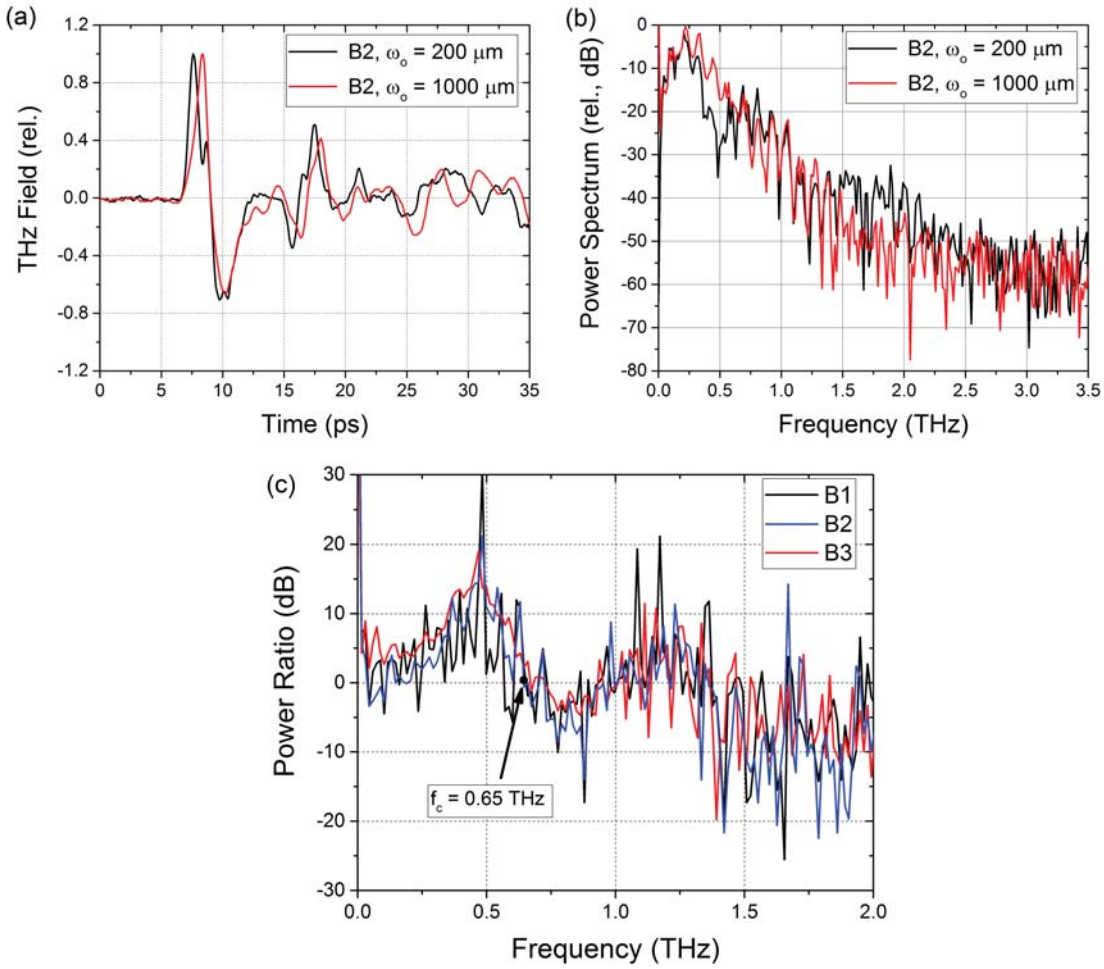

Figure 5.12: Influence of optical beam dimension for interdigitated PCAs. Plots (a) and (b) illustrates the time-domain and frequency domain response of B2 under the two illumination conditions; (c) shows the spectral power ratio between w_o = 1000 μm and w_o = 200 μm for B1, B2 and B3.

In the time domain signal shown in Fig. 5.12(a), the THz pulse generated from the large w_o has a larger pulse width. This corresponds to a larger distribution of power in the low frequency regime. The spectral power ratios shown in Fig. 5.12(c) demonstrate an enhancement in power of to 15 dB in the spectrum below f_c = 0.65 THz. The measured f_c is approximately twice the f_c calculated from (5.6) for the continuous array

at $w_o = 200$ μm. Similar trends in power ratio and f_c are realised in the measurement of interdigitated PCAs with other geometric parameters. This suggests that the alteration solely originates from the change in optical beam waist. Similar to the continuous array, this enhancement in radiated power originates from the improved directivity for low frequency components as w_o increases. In the spectrum above f_c, the AF from the two w_o values are both directional, and the enhancement in the power spectrum vanishes.

The influence of p was then examined in sequence. The gap dimension d_g was kept the same in each set of measurements. Here, the measurement results from C1, C2 and C3 with the excitation optical beam of $w_o = 200$ μm are selected for demonstration. The gap dimensions of these PCAs were small so that the effect of side lobe suppression from gap dimension is weak. According to (5.13), this selection of parameters yield $f_{cs1} = 0.26$ THz, $f_{cs2} = 2.25$ THz and $f_{cs3} = 6.0$ THz. These values spread across the spectrum of THz-TDS measurement, and will create a dramatic change in the corresponding AF, and subsequently the measured THz field. The measured results are shown in Fig. 5.13.

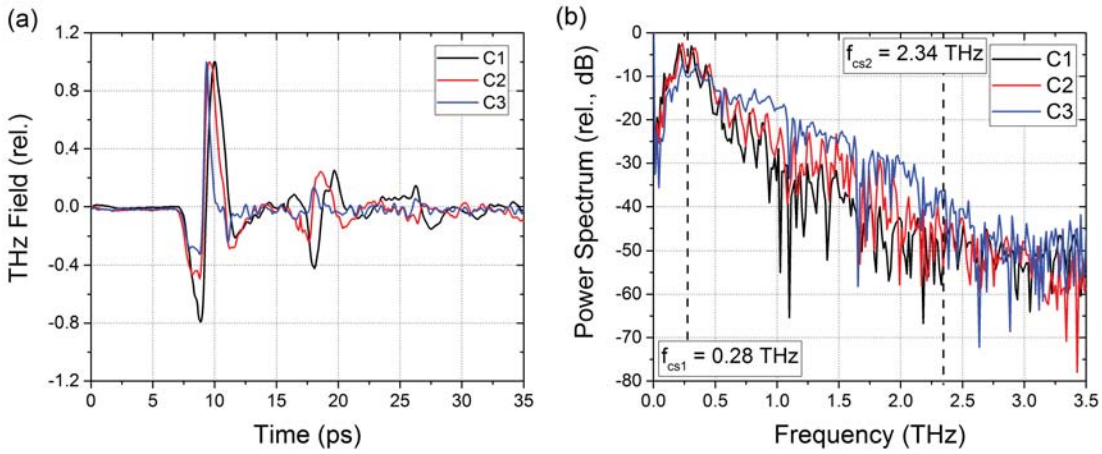

Figure 5.13: Measured THz signal from C1, C2 and C3 with $w_o = 200$ μm in (a) time domain; (b) power spectrum

In the time-domain, the pulse widths of the THz signals are compressed as p reduces. This indicates a larger contribution in the high frequency range. This trend is more

significant in the frequency domain as shown in Fig. 5.13(b). Owing to the selected parameters, side lobes start to appear at a very low frequency for C1. This leads to a reduced measured power comparing to C2 and C3 above $f_{cs1} = 0.28$ THz. The measured power spectrum from C2 stays above that from C1 until $f_{cs2} = 2.34$ THz. These are reasonably close to the predicted value. In contrast, the enhancement in the power spectrum can be observed over the whole frequency range of the THz radiation, as f_{cs3} is above the higher cut-off frequency of the generated THz wave. This measurement validates the proposed theorem.

Lastly, the influence of d_g was examined. This was realised by comparing the measured THz signal between the two pairs of interdigitated electrodes with the same p: A1 to B1 ($p = 200$ μm), and A2 to B2 ($p = 100$ μm). The optical beam waist of $w_o = 1000$ μm was used in this measurement. The measurement results are shown in Fig. 5.14.

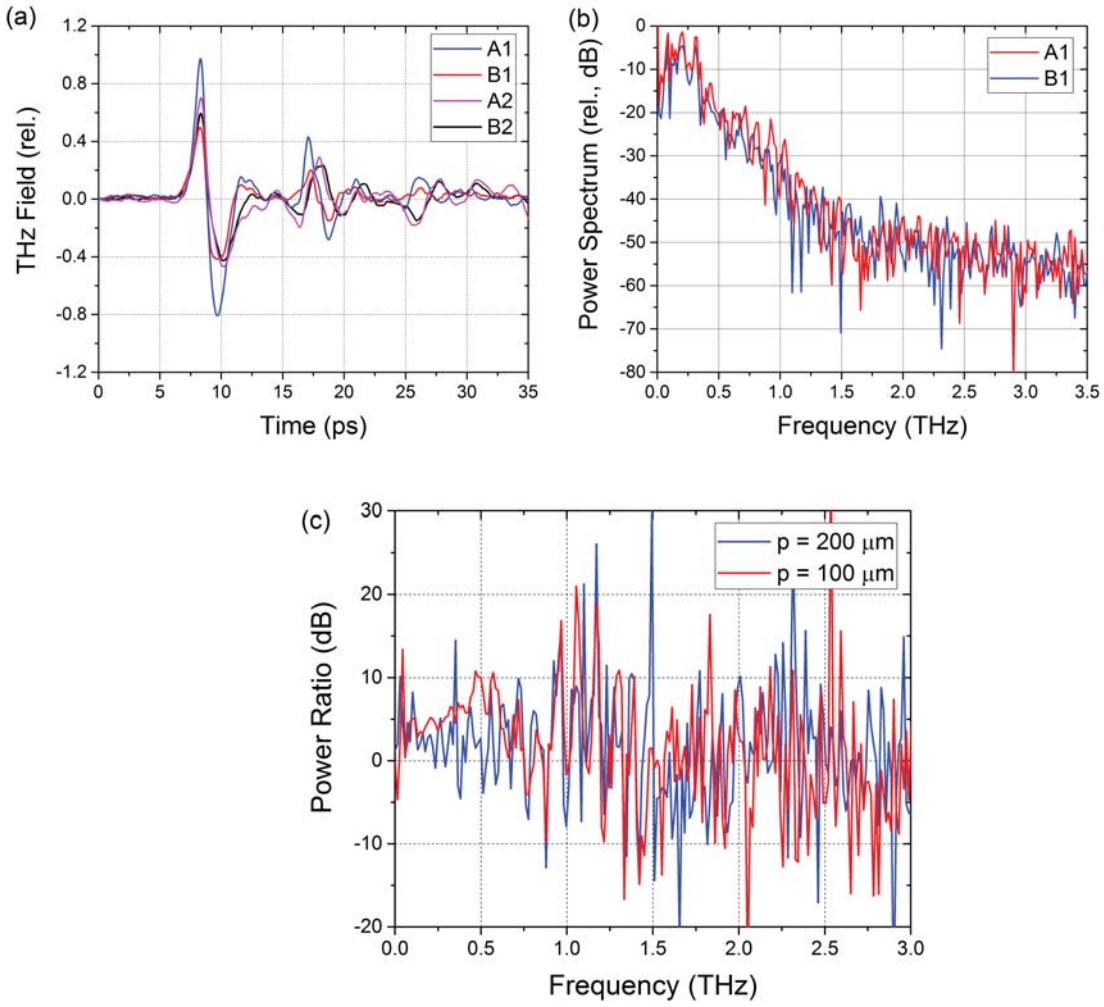

Figure 5.14: Comparison of measured THz signal from interdigitated PCAs with same p but different d_g. (a) Time domain response; (b) frequency domain response of A1 and B1; (c) spectral power ratio between A1 and B1 (blue), A2 and B2 (red)

A first point to notice in Fig. 5.14(a) is that the increased signal amplitude correlated to the increased d_g. As discussed, this originates from the increased absorption of optical energy. Average enhancements of 4.5 dB and 3.1 dB are realised for p = 100 μm and p = 200 μm respectively, as shown in Fig. 5.14(c). On the other hand, power enhancement correlated to side lobe suppression is not observed. No significant dispersive behaviour in power ratio is observed. This is most likely due to the relatively

small values of d_g used in the measurements. This limits the side lobe suppression to the high frequency band.

5.5 Summary

In this chapter, a systematic performance evaluation of THz PCA arrays was presented based on array factor analysis. Depending on the optical illumination scheme, THz PCA arrays are further categorised into continuous arrays and discrete arrays. Coupling conditions of array parameters for these two scenarios are developed.

For continuous arrays, the influence of optical beam size to the angular distribution of AF was specifically examined in theory. It is shown that a large optical beam size is beneficial for directional radiation. The critical condition for directional radiation regarding to optical beam waist and operation frequency was provided and validated by experiment. The measured critical frequency for directional AF at $w_o = 200$ μm is 1.37 THz. This is within 1% error to the predicted value, confirming the validity of the proposed theorem.

In the study of discrete arrays, the influence of the relevant geometric parameters on AF were examined independently. The excitation beam waist plays a similar role as in continuous arrays, while its significance is reduced. The requirement of beam waist for directional radiation is approximately twice of that for continuous arrays. The influence of the interdigitation period was realised to be highly dispersive. Critical conditions for the appearance of the first side lobe were introduced. The influence of the gap dimension was examined in combination with the continuous array theorem. A large gap dimension is recommended not only for the absorption of optical power but also the suppression of side lobes. Interdigitated THz PCAs of different geometric parameters were fabricated and experimentally assessed to validate the proposed theorem. Specifically, the measured critical frequencies for the appearance of first side

lobes for $p = 85$ μm and 40 μm at $w_o = 200$ μm are $f_{cs1} = 0.28$ THz and $f_{cs2} = 2.34$ THz. The differences between these two frequencies and the predicted values from the proposed theorem are less than 4%. In total, reasonably good agreement between experiment results and theory is achieved.

References

[1] G. Rodriguez and A. Taylor, "Screening of the bias field in terahertz generation from photoconductors," *Optics Letters*, vol. 21, no. 14, pp. 1046–1048, 1996.

[2] J. T. Darrow, X.-C. Zhang, D. H. Auston, and J. D. Morse, "Saturation properties of large-aperture photoconducting antennas," *IEEE Journal of Quantum Electronics*, vol. 28, no. 6, pp. 1607–1616, 1992.

[3] D. S. Kim and D. Citrin, "Coulomb and radiation screening in photoconductive terahertz sources," *Applied Physics Letters*, vol. 88, no. 16, p. 161117, 2006.

[4] S. Rihani, R. Faulks, H. Beere, H. Page, I. Gregory, M. Evans, D. A. Ritchie, and M. Pepper, "Effect of defect saturation on terahertz emission and detection properties of low temperature GaAs photoconductive switches," *Applied Physics Letters*, vol. 95, no. 5, p. 051106, 2009.

[5] M. Tani, S. Matsuura, K. Sakai, and S.-i. Nakashima, "Emission characteristics of photoconductive antennas based on low-temperature-grown GaAs and semi-insulating GaAs," *Applied Optics*, vol. 36, no. 30, pp. 7853–7859, 1997.

[6] J. H. Kim, A. Polley, and S. E. Ralph, "Efficient photoconductive terahertz source using line excitation," *Optics Letters*, vol. 30, no. 18, pp. 2490–2492, 2005.

[7] R. J. Mailloux, *Phased array antenna handbook*. Artech House Boston, 2005, vol. 2.

[8] C. A. Balanis, *Antenna theory: analysis and design*. John Wiley & Sons, 2016.

[9] G. H. Döhler, L. E. Garcia-Muñoz, S. Preu, S. Malzer, S. Bauerschmidt, J. Montero-de Paz, E. Ugarte-Muñoz, A. Rivera-Lavado, V. Gonzalez-Posadas, and D. Segovia-Vargas, "From arrays of THz antennas to large-area emitters," *IEEE Transactions*

on Terahertz Science and Technology, vol. 3, no. 5, pp. 532–544, 2013.

[10] G. Matthäus, S. Nolte, R. Hohmuth, M. Voitsch, W. Richter, B. Pradarutti, S. Riehemann, G. Notni, and A. Tünnermann, "Large-area microlens emitters for powerful thz emission," *Applied Physics B*, vol. 96, no. 2-3, pp. 233–235, 2009.

[11] A. Singh, N. Awari, S. Prabhu, and A. Vengurlekar, "THz from photoconductive antennas using circular and cylindrical Microlens arrays," in *Infrared, Millimeter and Terahertz Waves (IRMMW-THz), 2011 36th International Conference on*. IEEE, 2011, pp. 1–2.

[12] M. Awad, M. Nagel, H. Kurz, J. Herfort, and K. Ploog, "Characterization of low temperature gaas antenna array terahertz emitters," *Applied Physics Letters*, vol. 91, no. 18, p. 181124, 2007.

[13] X. Ropagnol, F. Blanchard, T. Ozaki, and M. Reid, "Intense terahertz generation at low frequencies using an interdigitated ZnSe large aperture photoconductive antenna," *Applied Physics Letters*, vol. 103, no. 16, p. 161108, 2013.

[14] X. Ropagnol, R. Morandotti, T. Ozaki, and M. Reid, "THz pulse shaping and improved optical-to-THz conversion efficiency using a binary phase mask," *Optics Letters*, vol. 36, no. 14, pp. 2662–2664, 2011.

[15] K. M. McPeak, S. V. Jayanti, S. J. P. Kress, S. Meyer, S. Iotti, A. Rossinelli, and D. J. Norris, "Plasmonic films can easily be better: Rules and recipes," *ACS Photonics*, vol. 2, no. 3, pp. 326–333, 2015, pMID: 25950012.

[16] O. P. Parida and N. Bhat, "Characterization of optical properties of su-8 and fabrication of optical components," in *Proceedings of the International Conference on Optics and Photonics, Chandigarh, India*, vol. 30, 2009.

Chapter 6

Plasmonic Electrode Assisted Photoconductive Process

In this chapter, the novel approach of efficiency enhancement in THz-PCAs with plasmonic assisted electrodes is reviewed and examined. The fundamentals of the excitation of surface plasmons are briefly reviewed. Plasmonic structures for the specific application of THz PCAs are assessed and studied. Optimisation principles with regard to properties of the substrates are proposed and examined.

6.1 Introduction

As reviewed in Sec. 2.1, THz radiation from PCAs relies on the ultrafast transient response of the photoconductor to the excitation optics. Trade-off is made between the field amplitude and its ultrafast transient characteristics.

In recent studies, THz PCAs with nano-structures were proposed to overcome this limitation [1]. Typical approaches include incorporating nano-rod [2] and nano-island [3] structures into the optical illuminated area, integrating plasmonic structures

on the electrode structures [4, 5] or the photoconductive substrate [6]. These approaches take advantage of the resonance between the nano-structure and the excitation optics to harvest the carrier generation. The approach of interating plasmonic structures to the PCA electrodes is considered most promising. With this configuration, over fifty times of power enhancement in THz radiation comparing to conventional PCAs was realised in the work of Berry *et al* [4]. A schematic of the plasmonic incorporated THz PCA is demonstrated in Fig. 6.1.

With distinction to conventional THz PCAs, in plasmonic assisted photoconductive process, the optical beam is first coupled to the periodic plasmonic structure before interacting with the photoconductive substrate. A localised surface plasmon resonance (LSPR) is created at the metal-semiconductor interface, leading to an enhanced optical field. This results in a dense carrier concentration in the near electrode area, and subsequently a strong THz radiation.

In the following sections, the principles of operation of plasmonic assisted THz PCAs are reviewed and discussed. Optimisation corresponding to the carrier properties of the photoconductive substrate is proposed. The discussion ends with fabrication and testing of THz PCAs that incorporate plasmonic electrodes.

6.2 Extraordinary Optical Transmission for THz PCAs

Surface plasmons (SPs) refer to oscillation of electrons at the surface of conductors. Essentially, they are quantized EM waves constrained to the surface of the conductors [7, 8]. In optics, one of the most tantalizing aspects caused by SPs is the possibility to transmit and concentrate optical beams through sub-wavelength structures (commonly at a metal-dielectric interface), *i.e.*, extraordinary optical transmission (EOT) [9]. Commonly, EOT results in a highly confined E-field at the interface [10]. This is of great interest concerning enhancement of the surface interaction between optics and

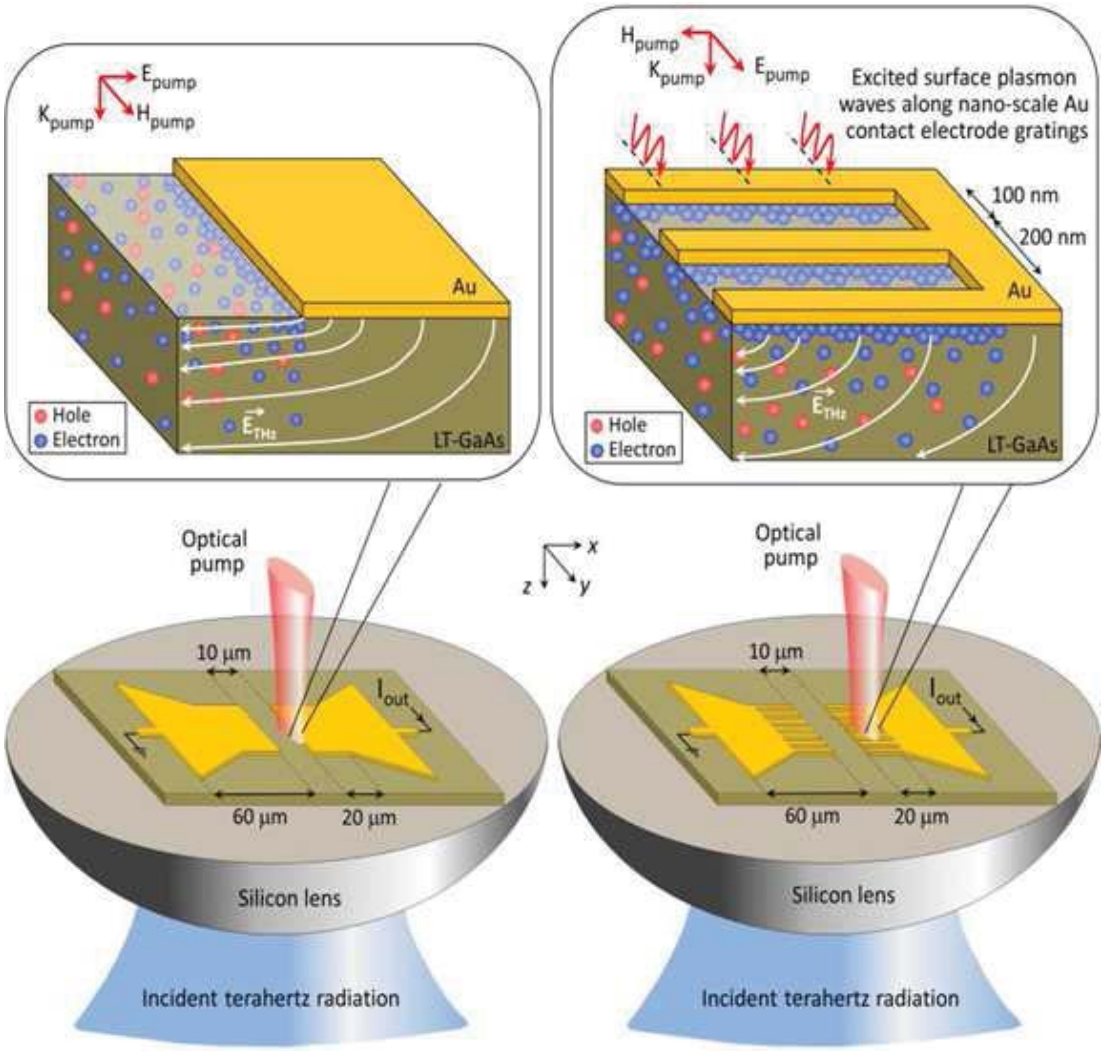

Figure 6.1: Schematics of conventional THz PCAs and THz PCAs with plasmonic electrodes [4]. For THz PCAs with plasmnoic electrodes, optical beam is first coupled to the surface plasmons before arriving on the photocoductive substrate.

materials, such as the development of high sensitivity sensors [11], enhanced Raman spectroscopy [12], etc.

SPs can only exist in TM modes due to the constraints in boundary conditions at the metal-dielectric interface. Consider the interface of a metal with permittivity ϵ_m and a dielectric with permittivity ϵ_d, the dispersion relation of surface waves can be

described as [13],

$$k_{sp}(\omega) = k_0 \sqrt{\frac{\epsilon_d(\omega)\epsilon_m(\omega)}{\epsilon_d(\omega) + \epsilon_m(\omega)}} \tag{6.1}$$

where k_{sp} is the SP angular wave-vector; ω is the angular frequency. For a Drude metal, its permittivity at ω is,

$$\epsilon_m(\omega) = 1 - \frac{\omega_p^2}{\omega^2} \tag{6.2}$$

where ω_p is the plasma frequency of the metal.

Substitute (6.2) into (6.1) to examine the dispersive nature of k_{sp}. At the low frequency domain ($\omega \ll \omega_p$), the interaction between SPs and the EM wave is weak, $k_{sp} \approx k_0\sqrt{\epsilon_d}$. SPs propagate long the interface, and decay exponentially in the vertical direction (also know as Sommerfeld-Zenneck waves). As the frequency increases and approaches ω_p the interaction between SPs and the EM wave becomes significant. Gold and silver are the most commonly used metals since their plasma frequencies are in the visible spectrum. Meanwhile, a momentum mismatch between SPs and the EM wave is realised, according to (6.1). This mismatch needs to be bridged in order to generate SPs.

In EOT, the momentum mismatch is generally compensated by the sub-wavelength periodic corrugation in the metal surface. Specifically, for plasmonic electrodes assisted THz PCAs, this periodic structure is formed by metallic slits. A schematic of the periodic metallic slits is shown in Fig. 6.2.

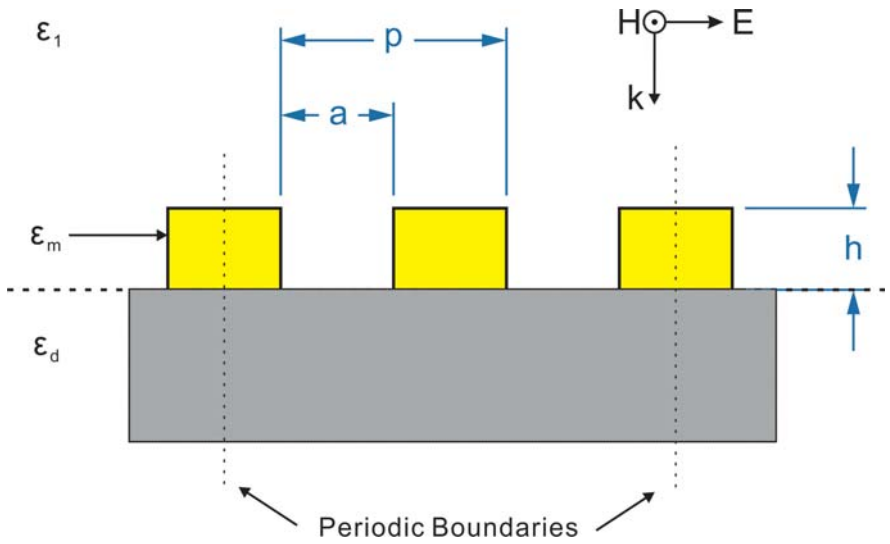

Figure 6.2: Schematic of the plasmonic coupled sub-wavelength structure. A TEM wave incidents on the sub-wavelength metal structure with period of p, spacing of a and thickness of h. TM modes are then excited within the nano-slits.

The geometric dependence of transmittance from the periodicity in the metal has been extensively studied by Yang *et al.* and Hsieh *et al.* [14, 15]. Here, in this work, the effects of the plasmonic structure were revealed in EM simulation concerning the specific application of THz PCAs. The model for simulation was built in the CAD package COMSOL. The model captured the layout as shown in Fig. 6.2. Periodic boundary conditions were assigned to the side edge of the model as indicated. The frequency of optical illumination was set to be between 750 nm and 850 nm, corresponding to the absorption wavelength of GaAs substrates. Gold was used as the electrode material. The complex dielectric constants of GaAs and gold in the corresponding spectrum were assigned for the model. Parametric studies were undertaken for p between 100 nm and 400 nm and a/p from 0.1 to 0.9. Figure 6.3 maps the distribution of optical absorption density at 800 nm optical excitation corresponding to several selected geometries.

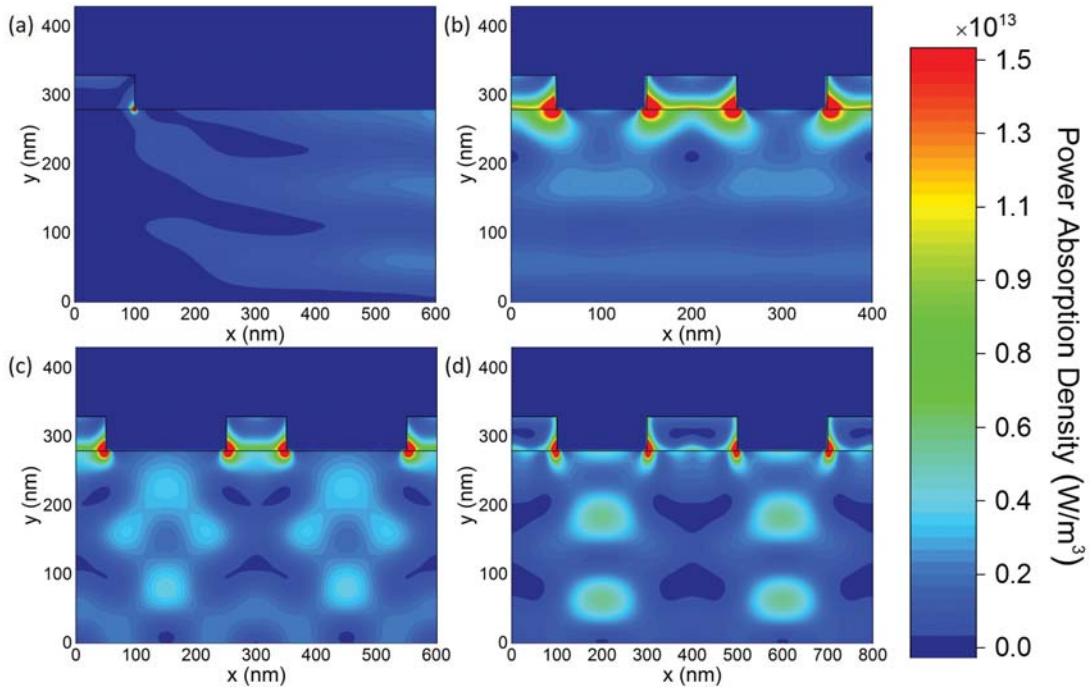

Figure 6.3: Simulated optical power absorption by different plasmonic geometrics at optical wavelength of 800 nm. (a) non-plasmonic structure; (b) $a = 100$ nm, $p = 200$ nm; (c)$a = 100$ nm, $p = 300$ nm, (d)$a = 200$ nm, $p = 400$ nm.

Figure 6.3 first illustrates the effect of the periodic metal structure. For conventional THz PCAs without the periodic structure, the optical power density is merely distributed uniformly inside the substrate, with very weak confinement of the optical field at the metal/semiconductor interface, as shown in Fig. 6.3(a). The optical confinement is caused by discontinuity in the boundary condition, as discussed in Sec. 3.3. With the geometric parameters of $p = 200$ nm, $a = 100$ nm, LSPR was excited at the metal-substrate interface, and confinement of optical absorption was realised, as shown in Fig. 6.3(b). The peak power absorption density (PAD) was approximately 10^4 stronger than that without the periodic structure. The influence of the geometry of the periodic metallic slits on the existence of LSPR is shown in Fig. 6.3(c). As p increased to 300 nm, the confinement of optical absorption at the metal-substrate inter-

face weakened dramatically. The peak absorption density dropped by 30%, while the area of strong absorption significantly reduced. By further increasing p to 400 nm, the strong absorption area at the metal-substrate interface continued to reduce, as shown in Fig. 6.3(d). However, comparing to Fig. 6.3(a), an enhancement in absorption was created inside the substrate between the spacing areas of the metal slits. In the simulated area, the increment of absorbed optical power was 67.3%. The enhanced absorption area situated away from the metal-substrate interface. These enhanced absorption areas not created by SPs, but the diffraction of the incident optics.

6.3 Coupling Between Enhanced Absorption and Photogenerated Carriers

One of the unique characteristics of the THz radiation process from PCAs is its ultrafast transient nature. As a result, the influence of the plasmonic structure on the photoconductive process is not only determined by the SPs, but also the carrier properties in the photoconductive substrate. Here, in this work, the concept of enhance area is proposed for studying the coupling between the enhanced absorption caused by EOT and the properties of the carriers. Figure 6.4 illustrates the enhanced area in the ultrafast photoconductive process.

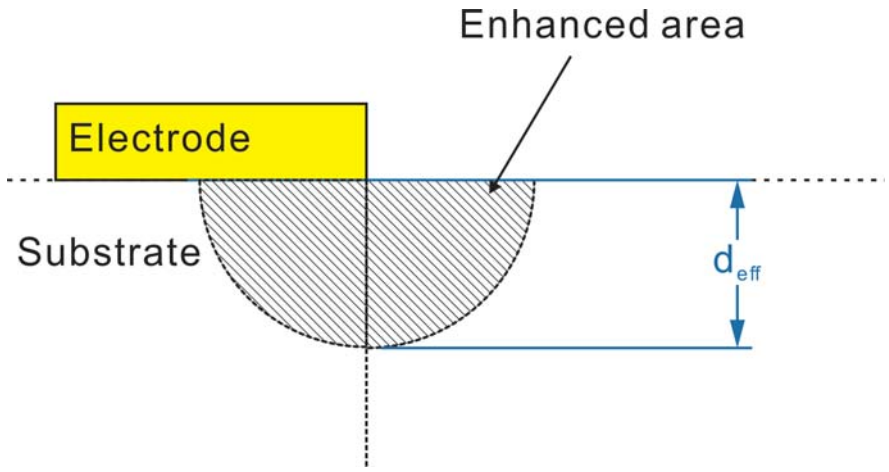

Figure 6.4: The enhanced area in the ultrafast photoconductive process. The carriers in the enhanced area can reach the electrode before recombined/scattered.

As illustrate in Fig. 6.4, the enhanced area refers to the region in the substrate adjacent to the metal-substrate contact. The carriers (electrons) generated in this area can be effectively transmitted to the electrodes, leading to a faster photoconductive response, and subsequently an enhanced THz radiation. The dimension of the enhanced area d_{eff} is determined by the carrier property of the substrate.

Here, the coupling between the enhanced absorption caused by EOT and the photo-generated carriers is evaluated by the average optical PAD within the enhanced area. The average PAD, P_{avr}, is defined as,

$$P_{avr} = \frac{\iint_{A_{eff}} P_a(r) dS}{A_{eff}}, \tag{6.3}$$

where $P_a(r)$ is PAD at location r, A_{eff} is the area of the enhanced area.

Two specific scenarios were considered [16]. For substrates with short carrier lifetime (LT-GaAs), this corresponds to the mean path length of electrons before recombination. A typical value is $d_{eff} \approx 20\ nm$ for $\tau_c = 200\ fs$; for substrates with long carrier lifetime (SI-GaAs), this refers to the path length of ballistic transport. A typical value of d_{eff}

for this scenario is $d_{eff} \approx 200\ nm$. Figures 6.5 and 6.6 show the dependence of the average optical PAD in the enhanced area to the geometry of the periodic metallic slits. The average optical PAD for optical excitation between 750 nm and 850 nm is mapped regarding the two geometric parameters p and a/p.

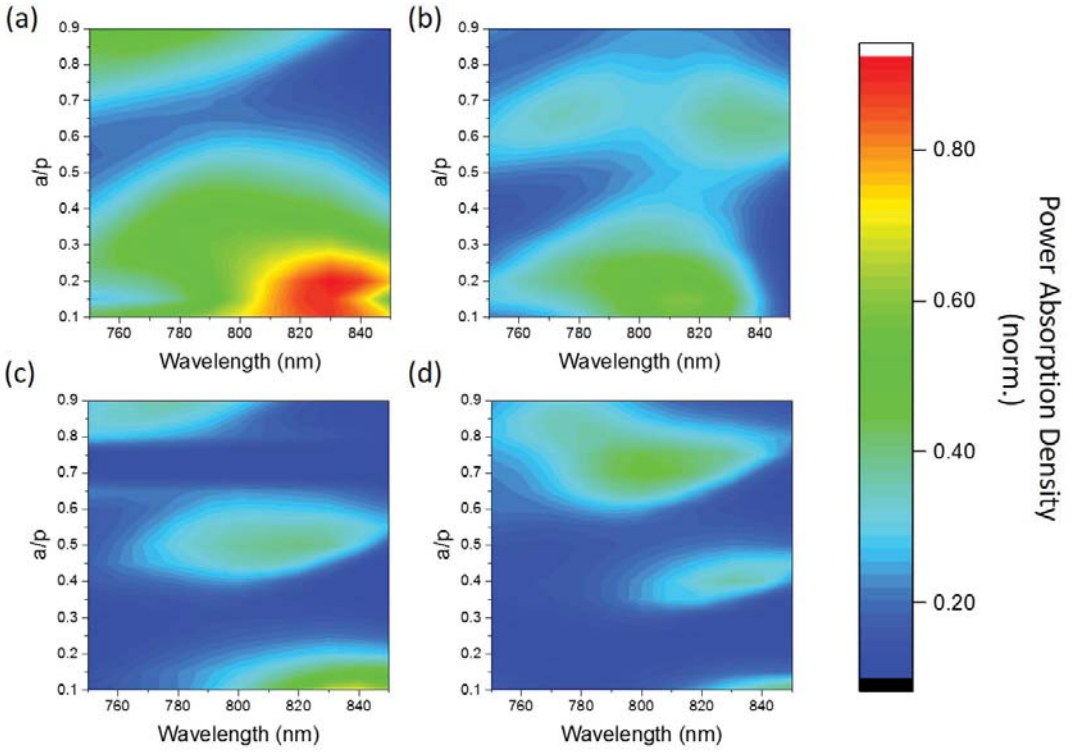

Figure 6.5: Geometric dependence of the average power absorption density in the effective area for $d_{eff} = 20$ nm. (a) $p = 200$ nm; (b) $p = 300$ nm; (c) $p = 400$ nm; (d) $p = 500$ nm.

The results in Figs. 6.5 and 6.6 demonstrate different geometric dependence of the average optical PAD for photoconductive substrates with different d_{eff}. For $d_{eff} = 20$ nm, the average PAD is more dependent on geometric of the periodic metallic slits. Maximum optical absorption is realised at $\lambda = 830$ nm, $p = 200$ nm and $a = 40$ nm. As the geometric changes, the PAD reduces rapidly. In comparison, for $d_{eff} = 200$ nm,

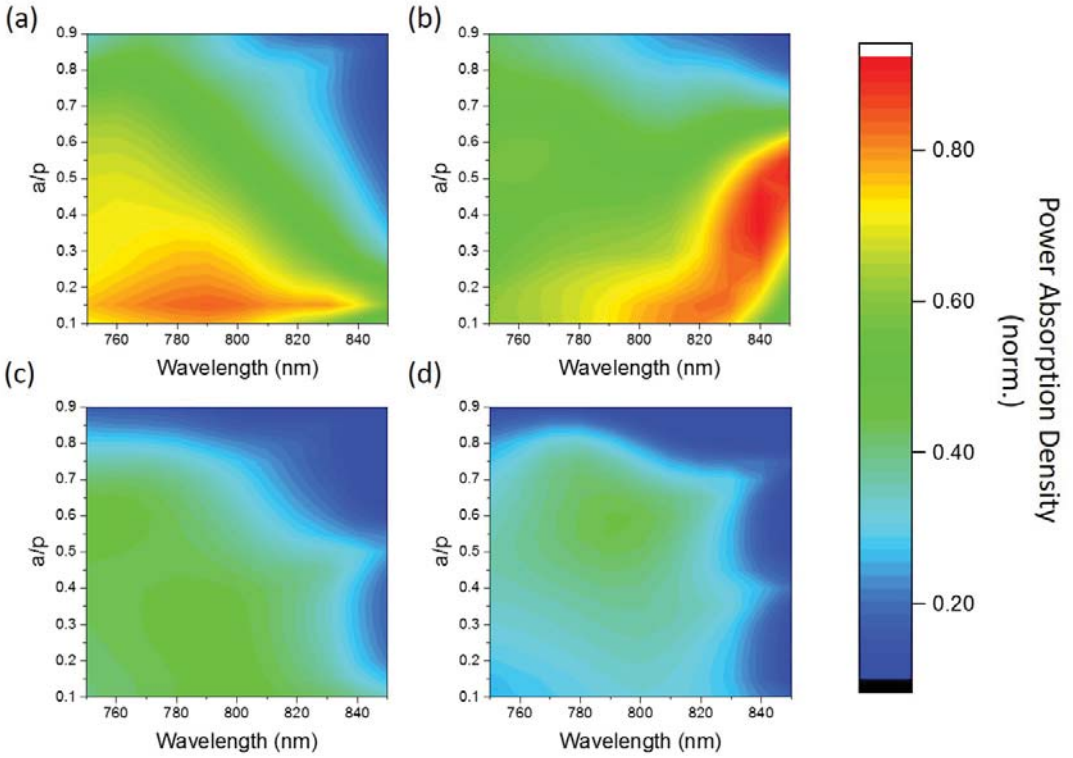

Figure 6.6: Geometric dependence of the average power absorption density in the effective area for d_{eff} = 200 nm. (a) p = 200 nm; (b) p = 300 nm; (c) p = 400 nm; (d) p = 500 nm.

maximum absorption in the enhanced area occurs at λ = 840 nm, p = 300 nm and a = 150 nm. A large value of PAD can be maintained as the geometry of the periodic structure alters. The distribution of optical power absorption for these two conditions is shown in Fig. 6.7.

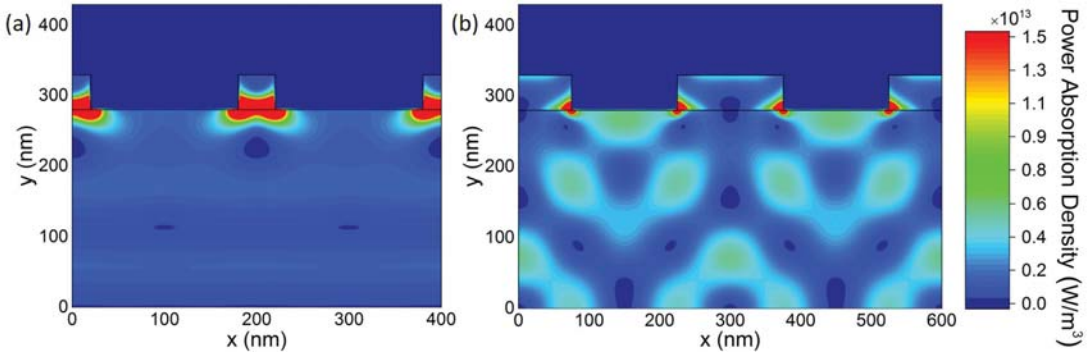

Figure 6.7: Distribution of optical power absorption for (a) d_{eff} = 20 nm; (b) d_{eff} = 200 nm. SPs are excited in (a), while the effect of optical diffraction dominates in (b).

Figure 6.7 shows different mechanisms in enhanced optical absorption correlated to the carrier properties. As illustrated in Fig. 6.7, the maximum optical absorption for d_{eff} = 20 nm was mainly contributed to by the confined optical absorption caused by EOT, while the resonance with SPs were compromised to match the relatively small enhanced area (compared to Fig. 6.3(b)). In contrast, the maximum optical absorption for d_{eff} = 200 nm was jointly contributed to by the confined absorption and the diffraction of the optical beam, with the effect of diffraction dominating. The enlarged enhanced area caused by large d_{eff} offers the possibility to take advantage of the enhance absorption caused by optical diffraction inside the substrate. This can also explain the lower sensitivity of PAD to the geometry of the periodic metallic slits, by comparing the geometric dependence in Figs. 6.5 and 6.6.

The difference in contribution of enhanced optical absorption due to carrier properties also leads to different sensitivity dependence to the polarisation of the incident optical beam. The relationship between the PAD and the rotation of the optical beam polarisation for short and long lifetime substrate materials is calculated and shown in Fig. 6.8, corresponding to the optimum structures illustrated in Fig. 6.7.

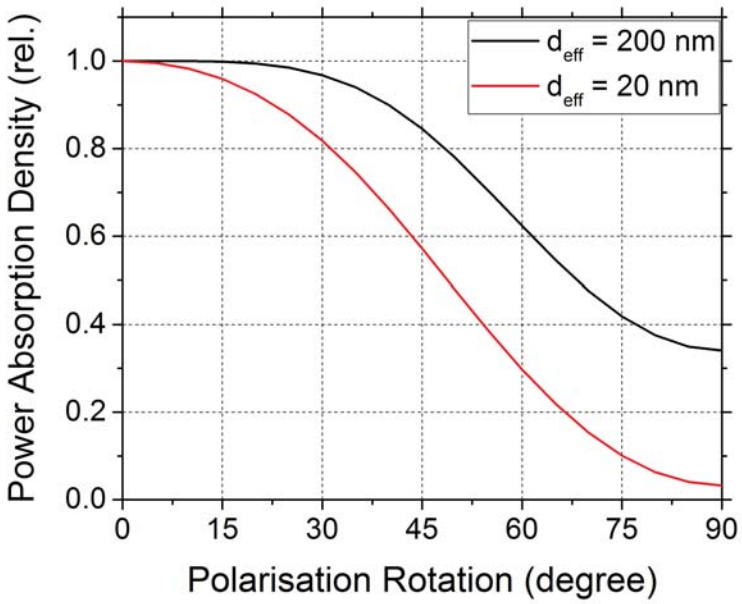

Figure 6.8: Polarisation dependence of average power absorption density of d_{eff} = 200 nm and d_{eff} = 20 nm. 0° refers to TM wave incident, 90° refers to TE wave.

As shown in Fig. 6.8, a TM wave incidnet is vital to the enhanced optical absorption in plasmnoic-incooperated THz PCAs. The trend of alteration in PAD is similar to that discussed in the work of Park *et al.* [2]. Meanwhile, the average PAD drops much faster for substrates for short carrier lifetimes (small d_{eff}) with larger decrement, when the polarisation of the incident optical beam shifts from TM to TE. For the case of d_{eff} = 20 nm, the difference in PAD for TM and TE incidence is nearly 30 times; while for d_{eff} = 200 nm, this ratio reduces to 2.3. The weakened polarisation sensitivity for long-lifetime substrates originates from its ability to couple the optical absorption from the diffracted wave, as the diffraction process is less polarisation-dependent compared to the excitation of SPPs.

6.4 Fabrication and Experimental Measurement

Here in this section, the performances of plasmonic incorporated THz PCAs are examined experimentally.

The configuration of the designed plasmonic incorporated PCAs are similar to that demonstrated in Fig. 6.1, while plasmonic structures are only attached to the anode, corresponding to the proposed location of optical incident. The gap dimension of the PCAs is set as 70 μm, while the length of the plasmonic structures is 20 μm. Within the plasmonic incorporated area, periodic metal slit structures with different periods (from 200 nm to 400 nm) and spacings (from 50 nm to 200 nm) are designed.

The nanometre scale plasmonic structure were fabricated by electron-beam lithography on SI-GaAs substrates (James Watt Nanofabrication Centre, University of Glasgow). Gold electrodes corresponding to the designed structures were deposited onto the substrates. The thickness of the gold layer was 50 nm. Figure 6.9 provides scanning electron microscope (SEM) images of selected fabricated plasmonic incorporated THz PCAs.

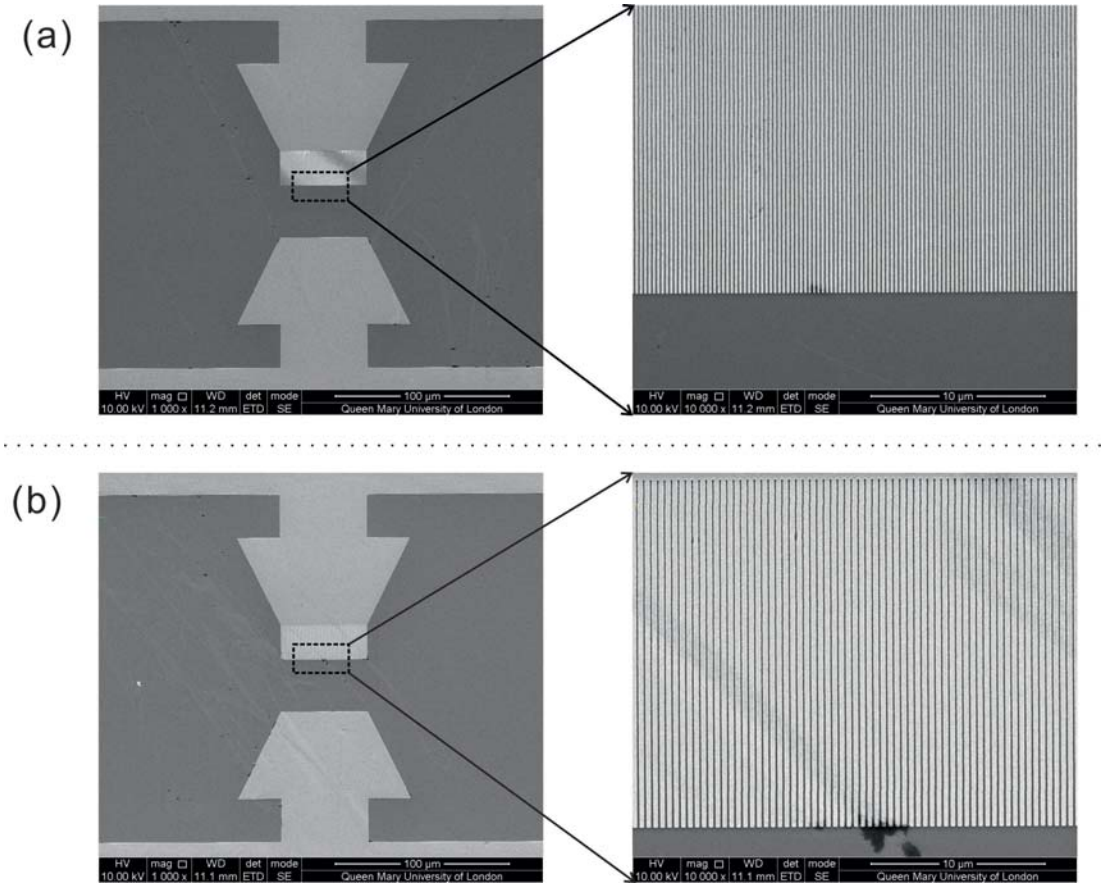

Figure 6.9: Scanning electron microscope images of selected THz PCAs with plasmonic electrodes. The images in the right column zoom into the plasmonic grating areas on the anodes. (a) $p = 200$ nm, $a = 100$ nm; (b) $p = 400$ nm, $a = 200$ nm

The error of the fabrication was within 10 nm. Overall, good agreement between the design and fabrication was met.

The performances of the fabricated plasmonic incorporated PCAs were tested on the THz-TDS bench used in previous experiments. Figure 6.10 shows the measured THz radiation from several selected THz PCAs. The signal amplitudes are normalised to the peak amplitude of the THz signal from conventional THz PCAs to demonstrate

the influence of the plasmonic structure.

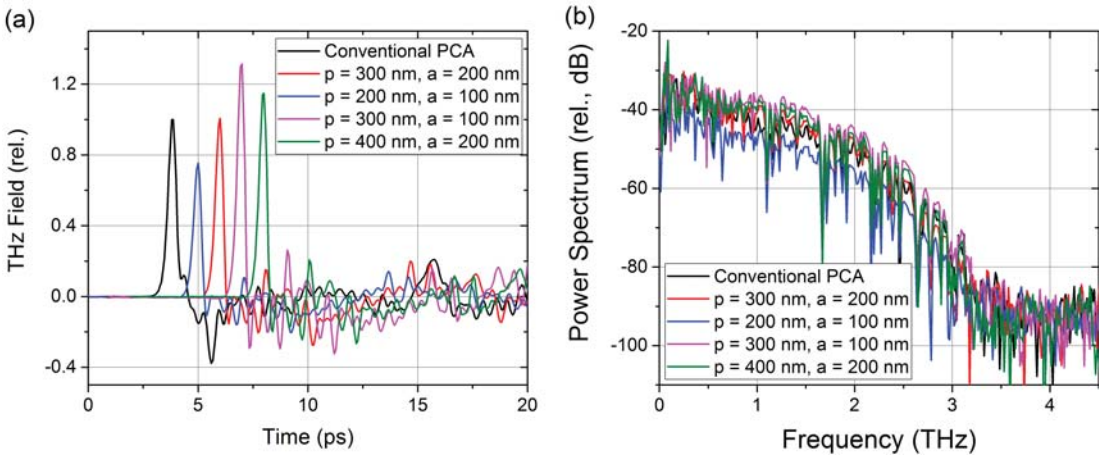

Figure 6.10: Measured THz radiation from conventional THz PCA and plasmonic incorporated THz PCAs with different geometric configurations. (a) Time domain signal normalised to the peak amplitude of conventional PCA; (b) power spectrum normalised to the same noise floor.

Geometric dependence of the performance of the plasmonic incorporated THz PCAs were observed in the measurement, as illustrated in Fig. 6.10. However, the significant enhanced THz radiation corresponding to EOT caused by the plasmonic structure was not realised. The radiated THz field from the plasmonic incorporated THz PCAs could be either weaker (p = 200 nm, a = 100 nm) or stronger (p = 300 nm, a = 100 nm and p = 400 nm, a = 200 nm) than that from conventional THz PCAs. In the time domain, the maximum realised enhancement in amplitude was less than 30%, while in the frequency domain, the alteration in DR was within 10 dB.

The enhancement observed in the measurement is suggested to originate from the diffraction of optical beam rather than the confined optical absorption. This statement is based on: (a) the capability of SI-GaAs substrate (long carrier lifetime) to incorporated with the enhanced absorption caused by diffraction (as discussed in Sec. 6.3); and

(b) the reduced amplitude at $p = 200$ nm, $a = 100$ nm due to the weakened diffraction (as shown in Fig. 6.3).

The unsuccessful demonstration of performance enhancement from plasmonic incorporated THz PCAs in experiment is suggested to be caused by the following reasons:

1. Optical saturation: The plasmonic structures on the photoconductive substrates lead to highly concentrated optical fields at the metal-semiconductor interface, as shown in Fig. 6.3. As discussed in Sec. 5.1, this enhanced optical field can result in saturation in the THz radiation process. Since the distribution of optical field is highly confined at the surface, the threshold optical intensity for saturation should be much lower than that in conventional PCAs. In measurements here, the average power of the optical beam was approximately 300 mW. In comparison to the optical power used in the work of Berry *et al.* (below 30 mW) [4], optical saturation could also be a reasonable cause for the reduce amplification in THz radiation.

2. Polarisation of the excitation optical beam: SPs can only be excited in TM modes. A matched polarisation between the optical beam and the periodic structure is vital for the excitation of SPs. Due to limitations in the experimental environment, the polarisation of the optical beam might not be precisely checked and aligned. The momentum matching condition was therefore not met, and SPs were not efficiently generated. In contrast, the diffraction of optical beam is less dependent to polarisation. As a result, a relatively weak radiation enhancement caused by diffraction was observed in experiment.

3. Structural defects on electrodes: The fabricated plasmonic structures were reasonably accurate, as shown in Fig. 6.1. However, defects do exist at the connection between the large electrode pads and the plasmonic structures, as illustrated in Fig. 6.11. These defects can lead to electrical connection failure between the plasmonic structure and the electrodes.

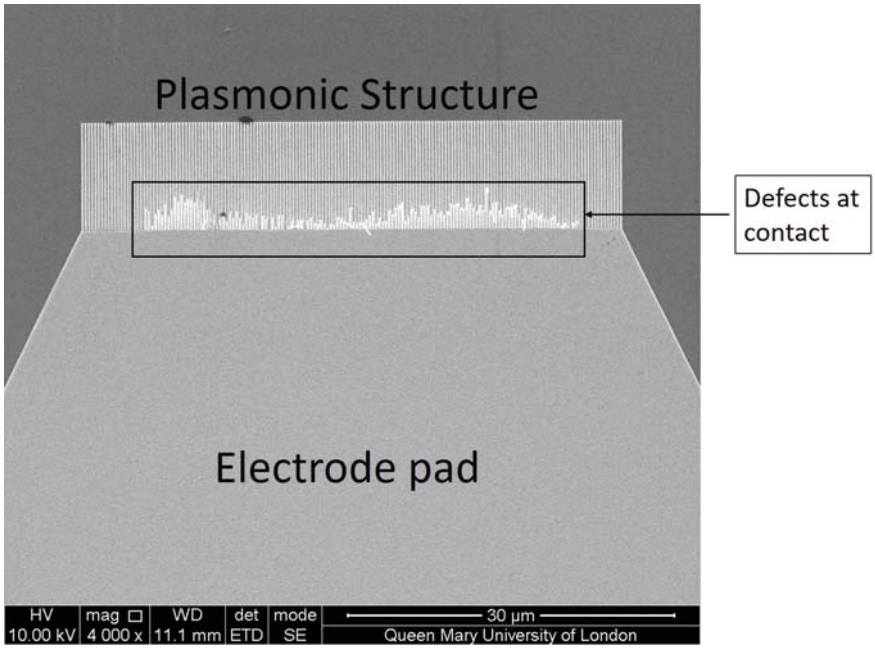

Figure 6.11: Defects at the contact between electrode pad and the plasmonic structure.

The electrical connection plays a significant role in the realisation of amplified photocurrent, by transporting the generated carriers in the enhanced absorption area to the electrode pads. In the work of Park *et al.* [2], plasmonic structures similar to [4] are used, but without the electrical connection between the plasmonic structure and the electrode pad. The power amplification ratio reduces to less than 3 times, which is much lower than that with the electrical connection (50 times in [4]). However, in practise, it is difficult to eliminate the defects with one-step electron-beam lithography due to the dramatic change in the structural dimensions.

6.5 Summary

In this chapter, the concept of incorporating surface plasmons to enhance the performance of THz PCAs was reviewed and examined. The principles for the generation of

SPs and the phenomenon of extraordinary optical transmission were reviewed. EOT was realised in simulation with respect to the specific scenario of THz wave generation from photoconductive process. The influence of the geometric parameters of the periodic gold slits were discussed.

In consideration of the transient nature of the ultrafast photoconductive process, the concept of enhanced area was proposed to evaluated the coupling between the enhanced absorption from EOT phenomenon and the photo-generated carriers in the substrate. The coupling efficiency was evaluated by the average power absorption density in the enhanced area. Specifically, the scenarios for photoconductive substrates with short and long carrier lifetimes (d_{eff} = 20 nm and d_{eff} = 200 nm, respectively) were evaluated and compared. Optimum geometrics for these two scenarios were demonstrated. For substrates with short carrier lifetimes, the maximum optical absorption was mostly contributed to by the confined absorption caused by EOT, while for substrates with long carrier lifetimes, the maximum optical absorption was mostly contributed to by the diffraction of optical beam. The difference in contribution of the enhanced optical absorption also leads different polarisation dependence of the plasmonic-incorporated THz PCAs. Substrates with long carrier lifetimes were realised to be less sensitive to polarisation as diffraction of optical beam is less polarisation dependent.

In the end of this chapter, plasmonic incorporated THz PCAs were fabricated and tested experimentally. Unfortunately, the dramatic enhancement in THz radiation correlated to EOT was not observed in the measurements. Relatively low levels of enhancement in THz radiation (approximately 30% in E-field amplitude) were observed. This enhancement was suggested to be caused by the diffraction of the periodic metallic structure. Possible reasons for the unsuccessful demonstration of EOT were discussed.

References

[1] S. Lepeshov, A. Gorodetsky, A. Krasnok, E. Rafailov, and P. Belov, "Enhancement of terahertz photoconductive antenna operation by optical nanoantennas," *Laser and Photonics Reviews*, pp. 2026–2031, 2016.

[2] S.-G. Park, K. H. Jin, M. Yi, J. C. Ye, J. Ahn, and K.-H. Jeong, "Enhancement of terahertz pulse emission by optical nanoantenna," *ACS Nano*, vol. 6, no. 3, pp. 2026–2031, 2012.

[3] S.-G. Park, Y. Choi, Y.-J. Oh, and K.-H. Jeong, "Terahertz photoconductive antenna with metal nanoislands," *Optics Express*, vol. 20, no. 23, pp. 25 530–25 535, 2012.

[4] C. Berry, N. Wang, M. Hashemi, M. Unlu, and M. Jarrahi, "Significant performance enhancement in photoconductive terahertz optoelectronics by incorporating plasmonic contact electrodes," *Nature Communications*, vol. 4, p. 1622, 2013.

[5] Y. Shang-Hua, M. R. Hashemi, C. W. Berry, and M. Jarrahi, "7.5% optical-to-terahertz conversion efficiency offered by photoconductive emitters with three-dimensional plasmonic contact electrodes," *Terahertz Science and Technology, IEEE Transactions on*, vol. 4, no. 5, pp. 575–581, 2014.

[6] A. Singh, H. Surdi, V. V. Nikesh, S. S. Prabhu, and G. H. Dohler, "Improved efficiency of photoconductive thz emitters by increasing the effective contact length of electrodes," *AIP Advances*, vol. 3, no. 12, 2013.

[7] W. L. Barnes, A. Dereux, and T. W. Ebbesen, "Surface plasmon subwavelength optics," *Nature*, vol. 424, no. 6950, pp. 824–830, 2003.

[8] J. Pendry, L. Martin-Moreno, and F. Garcia-Vidal, "Mimicking surface plasmons with structured surfaces," *Science*, vol. 305, no. 5685, pp. 847–848, 2004.

[9] T. W. Ebbesen, H. J. Lezec, and H. F. Ghaemi, "Extraordinary optical transmission through sub-wavelength hole arrays," *Nature*, vol. 391, no. 6668, pp. 667–669, 1998.

[10] L. Wu, P. Bai, and E. P. Li, "Designing surface plasmon resonance of subwave-

length hole arrays by studying absorption," *Journal of the Optical Society of America B*, vol. 29, no. 4, pp. 521–528, 2012.

[11] G. J. Kowalski, A. Talakoub, J. Ji, J. G. OConnell, M. Sen, and D. Larson, "Fast temperature sensing using changes in extraordinary optical transmission through an array of subwavelength apertures," *Optical Engineering*, vol. 48, no. 10, pp. 104 402–104 402, 2009.

[12] Z. Li, A. W. Clark, and J. M. Cooper, "Annular nanoplasmonic void arrays as tunable surface enhanced raman spectroscopy substrates," *Applied Physics Letters*, vol. 105, no. 3, p. 033115, 2014.

[13] S. A. Maier, *Plasmonics: fundamentals and applications*. Springer Science & Business Media, 2007.

[14] B. Y. Hsieh and M. Jarrahi, "Analysis of periodic metallic nano-slits for efficient interaction of terahertz and optical waves at nano-scale dimensions," *Journal of Applied Physics*, vol. 109, no. 8, 2011.

[15] S.-H. Yang and M. Jarrahi, "Enhanced light matter interaction at nanoscale by utilizing high-aspect-ratio metallic gratings," *Optics Letters*, vol. 38, no. 18, pp. 3677–3679, 2013.

[16] G. Carpintero, E. Garcia-Munoz, H. Hartnagel, S. Preu, and A. Räisänen, *Semiconductor Terahertz Technology: Devices and Systems at Room Temperature Operation*. John Wiley and Sons, 2015.

Chapter 7

Conclusions and future work

7.1 Summary

THz-TDS techniques play a significant role in THz science and technology. The objective of this research work is to improve of the performance of THz-TDS systems and to explore the boundary of the technique.

Concentrating on this objective, a thorough review of the operation principles of THz-TDS systems is provided in **Chapter 2**. The limitations of the technique were assessed with respect to dynamic range, signal-to-noise ratio and spectral resolution. The influence of systematic operation parameters on the overall performance of the system were addressed. The detection time-constant in the lock-in amplification scheme τ_{LIA} and the internal reference frequency f_r are shown to play different roles concerning noise cancellation in the system. τ_{LIA} mostly contributes to the suppression of external noise, while f_r is responsible for the suppression of the fluctuation in the detected THz field (internal noise). With parameters optimised, up to 10 dB of improvement in dynamic range and signal-to-noise ratio was observed in experimental measurement.

The key to extend the measurement capability of THz-TDS systems is to improve

the performance of the broadband THz source. In **Chapter 3**, a systematic characterisation was undertaken of on THz PCAs, one of the most commonly used THz source devices in THz-TDS systems. The influence of the excitation condition of the THz PCA was described in terms of intrinsic and extrinsic excitation parameters. Optimal relations for the two most influential intrinsic excitation parameters, pulse duration of the excitation optical beam τ_p and the carrier lifetime of the substrate material τ_c, were established in this study. Two optimum ratios between τ_p and τ_c were found to be $\eta_1 = 0.1$ and $\eta_2 = 0.6$, correspond to the scenarios of maximum bandwidth and high power radiation, respectively. The extrinsic excitation parameters studied in this work were the bias electric field and the spatial character of the excitation optical beam. The influence of the bias electric field was analysed with regard to its amplitude and spatial distribution across the photoconductive gap area. The influence of the optical expectation geometry was analysed with a revised equivalent circuit model. Optimum excitation strategies for low and high optical excitation intensities were derived. Experimental measurements were carried out to validate the proposed theorem. Finally, a numerical model was developed to evaluated the power collection efficiency in the power collection scheme typically implemented in THz-TDS systems. Again, the proposed model was validated by experimental measurement.

A methodology for analysing the alignment sensitivity of the quasi-optic subsystem in THz-TDS was introduced in **Chapter 4**. Specifically, the sensitivity of the system to misalignment of the broadband THz source was extensively addressed. Assessments were carried out in regard to the frequency domain and time-domain response of the electric field as well as its spatial distribution. High frequency components in the broadband THz pulse were realised to be more sensitive to misalignment due to their nature of having associated with small wavelengths. Meanwhile, the E-field response was demonstrated to be more sensitive to misalignment transverse to the beam axis in the quasi-optic system. On the other hand, experimental measurements indicate that the instability corresponding to source location error can be partially compensated

with an enlarged probe beam. Mode analysis was performed to quantitatively assess the alteration in field distribution. Non-dispersive mode coupling patterns were discovered.

In **Chapter 5**, the concept of antenna array is applied to THz PCAs. Systematic performance analysis of THz PCA arrays based on array factor study was presented. Depending on the opitcal illuminated scheme, array factors for the scenarios of continuous and discrete arrays were examined in sequence. Continuous array refers to the scenario of THz PCAs excited with an optical beam of finite dimension. The influence of excitation beam waist on the radiation characteristics was examined. Critical condition for directional radiation was established and confirmed in experiment. The general realisation for discrete THz PCA arrays is in the form of interdigitated electrodes. The geometric dependence of the array factor was extensively examined with respect to excitation area, periodicity of interdigitation and gap dimension. Interdigitated THz PCAs were fabricated and tested to validate the theorem. The difference between the predicted and measured critical frequency for the appearance of the first side lobe was within 4%.

Finally, in **Chapter 6**, the novel approach of enhancing the THz radiation from PCAs with electrodes incorporating plasmonic-supporting features was reviewed and tested. Geometric optimisation was carried out in consideration of the transient characteristics of the carriers in the photoconductive substrates. The scenarios for substrates with short and long carrier lifetimes were evaluated and compared. The maximum optical power absorption realised for short carrier lifetime is contributed to by the confined absorption at the metal-substrate interface; while the maximum condition for the situation of long carrier lifetime is dominant by the diffraction of the optical beam inside the substrate. Plasmonic incorporated THz PCAs were fabricated and tested experimentally. Dramatic radiation enhancement from extraordinary optical transmission was not observed, while weak enhancement correlated to diffraction was realised. Possible causes for the unseen dramatic enhancement were addressed and discussed. Possible reasons include the misalignment of the polarisation of the optical beam to

the plasmonic structure, optical saturation in the photoconductive substrates due to strong confinement of the optical power, and electrica connection failure caused by defects in fabrication.

7.2 Future work

Concluding the research within this study, aspects of potential further research are given as following,

1. **Further development of the alignment sensitivity assessment model.** In Chapter 4, the influence of location error in the THz source was extensively studied. Meanwhile, the evaluation method can be easily adapted. With Hermite-Gaussian mode analysis, a quantitative understanding is provided in regard to the beam profile within the QO system. Further development of this assessment method could focus on not only the influence of misalignment of other QO components, but also on the beam profile within the QO system, which is of great importance for imaging applications.

2. **Experimental demonstration of plasmonic-incorporating THz PCAs.** In the experimental measurement of Chapter 6, the demonstration of THz radiation enhancement from plasmnoic electrodes was not observed. Considering the possible reasons for the unsuccessful experiment, suggestions for further explorations are as following:

   (a) Precise measurement of relevant optical parameters. The polarisation and intensity of the excitation optical beam strongly affect the performance of the plasmonic-incorporated PCAs. These parameters should be precisely measured in future measurements;

   (b) Measurement of carrier properties in the photoconductive substrate. This work

demonstrates that the amplification of photocurrent due to enhancement in optical absorption is dependent on the carrier properties in the semiconductor substrate. However, in this work, the carrier properties (carrier lifetime, mobility etc.) are not measured. Future experiment should measure these properties in order to evaluated the performance of the device;

(c) Improved fabrication process. The defects at the connection area between the plasmonic structures and large electrode pad can cause catastrophic effects in the operation of plasmonic incorporated THz PCAs. The dramatic change in dimension makes it difficult to eliminate the defects in a one-step process (solely electron-beam lithography). A two-step process combining photo-lithography with electron-beam lithography might be able to overcome this problem, and achieve good electrical contact between the plasmonic structures and large electrode pad.

3. **Full excitation condition characterisation of THz PCAs through the proposed equivalent circuit model.** In the measurement presented in Sec. 3.2.2, the excitation factor was correctly measured with the proposed equivalent circuit model. Meanwhile, one key factor, the radiation factor η_r, was nonetheless undetermined. Further work should be carried out (with a controllable optical excitation condition) to measure and determine this factor.

Appendix A

Author's publications

Journal Papers:

1. **Yang Zeng**,Theo Kreouzis, Xiaodong Chen, Robert Donnan, "Principles of Optimisation for Interdigitaed Terahertz Photoconductive Antennas," (in preparation)

2. **Yang Zeng**, Bin Yang, Robert Donnan, "Investigation of Source Alignment Sensitivity in a Terahertz Time-Domain Spectroscopy System," (to be submitted)

3. **Yang Zeng**, Marc Edwards, Robert Donnan, Robert Stevens, Bin Yang, "Terahertz Characterization of UV Offset Lithographically Printed Electronic-Ink ," (submitted to Organic Electronics)

4. Chuying Yu, **Yang Zeng**, Bin Yang, Haixue Yan, *et al.*, "Terahertz-tailored Titanium Dioxide Simultaneously Possessing Non-resonant High Permittivity and Ultra-Low-Loss" (submitted to Nature Communications)

5. Xiang Li, Xiaoming Liu, Kevin Ronald, Wenlong He, **Yang Zeng**, Yasir Alfadhl, Robert Donnan, Adrian Cross, Xiaodong Chen, Investigation of Frequency Selective Surfaces for a THz Gyro-Multiplier Output System, (submitted to IEEE

Transaction on Electron Device)

Conference Papers:

1. **Yang Zeng**, Xiaodong Chen, Robert Donnan, "Analysing and Modelling of Photoconductive Antennas for Terahertz Wave Generation", The IV Workshop of Theory, Modelling and Computational Methods for Semiconductors, 22-24 Jan., 2014, Manchester, UK.

2. **Yang Zeng**, Theo Kreouzis, Xiaodong Chen, Robert Donnan, "Efficiency Evaluation and Analysis of High Power Broadbansd Interdigitated-Electrode Terahertz Photoconductive Antennas", Photon 14, 1-4 Sep., 2014, London, UK.

3. **Yang Zeng**, Theo Kreouzis, Xiaodong Chen, Robert Donnan, "Study of Terahertz Radiation Generation From Photoconductive Antennas and Interdigitated Arrays", The 7th Millimeter Waves and THz Technology Workshop, 1-5 Sep., 2014, Chengdu, China.

4. **Yang Zeng**, Theo Kreouzis, Xiaodong Chen, Robert Donnan, "Efficiency and Spectrum Evaluation of Terahertz Photoconductive Antenna Array Based on GaAs Substrates", The 39th International Conference on Infrared, Millimetre and THz wave, 14-19 Sep., 2014, Tuscon, USA.

5. **Yang Zeng**, Andre Sarker Andy , Theo Kreouzis , Xiaodong Chen , Robert S. Donnan, "Beam profile measurement of THz pulses in a TDS system", The 39th International Conference on Infrared, Millimetre and THz wave, 14-19 Sep., 2015, Hong Kong, China.

Appendix B

Alignment of THz-TDS Systems

The procedure for the alignement of THz-TDS systems is introduced here. This procedure was used routinely on the THz-TDS bench in the Antennas Lab, QMUL throughout this study. A full layout of the THz-TDS bench (including all the components) and its photograph is shown in Fig. B.1.

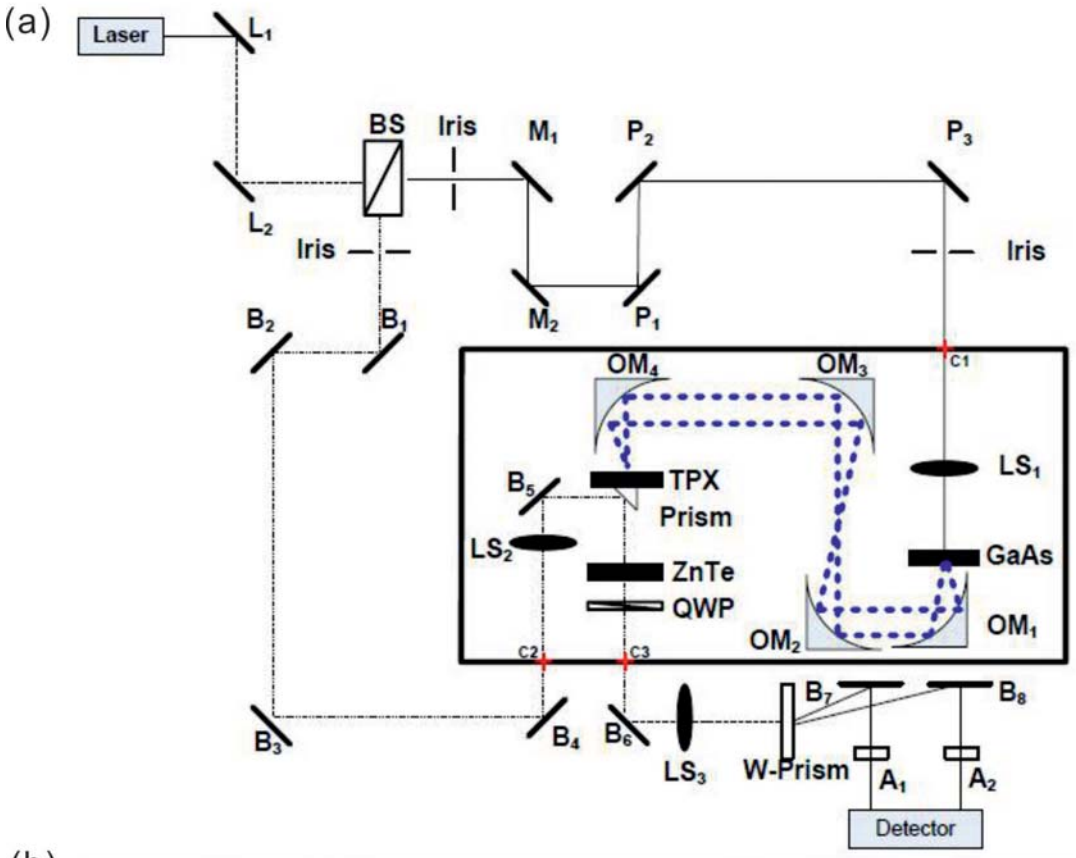

Figure B.1: (a)Full layout of the THz-TDS system in QMUL including all the components with notations; (b) photograph of the system.

The alignment procedure is described as following. The notations are as shown in Fig. B.1.

1. Routine alignment tips.

   (a) In alignment the optic power should firstly be heavily attenuated for safety;

   (b) The height of the centre of the QO system is set at approximately 8.9 cm in the system (pre-set height); while the height of the laser source is 10.83 cm. Heights can be marked with irises or target papers for alignment;

   (c) Lens adjustment. Place the lens in a optic beam path parallel to the optic table. Two reflection spots should be observed, corresponding to the front and back surfaces of the lens. A proper lens adjustment should make these reflection spots coincide, and matches to the input optic;

   (d) Two-mirror adjustment method. This method is used when height adjustment is required in the system. Two mirrors and two height marks are used in combination to ensure that the output beam is parallel to the optic table. Take the beam path between P_2 and P_3 for example to introduce this method. Place two pre-set irises I_1 and I_2 between P_2 and P_3, I_1 close to P_2 and I_2 far from P_2. Close I_1 and adjust P_1 to let the laser beam pass through I_1; then open I_1, close I_2, adjust P_2 let the laser pass through I_2. Repeat this process until the laser can pass through I_1 and I_2 simultaneously;

   (e) One-mirror adjustment method. This method is used to match the output of a mirror to the input beam that is already parallel the optic table. Place a height marker on the expected reflection beam path, and adjust the mirror to match the height of the marker.

2. Alignment of motor stage.

   (a) Set the laser beam between L_2 and M_1 parallel to the optical stage. Set a

target paper on the motor stage. Mark the position of the laser spot and observe the movement of the laser spot as the motor stage moves backward and forward. Adjust L_1 and L_2 with the two-mirror adjustment method;

(b) Mark the height of the laser beam between L_2 and M_1 using an iris. Adjust M_1 with the one-mirror adjustment method to collimate the laser between M_1 and M_2. Repeat this process to collimate the laser between M_2 and P_1.

3. Alignment of the pump beam.

(a) Apply the two-mirror adjustment method to P_1 and P_2 to adjust the height of the laser between P_2 and P_3 to the pre-set height, and parallel to the optic stage;

(b) Apply the one-mirror adjustment method to P_3 to collimate the pump beam

(c) Use the collimated beam after P_3 to align lens LS_1.

4. Setting up the detection path.

(a) Apply the two-mirror adjustment method to B_2 and B_3 to adjust the height of the laser between B_3 and B_4 to the pre-set height, and parallel to the optic stage;

(b) Use the collimated beam after P_3 to align lenses LS_2 and LS_3.

(c) Align B_4, B_5 and the refection surface of TPX Prism in sequence with the one-mirror adjustment method.

5. Alignment of the QO path.

(a) Place a membrane paper in the pump path to diverge the laser beam. The diverted beam will be used to represent the behaviour of the THz wave in the alignment process;

(b) Monitor the reflection beam from OM_1. Adjust OM_1 to make the reflection beam parallel to the optic table. Continue to monitor the reflection from OM_1. Adjust OM_1 to create a collimated circular reflection;

(c) Adjust OM_2 to make its reflection surface fully illuminated by the reflected beam from OM_1. Then, monitor the reflection beam from OM_2 at its focus. Adjust OM_2 to get the centre of the focused beam to the pre-set height;

(d) Place OM_3 approximately 20 cm from OM_2. Adjust OM_3 to make its reflection surface fully illuminated by the reflected beam from OM_2. Then, monitor the reflection beam from OM_3. Adjust OM_3 to create a collimated circular reflection;

(e) Place OM_4 at the intersection between the reflection from OM_3 and the extension of the probe beam. Adjust OM_4 to make its reflection surface fully illuminated by the reflected beam from OM_3. Then, monitor the reflection beam from OM_3. Adjust OM_4 to make the centre of the reflected beam coincide with and travel along with the probe beam.

6. Balance detector settings.

(a) Insert the aligned LS_2 into the probe path. Make the focus of LS_2 approximately lies in the centre of the reflection beam from OM_4;

(b) Set the ZnTe crystal at the focus of LS_2. Place the quarter wave plate (QWP) afterwards;

(c) Align B_6, B_7 and B_8 in sequence with the one-mirror adjustment method. The distance between the reflection beam from B_7 and B_8 is set to match the distance between the photo-diodes.

(d) Block the pump path and set the balanced detector to balance mode. Adjust attenuators A_1 and A_2 for balanced detection.

7. Alignment of THz PCA.

   (a) Replace the membrane paper with THz PCA. Ensure the surface of the PCA is merely perpendicular to the incident laser (but not strictly normal to protect the laser device) by checking the refraction from the PCA;

   (b) Increase the pump power and apply bias to the PCA;

   (c) Find the peak of the THz signal. Adjust the distance between the PCA and OM_1 to optimise this signal;

   (d) LS_1 can be inserted for focused laser excitation. After inserting LS_1, the distance between the PCA and OM_1 should not be further adjusted.

Appendix C

Fabrication Procedures for THz PCAs

The fabrication process of THz PCAs in this study in realised by combining metal deposition with thermal vacuum evaporator and photo-lithography. The details fabrication procedures are introduced in details here.

C.1 Thermal Vacuum Evaporator

The schematic and prototype of the vacuum evaporator used in the experiment for metal deposition is shown in Fig. C.1. In the metal deposition process, the substrates are placed at the top of the chamber, while the bulk metal materials are placed at the bottom. Rotary pump and oil diffusion pump are used in sequent to create a fine vacuum (below2×10^{-5} $mbar$). after the build up of the vacuum, metal is heated by a electrical current and evaporated. Metal atoms spread into the vacuum when evaporated, and attached to the surface of the substrate. The thickness of this metal layer and its growing rate can measured by the attached thickness monitor. The growing rate can be controlled by tuning the amplitude of the heating current. This technique

is capable of depositing metal layers with accuracy of thickness within 1 nm.

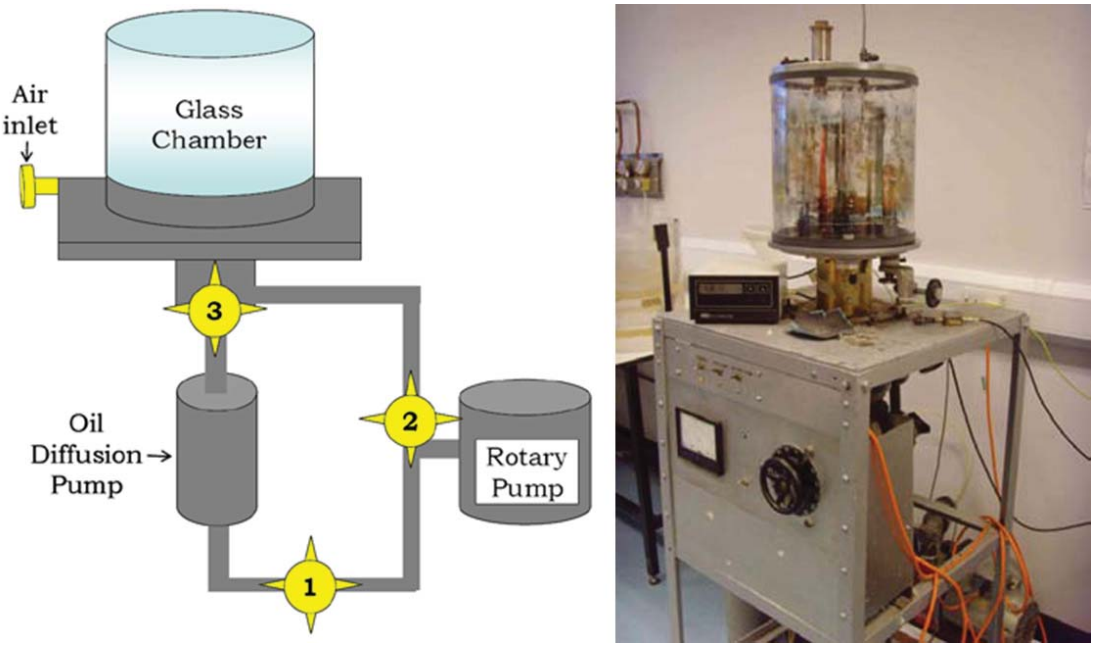

Figure C.1: Schematic of vacuum evaporator (left) and prototype (right)

The detailed procedure is described as following. Valve 1, 2 and 3 are illustrated as in Fig. C.1

1. Turn on water supply
2. Open diffusion pump and leave to warm up for 20min.
3. Open rotary pump and open Valve 1, this will suck air towards rotary.
4. Open air inlet to allow air in and remove glass chamber.
5. Place Al hooks on the tungsten filament and check for a closed circuit by seeing if a current is drawn.
6. Place substrates into holder.
7. Clean glass chamber using acetone including the rim to ensure a better vacuum.
8. Place chamber back and close the air inlet valve and shut Valve 1.

9. Open the rotary pump Valve 2.
10. Wait until the pressure inside the chamber is $\leq 5 \times 10^{-2} mbar$ and open Valve 1.
11. Close Valve 2 and open Valve 3.
12. Pour liquid nitrogen into the diffusion pump.
13. Wait until the pressure inside the chamber drops to $\leq 2 \times 10^{-5} mbar$.
14. Pre-heat the Al at 20 A for approximately 2 min.
15. Draw current at a rate of $\sim 10 \mathring{A}/sec$ (generally around $40 \sim 50A$ of current) until the required Al thickness (shown on thickness monitor) is achieved. Switch off current and allow cool down for $\sim 30 min$.
16. Close Valve 3 and allow air into evaporation system (open air inlet).
17. Once samples have been removed, reassemble evaporation system and turn off diffusion pump and close air inlet.
18. Open Valve 2 and wait for a few minutes to pump down the chamber.
19. Close Valve 2.
20. Wait for $\sim 10 min$ to cool before switching Valve 1 and water supply.

C.2 Photo-lithography

Photo-lithography is a commonly used technique to fabricate micro structures. In practice, the accuracy of photo-lithography is determined the operation protocol, the property of the used photo-resist and the diffraction of the light for exposure. UV light is commonly used owning to its nature of short wavelength. Micro structures with dimension as small as 0.2 μm can be fabricated using UV photo-lithography.

In this work, depending on the requirement of accuracy, two photo-lithography protocols were developed, namely lithography - metal-etching procedure, and lithography - lift-off procedure.

C.2.1 Lithography - Metal-Etching Procedure

In lithography - metal-etching procedure, a metal layer is priorly deposited on the substrate before the photo-lithography process starts. In the fabrication process used in this study, positive photo-resist Shipley MICROPOSIT® S1818 G2 was used for this procedure, in combination with MICROPOSIT®-351 developer. Mask alignment and exposure were realised on mask aligner Suss MicroTec MJB3. The operation protocol for the lithography - metal-etching procedure is described as following:

1. Substrate cleaning.
   (a) Clean both side of the substrate with detergent;
   (b) Sonicate substrates in ultra-clean water for 20 min with ultrasonic bath;
   (c) Sonicate substrates in Acetone for 5 min, and repeat 2 times;
   (d) Sonicate substrates in Chloroform for 5 min, and repeat 2 times;
   (e) Blow-dry substrates using nitrogen.
2. Photo-lithography.
   (a) Place substrates on spin coater, cover the central area with $5\tilde{6}$ drops of photo-resist;
   (b) Spin coat photo-resist on substrate. Spin-coater setting: 800 rpm for 7 s, then 6000 rpm for 30 s. This will give a thin photo-resist layer of approximately 1.7 μm;

(c) Softbake the sample for 1 min on a 115 $^{\circ}C$ hotplate to evaporate water in the photo-resist layer;

(d) Align coated with photo-mask on mask aligner;

(e) UV light exposure. Exposure dose: i-line exposure, 90 mJ/cm^2 (Cl1 on mask aligner MJB3, 9.2 mW/cm^2 for 9.7 s);

(f) Develop to dissolve exposed areas. Developer with distilled water by ratio of 1:3. With manual agitation, the optimum development time is approximately $20 \sim 25s$;

3. Etch metal in the dissolved area.

   For aluminium used in this work, etching can be realised with the developer (contain alkali) following the reaction formula,

$$2\mathrm{Al} + 2\mathrm{NaOH} + 2\mathrm{H_2O} = \mathrm{NaAlO_2} + 3\mathrm{H_2} \uparrow \tag{C.1}$$

   With the diluted developer, the etching rate is approximately 1.4 nm/s at temperature 20 $^{\circ}C$.

4. Cleaning and finishing.

   (a) Sonicate substrates using Acetone for 2 min to remove the remaining photo-resist;

   (b) Sonicate substrates using distilled water for 10 min;

   (c) Blow-dry substrate using nitrogen.

C.2.2 Lithography - Lift-off Procedure

No extra layers are required to start with lithography - lift-off procedure.

In the fabrication process used in this study, negative photo-resist SU-8 2005 and SU-8 developer supplied by MicroChem was used for photo-lithography. MICROPOSIT Remover 1165 is used for the lift-off process, while OmniCoat^{TM} and MICROPOSIT MF-319 were used in combination to assist the lift-off. The operation protocol for the lithography - lift-off Procedure etching procedure is described as following:

1. Substrate cleaning.
   (a) Clean both side of the substrate with detergent;
   (b) Sonicate substrates in ultra-clean water for 20 min with ultrasonic bath;
   (c) Sonicate substrates in Acetone for 5 min, and repeat 2 times;
   (d) Sonicate substrates in Chloroform for 5 min, and repeat 2 times;
   (e) Blow-dry substrates using nitrogen.
2. Deposit OmniCoat^{TM} layer.
   (a) Place substrates on spin coater, cover the central area with $8\tilde{1}0$ drops of photo-resist;
   (b) Spin coat OmniCoat^{TM}. Spin-coater setting: 500 rpm for 5 s, then 3000 rpm for 30 s. This will give a thin OmniCoat^{TM} layer of approximately 17 nm;
   (c) Bake the coated substrate on 200 $^{\circ}C$ hotplate for 1 min, allow the substrate to cool to room temperature;
   (d) Repeat the spin coating and baking process for 2 more times to realise a OmniCoat^{TM} layer with thickness above 50 nm.
3. Photo-lithography.
   (a) Place substrates on spin coater, cover the central area with $5\tilde{6}$ drops of photo-resist;

(b) Spin coat photo-resist on substrate. Spin-coater setting: 500 rpm for 5 s, then 3000 rpm for 30 s. This will give a thin photo-resist layer of approximately 5.0 μm;

(c) Softbake the sample for 2.5 min on a 95 $^{\circ}C$ hotplate to evaporate water in the photo-resist layer;

(d) Align coated with photo-mask on mask aligner;

(e) UV light exposure. Exposure dose: i-line exposure, 100 mJ/cm^2 (Cl1 on mask aligner MJB3, 9.2 mW/cm^2 for 10.8 s);

(f) Post exposure bake. Bake the exposed substrate on a 95 $^{\circ}C$ for 3 min. The image of the photo-mask should start to appear at approximately 1.5 min;

(g) Develop to dissolve unexposed areas with SU-8 developer. The optimum development time is approximately 1.5 min with on agitation in sonicator.

(h) Rinse substrates in Isopropyl Alcohol (IPA);

(i) Develop the OmniCoat^{TM} in the unexposed areas with MICROPOSIT MF-319. Develop time is 30 s;

(j) Rinse substrate with IPA.

(k) Blow-dry substrate using nitrogen.

(l) Hard bake. This step is only required for the fabrication of the buffer layer in the interdigitated PCAs. Place the substrate on a 250 $^{\circ}C$ hotplate for $20 \sim 30$ min to create a solid and stable SU-8 layer.

4. Metal deposition.

   Use vacuum evaporator to deposit metal into the image created by photo-lithography.

5. Lift-off.

(a) Heat the remover to 95 $^{\circ}C$ in water bath environment.

(b) Place the substrates in the heated remover solution. The lift-off process takes approximately $30 \sim 60$ min.

(c) Rinse substrate with IPA for 10 s.

6. Cleaning and finishing.

(a) Sonicate substrates using IPA for 2 min to remove the remaining photo-resist and remover;

(b) Sonicate substrates using distilled water for 10 min;

(c) Blow-dry substrate using nitrogen.

C.2.3 Comparison

The fabrication results of the electrode patterns in interdigitated THz PCA C1 from the two lithography procedures are shown in Fig. C.2.

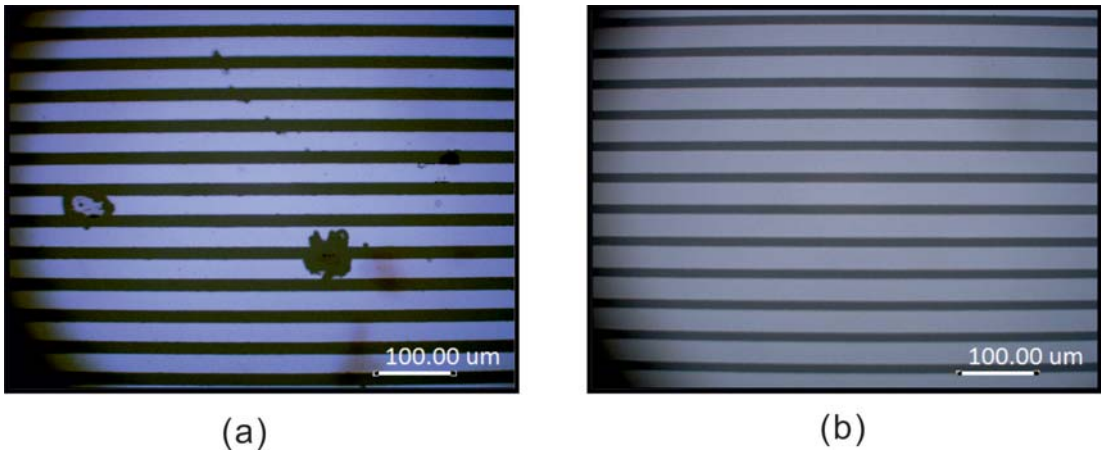

Figure C.2: Fabricated interdigitated electrodes of Pattern C1 from (a) lithography - metal-etching procedure; (b) lithography - lift-off procedure.

In general, with optimised protocols, the accuracies from the two photo-lithography

procedures are comparable. The procedure for lithography - metal-etching is simpler. However, more defects were created with this method. The defects mostly come from the deposition of metal, and the gas generated in the etching process.